

COMPENSATION OF SHAPE CHANGE ARTIFACTS AND SPATIALLY-VARIANT
IMAGE RECONSTRUCTION PROBLEMS IN ELECTRICAL IMPEDANCE
TOMOGRAPHY

By

SUNGHO OH

A DISSERTATION PRESENTED TO THE GRADUATE SCHOOL
OF THE UNIVERSITY OF FLORIDA IN PARTIAL FULFILLMENT
OF THE REQUIREMENTS FOR THE DEGREE OF
DOCTOR OF PHILOSOPHY

UNIVERSITY OF FLORIDA

2009

© 2009 Sungho Oh

To my family in Korea

ACKNOWLEDGMENTS

To begin with, Dr. Rosalind Sadleir deserves all my gratitude for giving me the research-opportunity in the field of Electrical Impedance Tomography. If it were not for our casual meeting in the late summer of year 2004, all this work would not have existed. I feel that I have never expressed my gratitude towards her in a proper way. Now I would like to take this opportunity to say that I am genuinely thankful for the enduring support she provided with me and my research.

My transition from electrical engineering to biomedical engineering would have been impossible without Dr. Hans van Oostrom. His presence has been tremendously helpful throughout my graduate studies. I also want to mention that his current role as a graduate coordinator is highly appreciated.

With Dr. Huabei Jiang in my dissertation committee, I always tried to think outside the box. Fundamental mathematics in image reconstruction problems are essentially the same. I actively searched for relevant literatures in areas other than Electrical Impedance Tomography, hoping that the methods developed in my research could be useful in other areas.

Exchanging ideas with people in other disciplines is one of the rewarding aspects of biomedical research. My external committee member Dr. Charlene Krueger gave me wonderful opportunities to work in her fetal/prenatal research projects. I truly enjoyed working with her in the General Clinical Research Center and Neonatal Intensive Care Units at Shands hospital. From Dr. Paul Carney I learned that there is nothing wrong with holding on to my dreams. Dr. Mathew Saxonhouse provided me with an inspirational opportunity in the Neonatal Intensive Care Unit.

I owe what I am to my family in Seoul, Korea. Life alone and away from home made me realize how much I love my family. I love my parents who put up with their most stubborn and

quirky child. I love my brother and sister who now have become big pillars of our family. I also want to express gratitude to Al-rajhi family in Florida for their friendship and for being there whenever I felt like there was a hole in the chest.

As far as I know, words are the lowest medium in teaching. My best guiding light always has been the lives of my grandparents and ancestors. I hereby swear that I will always do my best to meet your expectations and not to become a disgrace to you as your son, your student, and your friend.

TABLE OF CONTENTS

| | <u>page</u> |
|---|-------------|
| ACKNOWLEDGMENTS | 4 |
| LIST OF TABLES | 9 |
| LIST OF FIGURES | 10 |
| ABSTRACT | 13 |
| CHAPTER | |
| 1 INTRODUCTION | 16 |
| Electrical Impedance Tomography | 16 |
| Clinical Applications | 17 |
| Rationale | 17 |
| Advantages | 18 |
| Continuous Patient Monitoring | 19 |
| Quantitative EIT | 19 |
| Limitations | 20 |
| About This Dissertation | 21 |
| Main Goal | 21 |
| Organization of the Dissertation | 21 |
| 2 FORWARD PROBLEM IN EIT | 23 |
| Electrode Layout | 23 |
| The Full Array | 23 |
| Hemiarray | 23 |
| Electrode Arrays in 3D EIT | 24 |
| Measurement Method | 25 |
| Adjacent Electrode Configuration | 26 |
| Opposite Electrode Configuration | 26 |
| The Forward Problem | 27 |
| 3 IMAGE RECONSTRUCTION IN EIT | 30 |
| Inverse Problem | 30 |
| Time Difference Imaging | 30 |
| The Sensitivity Matrix | 31 |
| Inverse Model | 32 |
| Regularized Inverse | 33 |
| Ill-posed Nature of the Inverse Problem | 33 |
| Singular Value Decomposition | 33 |
| Condition Number | 35 |

| | | |
|---|--|----|
| | Singular Images | 36 |
| | Truncated Singular Value Decomposition | 37 |
| | Weighted Minimum Norm Method | 38 |
| | Tikhonov Regularization | 40 |
| | L-curve | 41 |
| | Quantity Index | 42 |
| 4 | ESTIMATING ELLIPTICAL SHAPE CHANGE OF AN OBJECT BOUNDARY USING JOUKOWSKI TRANSFORMATION IN EIT | 43 |
| | Background..... | 43 |
| | Method..... | 45 |
| | The Joukowski Transformation and Elliptical Boundary Shape Change..... | 46 |
| | Boundary Shape Estimation | 51 |
| | Computer Simulation..... | 53 |
| | Phantom Experiment | 54 |
| | Results..... | 58 |
| | Simulated Data | 58 |
| | Phantom Data | 60 |
| | Discussion and Conclusion..... | 61 |
| 5 | NORMALIZATION OF SPATIALLY-VARIANT IMAGE RECONSTRUCTION PROBLEM IN EIT USING SYSTEM BLURRING PROPERTIES | 64 |
| | Background..... | 64 |
| | Method..... | 65 |
| | Point Spread Function and the Blur Matrix..... | 65 |
| | Normalizing Terms..... | 67 |
| | Pixel-wise Scaling | 67 |
| | Weighted Pseudo-inverse | 68 |
| | WMNM Normalization | 68 |
| | Normalized Sensitivity Matrices | 69 |
| | Reconstruction Matrix after Normalization..... | 69 |
| | Computer Simulation..... | 70 |
| | Phantom Experiment | 71 |
| | Measurement System..... | 72 |
| | Results..... | 72 |
| | Ideal Reconstructions | 72 |
| | Simulated Data | 73 |
| | Phantom Data | 74 |
| | Discussion..... | 79 |
| | Conclusion..... | 82 |

| | | |
|--------------|---|-----|
| 6 | IMAGE RECONSTRUCTION BY WEIGHTED PSEUDO-INVERSION METHOD IN HEMIARRAY EIT | 83 |
| | Introduction..... | 83 |
| | Method..... | 83 |
| | Weighted Pseudo-Inversion..... | 83 |
| | Singular Value Decomposition..... | 84 |
| | Computer Simulation..... | 84 |
| | Results..... | 86 |
| | Noiseless Simulated Measurement..... | 86 |
| | Noisy Simulated Measurement..... | 89 |
| | Localization of Anomaly | 89 |
| | Discussion and Conclusion..... | 89 |
| 7 | FUTURE WORK..... | 92 |
| | Estimation of Shape Change in 3D..... | 92 |
| | Normalization Method in EIT Image Reconstruction | 92 |
| | Test for Anomalies of Different Conductivities..... | 92 |
| | Test for Multiple Anomalies | 92 |
| | Normalization in 3D..... | 93 |
| APPENDIX | | |
| A | MATHEMATICAL FORMULATION..... | 94 |
| | Least Squares Solution | 94 |
| | TSVD Solution (Full Rank)..... | 94 |
| | Weighted Minimum Norm Method..... | 95 |
| | Tikhonov Regularization | 95 |
| | Joukowski Transformation of a Unit Circle | 96 |
| B | MATLAB/COMSOL SCRIPTS..... | 98 |
| | Solve.m | 98 |
| | Solve_batch.m | 102 |
| | Measure.m | 103 |
| | Measure_all_8.m | 103 |
| | Check_sol.m | 104 |
| | Sensitivity.m | 104 |
| | Reconstruct.m | 107 |
| | LIST OF REFERENCES | 108 |
| | BIOGRAPHICAL SKETCH | 116 |

LIST OF TABLES

| <u>Table</u> | <u>page</u> |
|--------------|---|
| 1-1 | Conductivity values (Sm^{-1}) of mammalian tissues18 |
| 2-1 | The complete sequence of measurements using 8-electrode adjacent electrode configuration.26 |
| 2-2 | The complete sequence of measurements using 8-electrode opposite electrode configuration.27 |
| 3-1 | Properties of the sensitivity matrices (S) of 8-electrode full array and hemiarray topologies.36 |
| 4-1 | Estimated c (percentile) from the measurements made on cylindrical and elliptical phantoms I and II.62 |
| 5-1 | Condition numbers of the normalized system matrices.69 |
| 5-2 | Index assignment for various normalization methods.70 |
| 5-3 | <i>RSD</i> of QI (5-11) calculated from the ideal measurement reconstructions (at full rank, $k = 20$) of eight electrode cases.72 |
| 5-4 | Maximum deviation error (ε) of the relative QI, calculated from the simulated measurement reconstructions ($k = 16$) of eight electrode cases.73 |
| 5-5 | Maximum deviation error of the relative QI (ε), calculated from phantom reconstructions of eight electrode full array and hemiarray topologies.74 |
| 6-1 | Condition numbers of sensitivity matrices with and without weighting.90 |

LIST OF FIGURES

| <u>Figure</u> | <u>page</u> |
|--|-------------|
| 1-1 Schematic of a typical EIT system..... | 16 |
| 2-1 Illustration of 8-electrode full array applied on the boundary of a disk object..... | 23 |
| 2-2 Illustration of 8-electrode hemiarray applied on the boundary of a disk object..... | 24 |
| 2-3 Mesh generation for a 2D disk model with 8-electrode full array and a disk anomaly..... | 28 |
| 2-4 Forward solution for the model in Figure 2-3..... | 29 |
| 3-1 An inverse model composed of 344 elements..... | 32 |
| 3-2 Singular value spread of sensitivity matrices for 8-electrode full array and hemiarray..... | 34 |
| 3-3 Singular images of the full array sensitivity matrix (8-electrodes)..... | 36 |
| 3-5 TSVD reconstructions for FEM models containing a single anomaly..... | 38 |
| 3-6 The l -curve example in Tikhonov regularization..... | 41 |
| 4-1 Extent of shape change..... | 44 |
| 4-2 A 2D disk model after three different degrees of elliptical shape change ($c = 0.1, 0.2$ and 0.3) under the Joukowski transformation..... | 46 |
| 4-3 Inverse Joukowski transformation of an elliptical domain with 16 equidistant boundary electrodes..... | 47 |
| 4-4 Measurements made on the disk model..... | 48 |
| 4-5 Reconstruction image from the measurement on a disk object containing an anomaly at the center..... | 49 |
| 4-6 Absolute values of maximum and minimum of reconstruction amplitude ($\Delta\sigma$) for various degrees of shape change c (%)...... | 50 |
| 4-7 QI vs. the degrees of shape change (<i>Joukowski parameter: c (%)</i>)...... | 50 |
| 4-8 Summary of our method to estimate boundary shape..... | 51 |
| 4-9 The boundary elements that were used for the template (filled with color)...... | 52 |
| 4-10 Template vs <i>Joukowski parameter</i> ($c = 0 \sim 50\%$)...... | 52 |

| | | |
|------|---|----|
| 4-11 | Elliptical phantoms simulating two different degrees of shape change ($c = 0.1$ and 0.2)..... | 55 |
| 4-12 | Prototype KHU Mark1 with 16 channels applied to a cylindrical phantom..... | 56 |
| 4-13 | A malleable cylindrical phantom with 16 bar electrodes..... | 57 |
| 4-14 | Reconstructed images for a single anomaly on five different locations..... | 58 |
| 4-15 | Cost function curve for estimating the amount of shape change..... | 59 |
| 4-16 | Estimation errorbar plot for various amounts of shape change (c). Measurements were noisy with additive WGN of 20dB SNR..... | 59 |
| 4-17 | Reference measurements from homogeneous medium for four different amounts of shape change..... | 60 |
| 4-18 | Elliptical boundary shape estimation by the <i>Joukowski parameter</i> c (%)...... | 61 |
| 4-19 | Area of the domains for the elliptical shape change of various degrees (c)...... | 63 |
| 5-1 | Overview of the ePack system..... | 71 |
| 5-2 | Eight electrode full array images ($k = 17$) reconstructed from phantom measurements made for a blood-like anomaly (100mL) in four different locations on the negative β axis ($r_A/r_P = 0, 0.25, 0.5, \text{ and } 0.75$)...... | 75 |
| 5-3 | Eight electrode hemiarray images ($k = 16$) and relative QI curves reconstructed from a blood-like anomaly (100mL) using methods A1, B1, B4 and C5..... | 78 |
| 5-4 | Radial curves of relative QI calculated using TSVD (A1) and normalization method (C5)...... | 80 |
| 6-1 | Singular images of sensitivities matrices (S and SP)..... | 85 |
| 6-2 | Comparison of singular value spectra S , SP and SW in eight-electrode hemiarray case..... | 86 |
| 6-3 | Images of a single anomaly at 15 different locations reconstructed from noiseless measurements using A) TSVD, B) WMNM and C) the WPI in eight-electrode hemiarray case ($k = 20$)..... | 87 |
| 6-4 | Images of a single anomaly at 15 different locations reconstructed from noisy measurements (AWGN of 30dB) using A) TSVD, B) WMNM and C) the WPI in eight-electrode hemiarray case ($k = 20$)..... | 88 |
| 6-5 | Localization of a single anomaly at various positions from simulated noisy measurements (AWGN of 40dB SNR)..... | 90 |

6-6 Localization of a single anomaly at various positions from simulated noisy measurements (AWGN of 30dB SNR).....91

Abstract of Dissertation Presented to the Graduate School
of the University of Florida in Partial Fulfillment of the
Requirements for the Degree of Doctor of Philosophy

COMPENSATION OF SHAPE CHANGE ARTIFACTS AND SPATIALLY-VARIANT
IMAGE RECONSTRUCTION PROBLEMS IN ELECTRICAL IMPEDANCE
TOMOGRAPHY

By

Sungho Oh

May 2009

Chair: Rosalind J. Sadleir
Major: Biomedical Engineering

Electrical Impedance Tomography (EIT) is an imaging modality in which electrical conductivity within the object is estimated from surface voltage measurements. Conductivity images in EIT can provide clinically significant information, since conductivity changes are closely related with physiological changes inside the body. Clinical applications of EIT are non-invasive, cost-effective and simple to apply to patients. Despite the above advantages, performance of EIT systems is affected by the uncertainties pertaining to patient's body *shape change* and *spatial variability* of the image reconstruction problem. In this research, we identify these uncertainties to be the major sources of reconstruction errors.

In EIT image reconstruction, the surface shape of an image object is often assumed to be known. In clinical environments, shape information is not always available. Discrepancies between the assumed and actual shapes can result in errors that may have clinical significance. We suggest an algorithm that estimates domain shapes for the use in 2D EIT. We investigated elliptical boundary distortions of a unit disk object as changes from circular to elliptical geometries, defined using the Joukowski transformation. Boundary shapes of a real domain were then estimated as ellipses after investigating the spatial characteristics of image artifacts caused

by shape changes. Our method was tested with boundary voltage measurements obtained using a full array electrode layout from elliptical simulation and phantom models containing a small disk anomaly at various positions. We found that the proposed method could estimate elliptical shape changes with relatively small error.

The EIT image reconstruction problem is spatially-variant, meaning that the same anomaly placed at different locations within an image plane may produce different reconstruction signatures. Correcting errors due to this spatial variability should improve reconstruction accuracy. We present methods to normalize the spatially-variant image reconstruction problem by equalizing the system Point Spread Function (PSF). In order to equalize PSF, we used blurring properties of the system derived from the sensitivity matrix. We compared three mathematical schemes: Pixel-Wise Scaling (PWS), Weighted Pseudo-Inversion (WPI) and Weighted Minimum Norm Method (WMNM) to normalize reconstructions. The Quantity Index (QI), defined as the integral of pixel values of an EIT conductivity image, was considered in investigating spatial variability. The QI values along with reconstructed images are presented for cases of 2D full array and hemiarray electrode topologies. We found that a less spatially-variant QI could be obtained by applying normalization methods to conventional regularized reconstruction methods such as Truncated Singular Value Decomposition (TSVD) and WMNM. The normalization methods were tested with boundary voltage measurements obtained from simulation disk models containing a smaller disk anomaly, and cylindrical phantom models with anomalies of various volumes placed at various locations within the electrode plane. For anomalies of the same volume, QI error caused by spatial variability was reduced the most among the tested methods when WMNM normalization was applied to WMNM regularized reconstructions for both hemiarray and full array cases.

The use of the blurring properties was further investigated in hemiarray EIT, where the electrodes cover only one half of the object boundary. Boundary measurements are relatively not sensitive to the conductivity anomaly that lies far away from electrodes, and the anomaly may be invisible or undetected in the images reconstructed using conventional methods. We propose a WPI method to enhance sensitivity in the region distant from the electrodes. The method was tested with data obtained from a 2D circular object. A smaller disk anomaly was varied in location within the object. The WPI method detected anomalies with relatively small errors for the hemiarray case.

CHAPTER 1
INTRODUCTION

Electrical Impedance Tomography

Electrical Impedance Tomography (EIT) is a non-invasive imaging modality that displays conductivity distribution within an object. In EIT, a set of electrodes is positioned on an object's surface, input currents are applied, and the resulting surface voltages are measured. The measurements are dependent on the object's internal conductivity distribution. Given the knowledge of input current patterns and the object's shape, cross-sectional conductivity images can be reconstructed from the measurements (Figure 1-1).

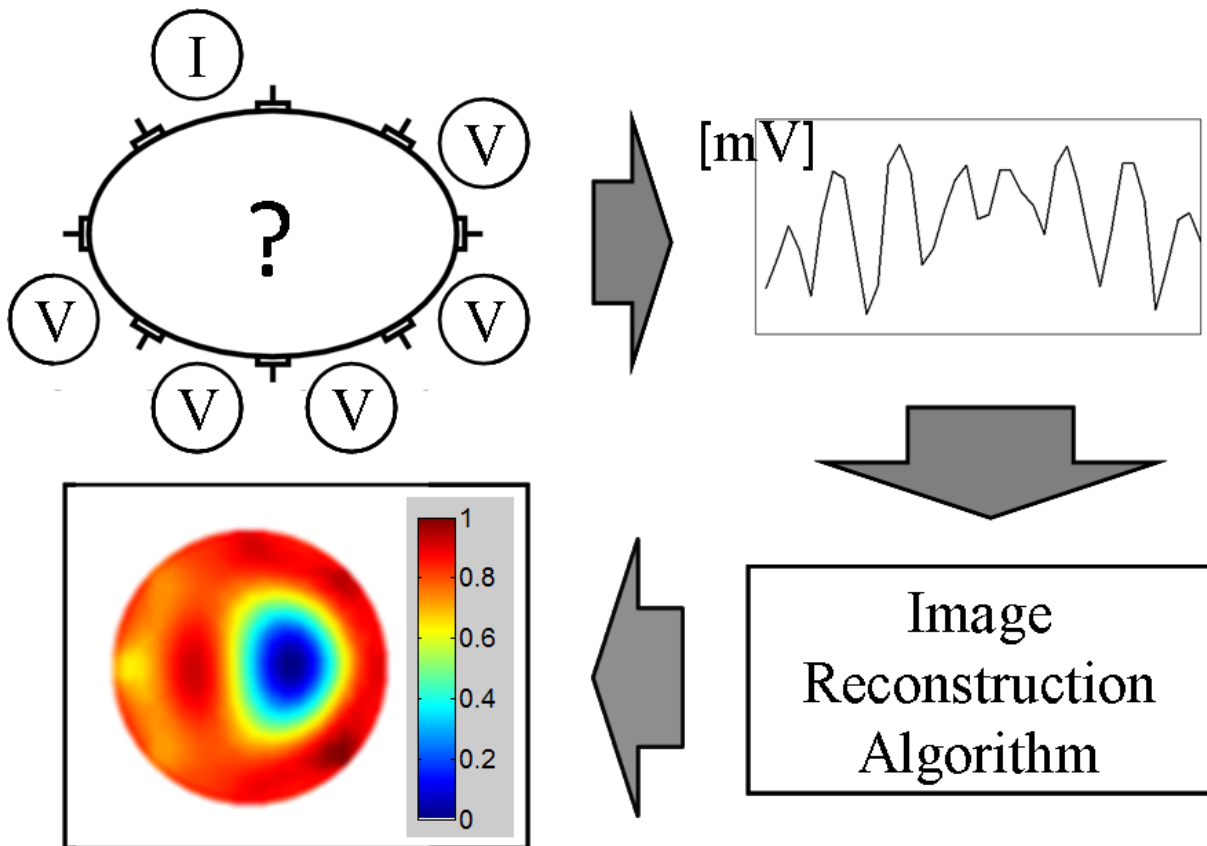


Figure 1-1. Schematic of a typical EIT system.

EIT conductivity images can be useful in many areas, mainly clinical, industrial and geophysical. An emerging area is the molecular medicine where real-time imaging of cell electroporation may become feasible using EIT (Davalos *et al.* 2004). Some examples of industrial and geophysical applications include:

- Imaging of fluid flows in pipes (Dickin and Wang 1996),
- Imaging material distribution within the process vessels (Heikkinen *et al.* 2006),
- Crack detection (Alessandrini and Rondi 1998),
- Detecting air bubbles in pipelines (Ljaz *et al.* 2008),
- Detecting the free surface between the liquid and air (Tossavainen *et al.* 2004),
- Imaging heterogeneities of sandy samples (Borsic A *et al.* 2005),
- Groundwater studies (Nobes 1996),
- Detecting corrosion faults in metallic plates (Vilhunen *et al.* 2002).

In this dissertation, we focused on the clinical aspect of EIT. The main clinical subjects that EIT have demonstrated applicability in are:

- Gastrointestinal tract (gastric emptying and acid secretion),
- Lungs (regional ventilation),
- Brain,
- Pelvis (pelvic blood volume) (Holder 2005, Morucci and Rigaud 1996).

Now let us discuss clinical applications of EIT in more details.

Clinical Applications

Rationale

The human body is made of tissues well contrasted in electrical conductivity (Barber and Brown 1984). Therefore, an imaging modality such as EIT producing distributional maps of conductivity within the body may find useful clinical applications (Dijkstra *et al.* 1993). Table 1-1 shows that the conductivity values of mammalian tissues vary widely with tissue types, and tissues such as blood and cerebrospinal fluid have smaller conductivity values compared to fat and bone tissues.

Table 1-1. Conductivity values (Sm^{-1}) of mammalian tissues (Barber and Brown 1984)

| Tissue | Conductivity |
|--------------------------------|--------------|
| Cerebrospinal fluid | 1.54 |
| Plasma | 1.52 |
| Blood | 0.17 |
| White matter | 0.15 |
| Grey matter | 0.35 |
| Fat | 0.04-0.05 |
| Lung (expiration-inspiration) | 0.04- 0.14 |
| Bone | 0.01 |
| Human arm (longitudinal) | 0.42 |
| Human arm (transverse) | 0.15 |
| Skeletal muscle (longitudinal) | 0.67-0.8 |
| Skeletal muscle (transverse) | 0.04-0.06 |
| Cardiac muscle (longitudinal) | 0.17-0.63 |
| Cardiac muscle (transverse) | 0.02-0.24 |

The conductivity characteristics of pathological tissues differ from those of normal tissues (Walker *et al.* 2000, Sha *et al.* 2002, Keshtkar and Keshtkar 2007, Shini and Rubinsky 2007).

Therefore, EIT conductivity images are anticipated to provide useful screening methods for breast cancer (Cherepenin *et al.* 2001, Soni *et al.* 2004), prostate cancer (Halter *et al.* 2007) or dental caries (Pretty I A 2006).

Advantages

There are several advantages of EIT that makes it especially attractive to clinical application. EIT is completely *non-invasive*, *innocuous* (Ghahary and Webster 1989), and *simple to apply*. It can easily be made portable using either a laptop computer or a PDA (Tang *et al.* 2006). It can be made as a handheld probe and be applied wherever it is needed (Kao *et al.* 2006). Additionally, integration with wireless technology is plausible (McEwan and Holder 2007).

EIT systems can be developed to *promptly acquire data and produce images* (Barber and Seagar 1987) with relatively *low cost*. Their imaging systems can produce real-time images and are cheaper than other imaging modalities such as MRI or CT.

Continuous Patient Monitoring

The advantages mentioned above make EIT system attractive as a continuous patient monitor. The systems can be used to monitor the physiological events that cause detectable conductivity changes continuously, since they can be made to produce real-time conductivity images (Edic *et al.* 1995, Lionheart *et al.* 1997). We categorized the potential imaging areas where EIT has been considered as a continuous patient monitor in the following.

- Brain imaging: detecting intra-ventricular hemorrhage (Murphy *et al.* 1987), brain function monitoring for cerebral ischemia and epilepsy (Boone and Holder 1995) and stroke detection (Romsauerova *et al.* 2006).
- Lung imaging: neonatal lung imaging (Taktak *et al.* 1995), monitoring pulmonary ventilation and perfusion (Campbell *et al.* 1994, Adler *et al.* 1997, Frerichs 2000), pulmonary edema (Adler *et al.* 1995) and emphysema (Eyüboğlu *et al.* 1995).
- Digestive system: monitoring gastric emptying (Mangnall *et al.* 1991, Nour *et al.* 1995).
- Internal hemorrhage: bleeding detection in the pelvis (Meeson *et al.* 1995), bleeding rates monitoring in the peritoneum (Sadleir and Fox 2001, Xu *et al.* 2007),
- Blood flow imaging (Brown *et al.* 1991, Vonk Noordegraaf *et al.* 1997)
- Temperature distribution: thermal monitoring during hyperthermia (Moskowitz *et al.* 1995) and hyperthermia treatment (Conway 1987).

For neonatal patients, applications in monitoring gastric emptying, pulmonary functions and intra-ventricular hemorrhage were considered promising (Murphy *et al.* 1987).

Quantitative EIT

The possibility of quantitative EIT was raised at an early stage of EIT's development. Exemplary applications suggested by Barber (1990) were gastric emptying, cardiac function, pulmonary ventilation and perfusion. Studies that followed demonstrated that estimating volume of conductive anomalies was plausible for some physiological changes. These include the changes of pulmonary liquid volume (Adler and Guardo 1996, Adler *et al.* 1997), bleeding

volume within the pelvic bowl (Thomas *et al.* 1994), bleeding volume inside the ventricles (Blott *et al.* 2000), and bleeding rate inside the peritoneum (Sadleir and Fox 2001).

An earlier work by Pomerantz *et al.* (1970) suggested the use of four-electrode trans-thoracic impedance measurement in monitoring intra-thoracic fluid volume. For patients with significant intra-thoracic fluid accumulation, consistent changes were observed in baseline measurements. In this type of impedance measurement, however, localization of the internal anomalies is not feasible. Additionally, the measurement is highly dependent on electrode errors and on patients' anthropometric parameters that are changeable during measurements (Zlochiver *et al.* 2007), possibly causing false positives. These limitations can be overcome in EIT by solving for the spatial conductivity distribution. The specificity of observations can be verified by inspection of reconstructed spatial distributions, and effects of electrode contact problems and anthropometric variations on EIT reconstructions can be reduced (Soleimani *et al.* 2006, Gómez-Laberge and Adler 2006).

Limitations

The number of electrodes that can be placed on the body surface is limited. As a consequence, the images produced have low spatial resolution. By increasing the number of electrodes, image quality will generally improve. Additionally, using non-stationary electrodes, one can obtain more independent measurements using the same number of electrodes (Murphy and York 2006). However, Tang *et al.* (2002) found that improvements were found near the object boundary rather than in the image center when more electrodes are considered. Therefore, having more measurements may not directly relate to the improvements of measurement sensitivity with respect to the changes in the body center.

The EIT image reconstruction problem is ill-posed, meaning that small measurement noise can cause large image artifacts (Holder 2005). The problem usually has to be regularized in order

to produce meaningful images. Regularized images may still produce inaccurate quantity estimation due to *spatial-variability* of the reconstruction problem. The effect of the spatial variability is that the reconstruction of an anomaly varies with its position. This can lead to significant errors in quantitative EIT (Adler *et al.* 1997, Sadleir and Fox 1998). Correcting these errors will result in more accurate reconstruction, and after the correction reasonable accuracy may be achievable with smaller number of electrodes.

Another important factor limiting the performance of EIT systems is the patients' body movements (i.e. breathing) and uncertainties related with the use of electrodes (i.e. misplacement or positional changes). For convenience, we use the term *shape change* whose general meaning includes all the uncertainties mentioned above (Oh *et al.* 2008). Shape change problems are almost unavoidable in clinical practices, and the image artifacts are hard to remove by conventional regularization methods, producing significant errors (Adler *et al.* 1996).

About This Dissertation

Main Goal

We aim to improve reconstruction accuracy by reducing errors caused from the above identified problems in EIT image reconstruction. Our main goal is *to compensate for the effects of shape change and spatial variability in EIT image reconstruction.*

Organization of the Dissertation

This dissertation is organized as follows. In Chapter 1, we give a brief introduction about EIT and its applications. Limitations of clinical EIT are identified, which lead us to the goal statement of this work. In Chapter 2 and 3, forward and inverse problems in EIT image reconstruction are described. In Chapter 4, we describe methods to compensate for artifacts caused by shape change, and demonstrate a method to estimate domain boundaries as ellipses. The estimated shapes are found to be effective in reducing shape change artifacts. In Chapter 5,

errors due to spatial variability in the image reconstruction problem are identified. We aim to reduce these errors by normalization using the system blurring properties. We finish the chapter by proposing one normalization method that shows the best performance among the ones in comparison. In Chapter 6, a blurring property is found to be useful in enhancing localization of anomalies when applied as the WPI for the hemiarray case. In Chapter 7, we conclude this work by suggesting future works.

CHAPTER 2
FORWARD PROBLEM IN EIT

Electrode Layout

The Full Array

In the full array layout, electrodes are positioned equally spaced around a 2D object boundary. This ensures current projections to be axially symmetric within the assumed object shape. Barber and Seagar (1987) showed that clinically useful images can be reconstructed in difference EIT using this type of 2D array. In Figure 2-1, use of the 8-electrode full array on a 2D disk model is illustrated. The angle between two adjacent electrodes is 45° for this model.

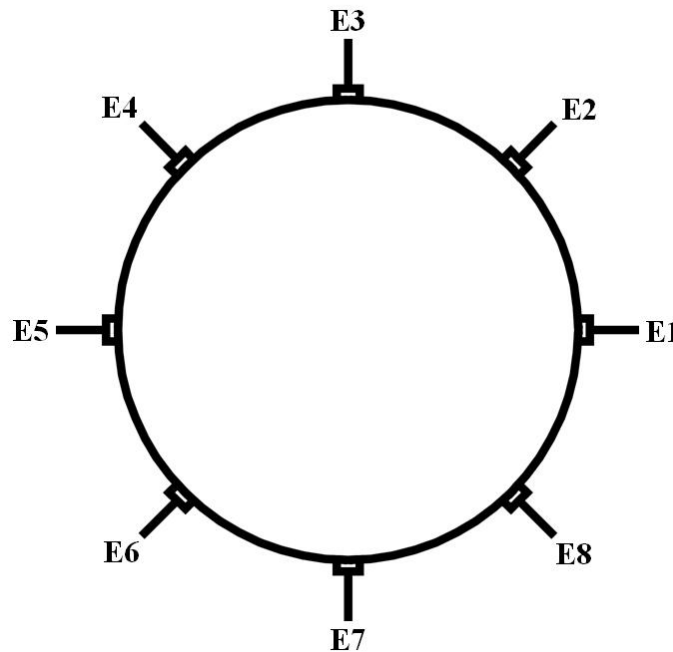


Figure 2-1. Illustration of 8-electrode full array applied on the boundary of a disk object. Electrodes are indexed from E1 to E8.

Hemiarray

The novel hemiarray electrode layout was motivated by EIT apparatus for the detection of intra-peritoneal hemorrhage (Sadleir *et al.* 2008). Patients in blunt trauma accidents, who are suspected to have developed intra-peritoneal hemorrhage, may also have injured their spines. In

such a case, lifting the body in order to place electrodes on the back can further damage the spine. Therefore, the preferred electrode locations will be the anterior surface of the body for patients in supine position, and this is where the hemiarray can be practical. In Figure 2-2, use of the 8-electrode hemiarray is illustrated on a 2D disk model. The angle of each pair of adjacent electrodes is 22.5° , with the exception of the angle (225°) of the bottom pair (E8, E1).

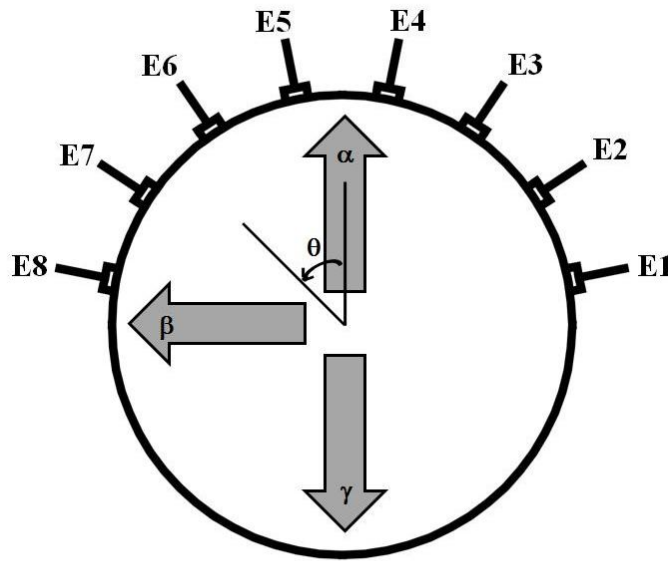


Figure 2-2. Illustration of 8-electrode hemiarray applied on the boundary of a disk object. Electrodes are indexed from E1 to E8. Variable θ was used to represent clock-wise angular displacement away from the north-pole. Axes whose θ values were 0° , 90° , and 180° were denoted as α , β and γ respectively.

Although using the hemiarray electrodes can be very practical in some cases, the current projections formed by using the hemiarray are highly asymmetric within the image plane. Typically, measurement sensitivity is comparatively low in the γ region, which is further away from electrodes.

Electrode Arrays in 3D EIT

3D expansion of the full array can be useful when imaging objects have near cylindrical shapes. Frerichs et al. (1999) used three layers of 16-electrode full arrays placed on the chest to

image ventilation. Dehghani *et al.* (2005) used four layers of 16-electrode full arrays to image human breast.

The linear electrode array suggested by Powell *et al.* (1987) has an advantage in which it can be placed on the desired part of the body surface. Kotre (1996) suggested the use of linear electrode arrays placed orthogonally for subsurface imaging.

When applying electrodes in EIT, the design of electrode arrays can be clinically or practically motivated. Rectangular electrode arrays were considered for breast cancer detection (Mueller *et al.* 1999), in which a handheld EIT probe could be pushed to flatten the breast. For head imaging (as in stroke cases), a modified 10-20 EEG electrode layout is a practical choice (Tidswell *et al.* 2001). In the neonatal skull, fontanel stays open for a relatively long period of time. It has higher electric conductivity than the surrounding skull bone tissues. Based on this feature, an electrode placed on top of the fontanel could be used for current injection consistently. A previous study by Sadleir and Tang (2009) applied this configuration to the detection of neonatal intra-ventricular hemorrhage.

Measurement Method

Once positioned, the electrodes are used to inject currents and measure the resulting voltages. The sequence of obtaining measurements using the electrodes has to be configured in a certain way. In this chapter, we discuss two current injection methods that uses adjacent and opposite electrode pairs.

Based on the superposition principle, measurements made using all available adjacent pairs are generally seen to be sufficient. For example, the measurement made using the (E1, E3) pair will, theoretically, be identical to the sum of the measurements made using the (E1, E2) and (E2, E3) pairs (Figure 2-1). In practice, electrodes used for current injection are not shared for voltage

measurements in order to avoid uncertainties that can arise from the changes of contact impedances in electrodes.

Adjacent Electrode Configuration

In the adjacent electrode configuration, an adjacent pair of electrodes is chosen to drive input current. A frame of input boundary voltage measurements is made using all adjacent pairs excluding the input pair. The next neighboring input pair produces the next frame of measurements and so on. This procedure is repeated for all the possible adjacent input pairs.

Table 2-1 shows the complete sequence of measurements using the adjacent electrode configuration in 8-electrode case. The measurement is conventionally configured so that the first measurement always begins from the lowest number of the electrode indexes.

Table 2-1. The complete sequence of measurements using 8-electrode adjacent electrode configuration.

| Input pair | Output pairs |
|------------|--|
| (E1, E2) | (E3, E4), (E4, E5), (E5, E6), (E6, E7), (E7, E8) |
| (E2, E3) | (E4, E5), (E5, E6), (E6, E7), (E7, E8), (E8, E1) |
| (E3, E4) | (E1, E2), (E5, E6), (E6, E7), (E7, E8), (E8, E1) |
| (E4, E5) | (E1, E2), (E2, E3), (E6, E7), (E7, E8), (E8, E1) |
| (E5, E6) | (E1, E2), (E2, E3), (E3, E4), (E7, E8), (E8, E1) |
| (E6, E7) | (E1, E2), (E2, E3), (E3, E4), (E4, E5), (E8, E1) |
| (E7, E8) | (E1, E2), (E2, E3), (E3, E4), (E4, E5), (E5, E6) |
| (E8, E1) | (E2, E3), (E3, E4), (E4, E5), (E5, E6), (E6, E7) |

This type of measurement method yields a total of $n \times (n-3)$ measurements for n electrodes. Due to reciprocity, only half the measurements are independent (Malmivuo and Plonsey 1995). For example, using 8-electrodes we can obtain 40 measurements in total, but only 20 of them are independent.

Opposite Electrode Configuration

In the opposite electrode configuration, a pair of electrodes that are diametrically opposite is selected for input current injection. Boundary voltage measurements are made using adjacent pairs of all combinations selected from the rest of the electrodes. The opposite electrode

configuration showed improved measurement sensitivity and SNR in domain center (Avis and Barber 1994). However, it produces fewer measurements compared to adjacent electrode configuration. When n electrode are used, it produces $n \times (n-4)$ measurements in total, and only half of them are independent. This indicates that localization accuracy may improve, but image resolution may not. In cerebral imaging, the presence of the skull prevents the current from entering the brain, significantly decreasing measurement sensitivity and SNR. The opposite current injection was suggested by Bayford *et al.* (1996) for cerebral imaging. Where opposite or approximately opposite current injection was used for 3D cerebral imaging, more accurate localization was expected (Tidswell *et al.* 2001, Dong *et al.* 2005, Romsauerova *et al.* 2006).

Table 2-2 shows the complete sequence of measurements using the opposite electrode configuration in 8-electrode array case. Measurements were configured so that the first measurement always began from the lowest number of the electrode indexes.

Table 2-2. The complete sequence of measurements using 8-electrode opposite electrode configuration.

| Input pair | Output pairs |
|------------|--|
| (E1, E5) | (E2, E3), (E3, E4), (E6, E7), (E7, E8) |
| (E2, E6) | (E3, E4), (E4, E5), (E7, E8), (E8, E1) |
| (E3, E7) | (E1, E2), (E4, E5), (E5, E6), (E8, E1) |
| (E4, E8) | (E1, E2), (E2, E3), (E5, E6), (E6, E7) |
| (E5, E1) | (E2, E3), (E3, E4), (E6, E7), (E7, E8) |
| (E6, E2) | (E3, E4), (E4, E5), (E7, E8), (E8, E1) |
| (E7, E3) | (E1, E2), (E4, E5), (E5, E6), (E8, E1) |
| (E8, E4) | (E1, E2), (E2, E3), (E5, E6), (E6, E7) |

The Forward Problem

The forward problem in EIT is to calculate the internal electric potential Φ from the applied current density J for a known conductivity distribution σ within a given object Ω . The object boundary $d\Omega$ is assumed to be smooth. When the prescribed input J is transmitted through

$d\Omega$, the corresponding Φ is generated following the Laplace equation shown in Equation 2-1a with the boundary condition as in Equation 2-1b.

$$\nabla \cdot (\sigma \nabla \Phi) = 0 \text{ in } \Omega \text{ subject to} \quad (2-1a)$$

$$\sigma(x, y, z) (\partial \Phi / \partial n) = -J \text{ on } d\Omega \quad (2-1b)$$

Here, n is a unit outward normal to the surface and σ is a function of positional variables (x, y, z) .

Ideally, forward problems can be solved analytically. However, analytical solutions are not always possible for domains that have complex shape or non-uniform conductivity distribution. In such cases, the Finite Element Method (FEM) can be used to provide numerical approximations of the analytical solution. In FEM, the object domain is divided into small elements. A mesh structure composed of the triangular elements is displayed in Figure 2-3. We designed a 2D disk model containing a smaller disk anomaly with 8-electrode full array (Comsol Multiphysics: Burlington MA). The model was discretized to 1472 second-order triangular finite elements.

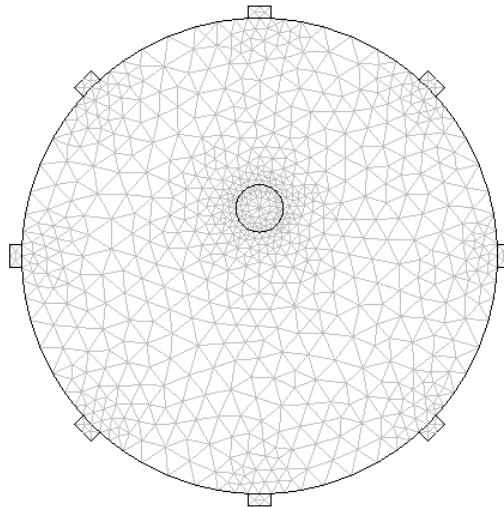


Figure 2-3. Mesh generation for a 2D disk model with 8-electrode full array and a disk anomaly.

Then, the solution is approximated as a polynomial function in each element where pixel values are assumed to be constant. If the elements are sufficiently small, the finite element solution is supposed to approach the exact solution closely. We assigned electrodes the conductivity of copper (5.99×10^7 [Sm^{-1}]). Conductivity values for background and anomaly were 1 [Sm^{-1}] and 2 [Sm^{-1}] respectively. We applied inward current density on the boundary of electrode E1 (1 [Am^{-2}]) and E2 (-1 [Am^{-2}]). The rest of the boundary segments were electrically insulated. The solution (electric potential: Φ) of our forward problem was solved using the direct linear system solver UMFPACK (Unsymmetric MultiFrontal PACKage) and displayed in Figure 2-4.

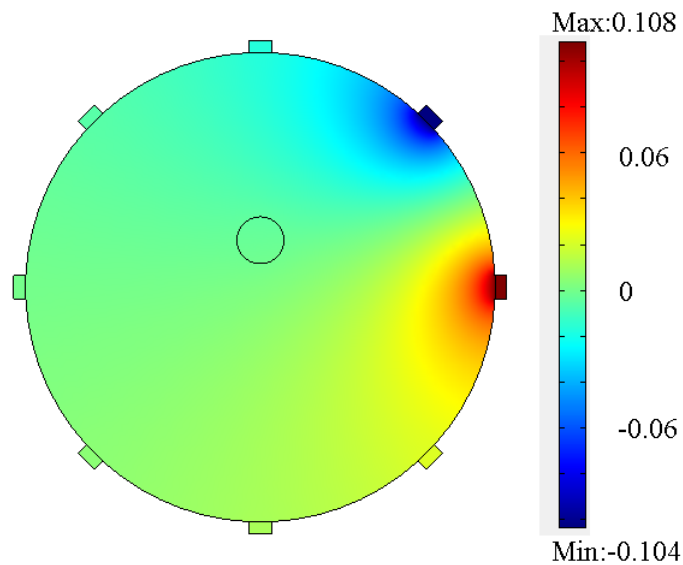


Figure 2-4. Forward solution for the model in Figure 2-3. Electric potential field is generated for the current density applied on electrode E1 (1 Am^{-1}) and E2 (-1 Am^{-1}) in a 2D disk model (1 Sm^{-1}) containing a smaller disk anomaly (2 Sm^{-1}).

CHAPTER 3 IMAGE RECONSTRUCTION IN EIT

Inverse Problem

For a fixed input current pattern and an object shape, a boundary voltage measurement V can be written as a function of conductivity distribution σ as in Equation 3-1.

$$V = f(\sigma) \quad (3-1)$$

The inverse problem in EIT image reconstruction is to estimate for the solution σ , using the nonlinear relation f between σ and V .

Time Difference Imaging

Reconstructing images of small conductivity changes from measurement changes over time is termed time difference imaging. In EIT, a sequence of difference images can be obtained in real-time, which is desirable for continuous monitoring or functional imaging applications.

For a small conductivity change $\Delta\sigma$ away from the reference conductivity distribution σ_0 , the measurement $f(\sigma)$ can be expressed as a Taylor series as in Equation 3-2.

$$V = f(\sigma_0) + f'(\sigma_0) \cdot \Delta\sigma + \frac{f''(\sigma_0) \cdot \Delta\sigma^2}{2!} + \dots + \frac{f^n(\sigma_0) \cdot \Delta\sigma^n}{n!} + \dots \quad (3-2)$$

By ignoring higher order terms, we obtain a linear approximation as in Equation 3-3.

$$V \cong f(\sigma_0) + f'(\sigma_0) \cdot \Delta\sigma, \quad (3-3)$$

where $f(\sigma_0)$ is the reference measurement V_0 , and $f'(\sigma_0)$ the Jacobian. If we move the reference measurement V_0 to the left hand side of the equation, we get Equation 3-4.

$$V - V_0 = \Delta V \cong f'(\sigma_0) \cdot \Delta\sigma, \quad (3-4)$$

where ΔV is the measurement change away from $f(\sigma_0)$. One can express $f'(\sigma_0)$ in matrix form, which gives us a system of linear equations as in Equation 3-5.

$$\Delta V \cong \mathbf{S}\Delta\sigma, \quad (3-5)$$

where \mathbf{S} is the Jacobian matrix, also termed the sensitivity matrix. Now, the nonlinear inverse problem of Equation 3-2 is linearized to Equation 3-5. In Equation 3-6, all the terms of the components in Equation 3-5 are laid out.

$$\begin{bmatrix} \Delta V_1 \\ \Delta V_2 \\ \vdots \\ \Delta V_i \\ \vdots \\ \Delta V_M \end{bmatrix} \cong \begin{bmatrix} \mathbf{S}_{1,1} & \mathbf{S}_{1,2} & \cdots & \mathbf{S}_{1,j} & \cdots & \mathbf{S}_{1,N} \\ \mathbf{S}_{2,1} & \mathbf{S}_{2,2} & & & & \\ \vdots & & \ddots & & & \vdots \\ \mathbf{S}_{i,1} & & & \mathbf{S}_{i,j} & \ddots & \\ \vdots & & & & \ddots & \\ \mathbf{S}_{M,1} & \cdots & & & & \mathbf{S}_{M,N} \end{bmatrix} \cdot \begin{bmatrix} \Delta\sigma_1 \\ \Delta\sigma_2 \\ \vdots \\ \Delta\sigma_j \\ \vdots \\ \Delta\sigma_N \end{bmatrix}, \quad (3-6)$$

where M is the total number of measurements, and N is the total number of elements (pixels) within the inverse model.

In Equation 3-5, $\Delta\sigma$ will be solved from measurement ΔV for an assumed \mathbf{S} . While inversion of the linearized equation as in Equation 3-5 can be iterated to obtain more accurate solution, a single step inversion was shown to produce reasonable reconstructions (Cheney *et al.* 1990, Avis and Barber 1992). The method used in this dissertation is also based on a single step inversion method, which will be explained later in this chapter.

The Sensitivity Matrix

For every unit element-wise anomaly, the forward problem can be solved to produce a set of measurements. \mathbf{S} can be built by using these sets of measurements as the columns of \mathbf{S} . This approach necessitates solving as many forward problems as the total number of elements.

Using sensitivity theorem or lead field theorem by Geselowitz (1971), Murai and Kagawa (1985) could calculate \mathbf{S} with much less computational burden. Their method requires only one forward problem solved. Each entry \mathbf{S}_{ij} can be calculated as in Equation 3-7.

$$\mathbf{S}_{ij} = -\int_j \frac{\nabla\Phi(\sigma_0)}{I_\phi} \cdot \frac{\nabla\Psi(\sigma_0)}{I_\psi} dv_j \quad (3-7)$$

The i and j are measurement and element indexes respectively. Sensitivity \mathbf{S}_{ij} is a negative integral of the inner product of lead fields due to measurement i over a finite volume of element j (v_j). The input and output lead fields are $\nabla\Phi(\sigma_0)/I_\phi$ and $\nabla\Psi(\sigma_0)/I_\psi$ respectively, for the reference conductivity distribution σ_0 .

The rows and columns of the matrix \mathbf{S} are arranged according to the measurement index i and the element index j . Measurement index was derived from the complete measurement sequence as the one shown in Table 2-1. The j -th column of \mathbf{S} is so-called the *ideal measurements* for a unit conductivity anomaly appearing in the element j .

Inverse Model

We designed an inverse model which was used throughout this work (Figure 3-1). Our model is a simple structure composed of 344 elements. All elements are square, and their areas are the same except the ones lying on the object boundary. We calculated \mathbf{S} for the inverse model having assumed uniform conductivity distribution, since accurate knowledge of internal conductivity is not easily available (Meeson *et al.* 1995).

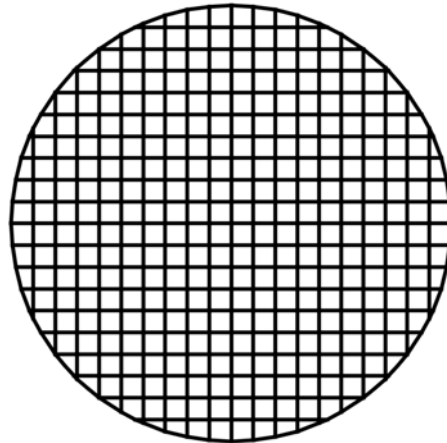


Figure 3-1. An inverse model composed of 344 elements. All elements are square and have the same area excluding the ones on the object boundary.

Regularized Inverse

Ill-posed Nature of the Inverse Problem

In EIT, the total number of measurements is typically smaller than the total number of elements. The number of measurements is limited by the number of electrodes applied. Thus, Equation 3-5 is typically an underdetermined problem, and \mathbf{S} is not square. For a non-square matrix, the direct inverse does not exist in general, in which case the least squares solution can be obtained. In the least squares method, solution is estimated so as to give the best fit that minimizes the sum of squared errors of Equation 3-5 as in Equation 3-8.

$$\min_{\Delta\sigma} \|\Delta V - \mathbf{S} \cdot \Delta\sigma\|_2^2 \quad (3-8)$$

This gives us the least squares solution (3-9) (Appendix A).

$$\Delta\hat{\sigma} = \mathbf{S}^T (\mathbf{S} \cdot \mathbf{S}^T)^{-1} \Delta V \quad (3-9)$$

The inverse problem in EIT image reconstruction is a severely ill-posed problem (Vauhkonen *et al.* 1998). As a result, small amount of noise in the measurement can cause large image artifacts. Simple least squares solutions as in Equation 3-9 will fail to produce meaningful images in EIT image reconstruction. In order to obtain reasonable images, the problem in Equation 3-5 has to be further regularized.

Singular Value Decomposition

Singular Value Decomposition (SVD) is a factorization of a rectangular matrix that has many applications (Golub and Reinsch 1970). Here, we apply SVD to compute the pseudo-inverse of matrix \mathbf{S} . Using SVD any matrix can be represented as a product of a unitary matrix, a diagonal matrix and another unitary matrix as in Equation 3-10.

$$\mathbf{S} = \mathbf{U}\mathbf{D}\mathbf{V}^T, \quad (3-10)$$

where \mathbf{D} is a diagonal matrix whose entries are termed the singular values. The rank of \mathbf{D} is identical to the rank of \mathbf{S} . The singular values are non-negative numbers, arranged in a descending order.

We calculated the matrices \mathbf{S} for the adjacent electrode configuration in the 8-electrode full array and hemiarray cases. In Figure 3-2, the singular values of both matrices are displayed as a log scale plot. Both curves decay gradually to zero indicating that our inverse problem is ill-posed.

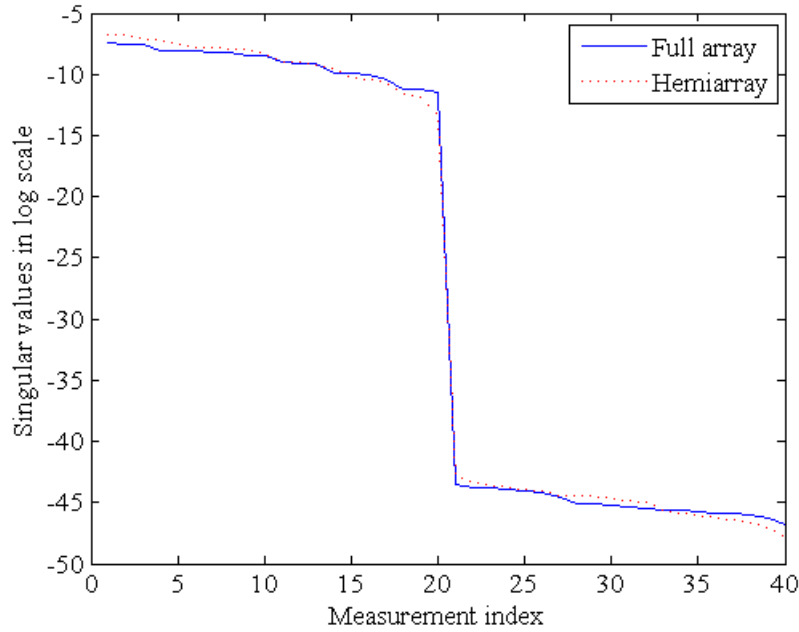


Figure 3-2. Singular value spread of sensitivity matrices for 8-electrode full array and hemiarray.

In Equation 3-10 \mathbf{U} and \mathbf{V} are unitary matrices whose inverses are identical to their transpose. The columns of \mathbf{U} and \mathbf{V} are termed the left and right singular vectors of \mathbf{S} . Written in column form, \mathbf{U} and \mathbf{V} can be expressed as in Equation 3-11.

$$\mathbf{U} = [u_1 \quad u_2 \quad \cdots \quad u_M] \quad (3-11a)$$

$$\mathbf{V} = [v_1 \quad v_2 \quad \cdots \quad v_N] \quad (3-11a)$$

Here, $u_i (M \times 1)$ and $v_i (M \times 1)$ are i -th column of \mathbf{U} and \mathbf{V} respectively. This column form lets us rewrite Equation 3-10 as in Equation 3-12.

$$\mathbf{S} = \begin{bmatrix} u_1 & u_2 & \cdots & u_M \end{bmatrix} \mathbf{D} \begin{bmatrix} v_1^T \\ v_2^T \\ \vdots \\ v_N^T \end{bmatrix} \quad (3-12)$$

Consequently, \mathbf{S} is sum of the rank one matrices ($u_i v_i^T$) weighted by diagonal entries of \mathbf{D} (d_i) as in Equation 3-13.

$$\mathbf{S} = \sum_{i=1}^N d_i u_i v_i^T \quad (3-13)$$

Condition Number

The system matrix of an ill-posed inverse problem is badly conditioned. The condition of a matrix can be represented by the condition number. The condition number of a matrix is defined to be the ratio between its maximum and minimum singular values as in Equation 3-14.

$$\kappa(\mathbf{S}) = \frac{d_{\max}}{d_{\min}} \quad (3-14)$$

where d_{\max} and d_{\min} are the maximum and minimum singular values of \mathbf{S} respectively. Here, the condition number $\kappa(\mathbf{S})$ provides a way to measure the sensitivity of \mathbf{S} to measurement noise. If $\kappa(\mathbf{S})$ is close to 1, the matrix columns are very independent. When $\kappa(\mathbf{S})$ is large, the columns are nearly dependent, making the inverse problem ill-posed.

The condition numbers in Table 2-1 are extremely large, indicating that our inverse problem is severely ill-posed. The hemiarray matrix condition number is larger than the full array, indicating that its inverse problem is more ill-posed. The ranks of both matrices are 20, half the number of total measurements, owing to the reciprocity principle (Malmivuo and Plonsey 1995).

Table 3-1. Properties of the sensitivity matrices (\mathbf{S}) of 8-electrode full array and hemiarray topologies.

| | Full array | Hemiarray |
|------------------|-----------------------|-----------------------|
| Dimensions | 40×344 | 40×344 |
| Rank | 20 | 20 |
| Condition Number | 2.21×10^{17} | 2.02×10^{18} |

Singular Images

Columns of the right singular vector \mathbf{V} are termed the singular images, and they form the basis of the reconstruction images (Zadehkoochak *et al.* 1991). These singular images can provide useful insights about how regularization determines spatial resolution in reconstruction images.

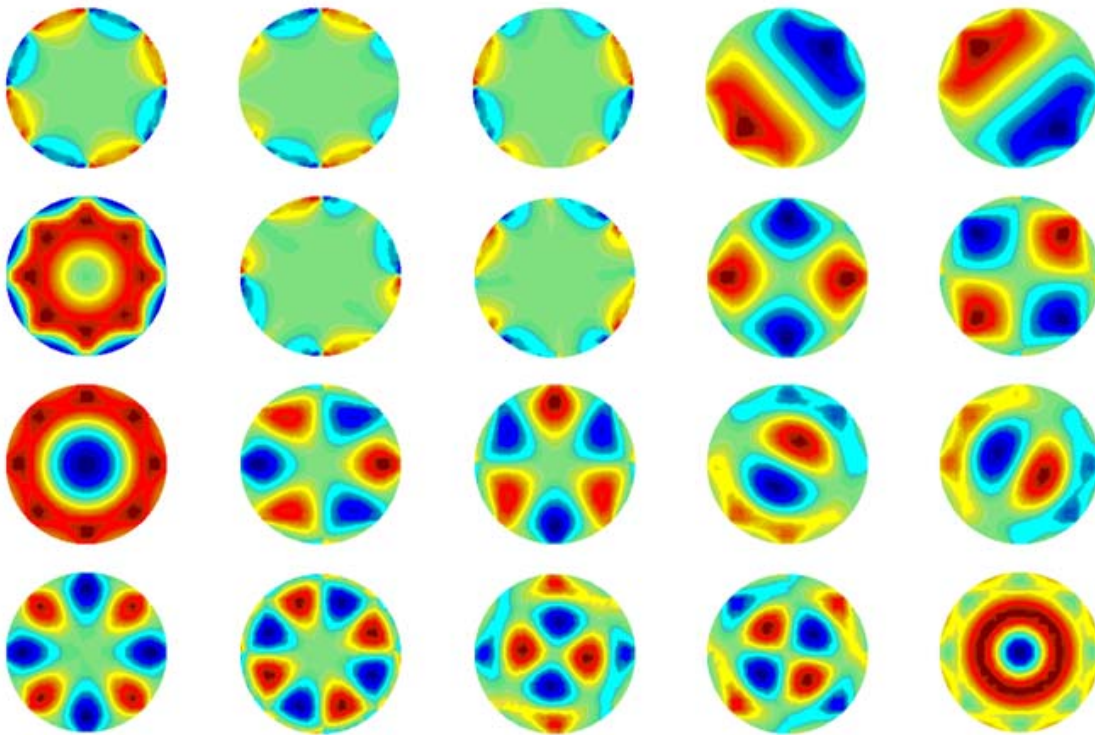


Figure 3-3. Singular images of the full array sensitivity matrix (8-electrodes). The mode number increases from left to right and top to bottom.

In Figure 3-3, singular images of the sensitivity matrix in 8-electrode full array case are displayed. Two main observations may be made from the figure. The boundary region, which is

near the electrodes, will be described ahead of the central region, which is far away from the electrodes. Similarly, lower spatial frequency components in the image will be depicted before higher spatial frequency components.

Singular images in the hemiarray case is seen to be similarly characterized (Figure 3-4). In the hemiarray case, the γ region is furthest away from the electrodes. It is seen that the singular images are unable to describe details of the γ region, indicating potential difficulties in reconstructing anomalies.

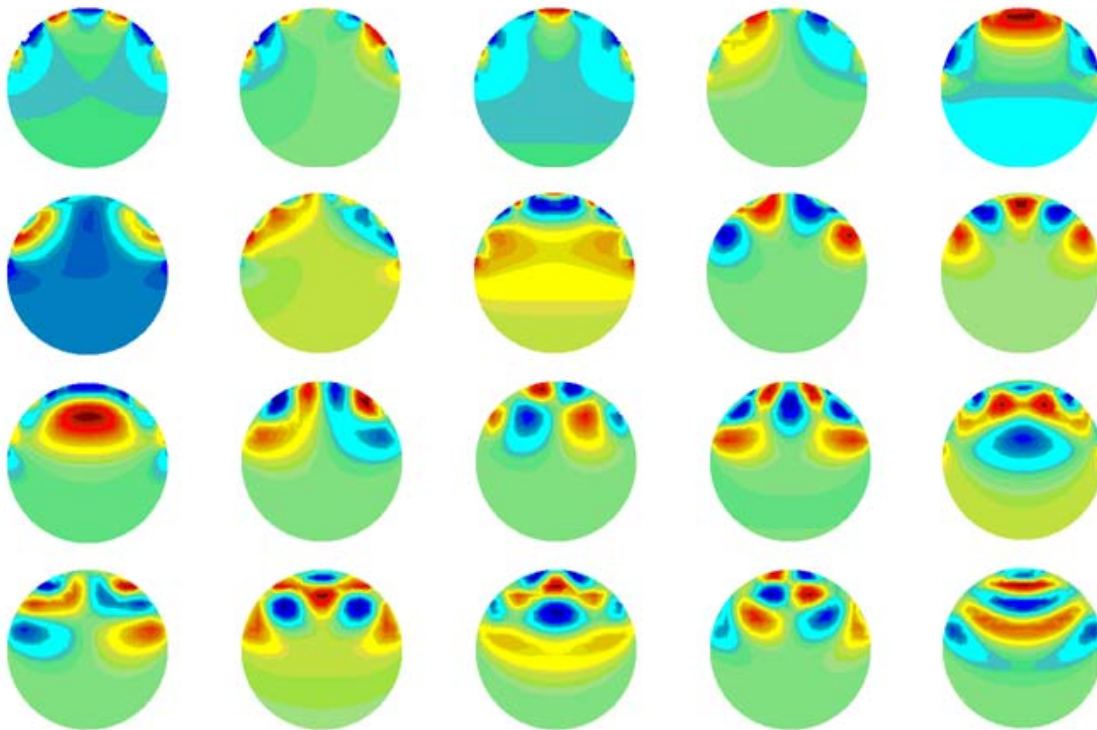


Figure 3-4. Singular images of the hemiarray sensitivity matrix (8-electrodes). The mode number increases from left to right and top to bottom.

Truncated Singular Value Decomposition

In TSVD, we attempt to get a meaningful approximate of the inverse solution by replacing \mathbf{S} by a well-conditioned matrix derived from \mathbf{S} . Based on the SVD of \mathbf{S} in Equation 3-10, the pseudo-inverse of \mathbf{S} (\mathbf{S}^+) can be calculated as in Equation 3-15.

$$\mathbf{S}^+ = \mathbf{V}\mathbf{D}^+\mathbf{U}^T, \quad (3-15)$$

where \mathbf{D}^+ is a truncated inverse of \mathbf{D} . Therefore, an estimated conductivity solution can be estimated using the pseudo-inverse \mathbf{S}^+ as the reconstruction matrix.

$$\Delta\hat{\sigma} = \mathbf{S}^+ \Delta V \quad (3-16)$$

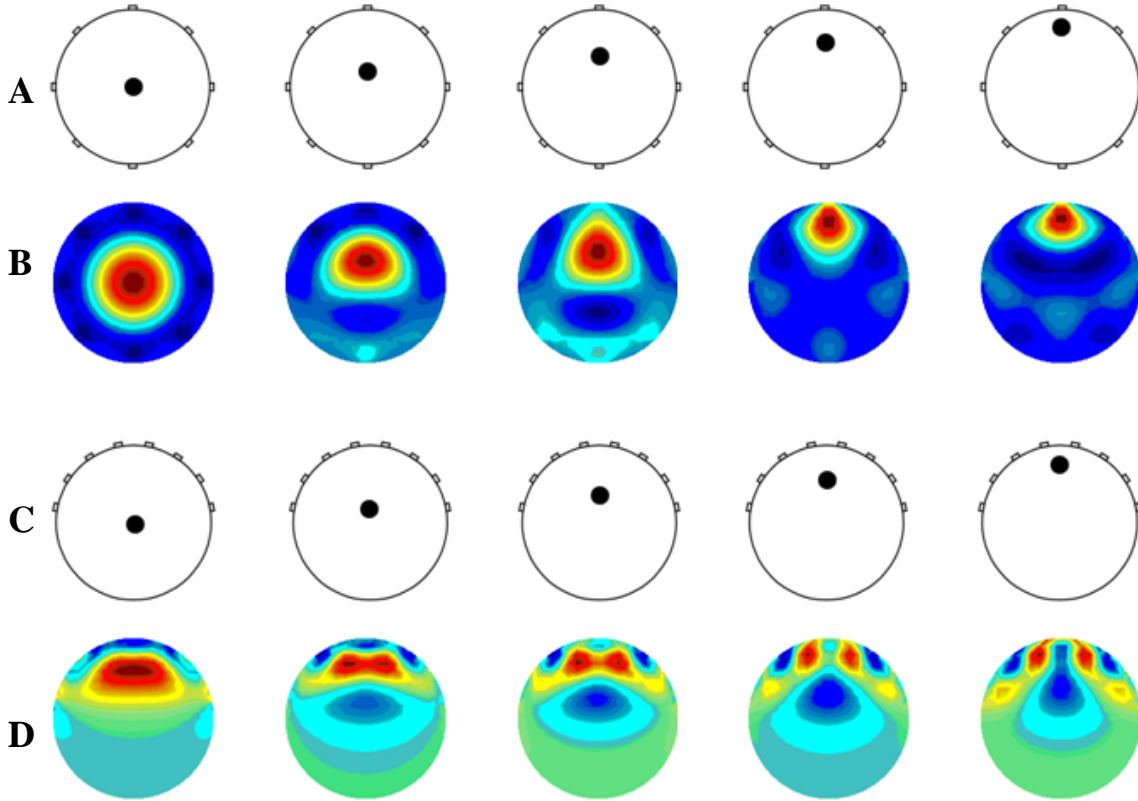


Figure 3-5. TSVD reconstructions for FEM models containing a single anomaly. A) FEM models containing a single anomaly in 5 different locations (8-electrode full array). B) Corresponding images generated from TSVD reconstruction ($k = 16$). C) FEM models containing a single anomaly in 5 different locations (8-electrode hemiarray). D) Corresponding images generated from TSVD reconstruction ($k = 16$).

The higher order singular values of \mathbf{S} correspond to high spatial frequency components in the singular image. As a result of inversion, the higher order values that are small will be reciprocated and show as artifacts in reconstruction image. By way of truncation of the small values, image artifacts can be successfully suppressed. Truncated SVD (TSVD) is such a

procedure that was proposed for discrete ill-posed problems to obtain smooth solutions (Hansen 1987). The estimated solution by TSVD can be expressed as the weighted sum of rank-one matrices as in Equation 3-17.

$$\Delta \hat{\sigma} = \sum_{i=1}^k \frac{u_i^T \Delta V}{d_i} v_i, \quad (3-17)$$

where k is the truncation number. The k can be chosen based on the amount of noise in measurement ΔV (Hansen 1987). When k equals the rank of \mathbf{S} , TSVD solution is the same as the least squares solution, since \mathbf{S}^+ is equal to $\mathbf{S}^T(\mathbf{S}\mathbf{S}^T)^{-1}$ (Appendix A).

Once the reconstruction vector is calculated, images are made by assigning estimated values to their corresponding elements (pixels) in the image plane. In Figure 3-5, images were produced from TSVD solutions and displayed after linear smoothing.

Weighted Minimum Norm Method

Sensitivity values are typically low in the regions that are further from the boundary electrodes. The FOCal Underdetermined System Solver (FOCUSS) algorithm employs the strategy that power normalization of the ideal measurement should improve spatial resolution of images. It was originally proposed for solving inverse problems in Electroencephalogram (EEG) and Magnetoencephalogram (MEG) by Gorodnitsky and Rao (1997). The algorithm produces a least squares solution based on minimization of a re-weighted norm of the solution (Gorodnitsky and Rao 1997). This method and its modifications were successfully adapted to EIT image reconstruction problems of various electrode topologies: full array (Clay and Ferree 2002, Dong *et al.* 2004), hemiarray (Sadleir *et al.* 2008), and modified 10-20 system of EEG electrode layout (Dong *et al.* 2005).

Clay and Ferree (2002) suggested a single step inversion of the FOCUSS algorithm in the context of EIT image reconstruction. This was termed the Weighted Minimum Norm Method

(WMNM) (Sadleir *et al.* 2008). Using WMNM, columns of \mathbf{S} are equalized in terms of its power before pseudo-inversion. The weighting terms (w_j) are defined as in Equation 3-18.

$$w_j = \left(\sum_{i=1}^M S_{ij}^2 \right)^{-1/2} \quad (3-18)$$

The changes made due to this equalization can be recovered by rescaling the pixels. Thus, using a diagonal weighting matrix \mathbf{W} comprised of these terms, the final form of WMNM regularized solution can be obtained as in Equation 3-19 (Appendix A).

$$\Delta\sigma = \mathbf{W}(\mathbf{S}\mathbf{W})^+ \Delta V \quad (3-19)$$

Tikhonov Regularization

When a meaningful solution cannot be computed by TSVD, imposing additional constraints on the problem may resolve this problem. In the general version of Tikhonov regularization, one obtains the solution by minimizing the quantity in Equation 3-20.

$$\arg \min \left\{ \|\Delta V - \mathbf{S} \cdot \Delta\sigma\|_2^2 + \lambda \cdot \|\mathbf{R} \cdot (\Delta\sigma - \sigma_0)\|_2^2 \right\}, \quad (3-20)$$

where \mathbf{R} is regularization matrix and λ is regularization parameter. The Newton's One-Step Error Reconstructor (NOSER) algorithm is a well known example of this type of single step Tikhonov regularization solution with \mathbf{R} being $\text{diag}(\mathbf{S}^T \mathbf{S})$ (Cheney *et al.* 1990). In Equation 3-21, we present zero-order Tikhonov regularization for an identity matrix \mathbf{R} and a zero vector σ_0 .

$$\arg \min \left\{ \|\Delta V - \mathbf{S} \cdot \Delta\sigma\|_2^2 + \lambda \cdot \|\Delta\sigma\|_2^2 \right\}, \quad (3-21)$$

Larger λ means larger amount of regularization constraining the solution $\Delta\sigma$ to have smaller norm. Algebraic form of the solution from Equation 3-21 is shown in Equation 3-22 (Appendix A).

$$\Delta\sigma = (\mathbf{S}^T \mathbf{S} + \lambda \cdot \mathbf{I})^{-1} \mathbf{S}^T \cdot \Delta V \quad (3-22)$$

L-curve

The choice of regularization parameter λ (or the truncation number k for TSVD) will determine the level of regularization, and is affected by the noise quantity in ΔV , which is generally unknown. The use of the l -curve was suggested in selecting adequate regularization parameters (Hansen 1992). In the l -curve, the solution norm is plotted versus the residual norm in log-log scale. The resulting curve is usually concave (L-shaped), hence its name. The l -curve displays a trade-off in regularization, where maximum curvature point is often seen as an optimal choice of a regularization parameter (Hansen and O'Leary 1993).

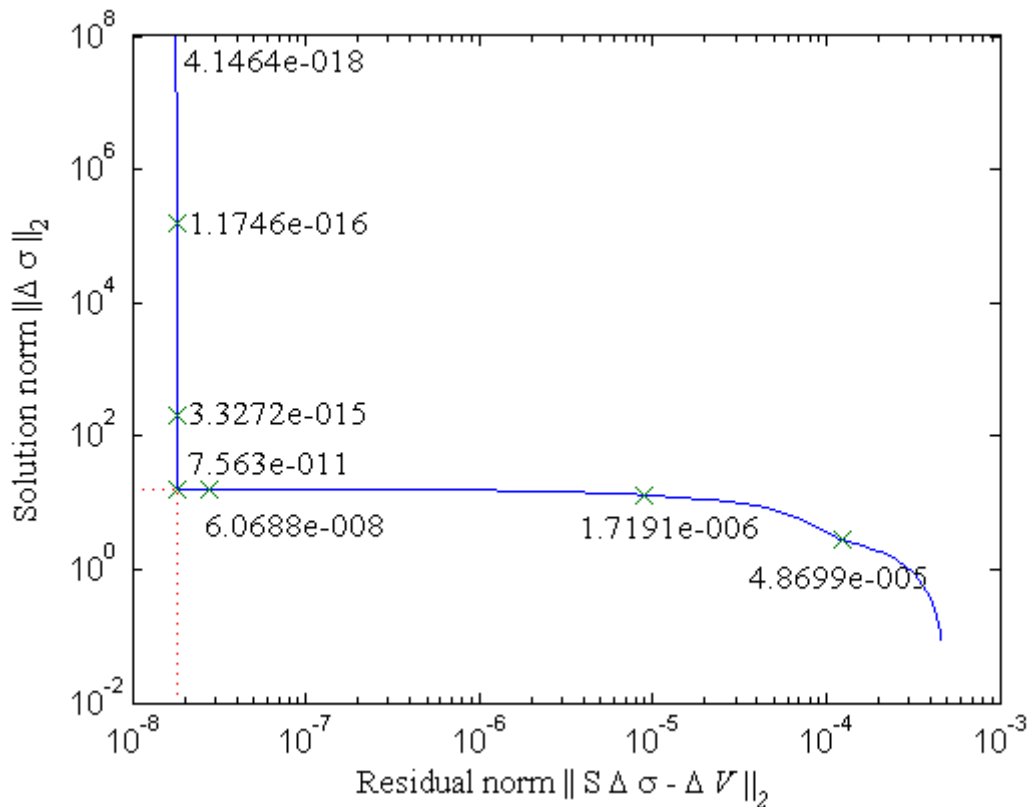


Figure 3-6. The l -curve example in Tikhonov regularization. The corner was located at $\lambda = 7.563 \times 10^{-11}$.

In Figure 3-6, *l*-curve for Tikhonov regularization was generated from the boundary measurement made from the 8-electrode FEM model with a central anomaly. Its corner was located at $\lambda = 5.2746 \times 10^{-11}$ using the regularization toolbox by Hansen (1994).

Quantity Index

Recently, estimation of absolute conductivity values has been studied using parametrical forward models, where the absolute conductivity values producing the best fit to conductivity measurements are suggested (Brown *et al.* 2002, Zhang and Patterson 2005). However, design of a parametrical model can be difficult for certain body parts due to temporal shape changes during measurement or large shape variations across patients.

Here, we propose an integral of EIT images as a useful measure related with anomaly volume. The quantity defined in Equation 3-23 is termed the Quantity Index (QI), which can be thought as the average of conductivity change multiplied by the number of elements N .

$$QI = \sum_{j=1}^N A_j \cdot \Delta\sigma_j \quad (3-23)$$

For an element (or pixel) j , conductivity change and element area are denoted as $\Delta\sigma_j$ and A_j respectively.

For later investigation, we define the relative QI (δQI) for the reference QI as in Equation 3-24.

$$\delta QI = QI / QI_0 \quad (3-24)$$

Unless otherwise noted, QI for an anomaly located at the domain center was used for QI_0 .

CHAPTER 4
ESTIMATING ELLIPTICAL SHAPE CHANGE OF AN OBJECT BOUNDARY USING
JOUKOWSKI TRANSFORMATION IN EIT

Background

Measurements in EIT are sensitive to uncertainties related with electrodes and variations of body shapes (i.e. respiratory movements and postural changes). Consequently, artifacts due to the corresponding errors in the measurement often dominate reconstruction images, which lead to significant errors in estimating anomaly volumes. These errors have to be corrected for successful EIT imaging and quantitation (Adler *et al.* 1996, Sadleir and Fox 2001, Zhang and Patterson 2005).

Previously, it has been shown that even a slight *shape mismatch* in the boundary shape models can produce significant image artifacts (Breckon and Pidcock 1988, Kolehmainen *et al.* 2005). Additionally, the body is subject to *temporal shape changes* such as thoracic expansion (Adler *et al.* 1996). Shape variations of object boundaries are closely correlated with variations in electrode locations, therefore, problems such as *electrode misplacement* (Barber and Brown 1988), and *electrode movement* (Soleimani *et al.* 2006) are analogous to the shape-related problems. Uncertainties related with body shape and electrodes cause similarly characterized image artifacts (i.e. spurious peaks near the object boundary) (Soleimani *et al.* 2006, Boyle *et al.* 2008). Here, we use the term *shape change* to describe these uncertainties in a collective sense (Figure 4-1).

In difference EIT, recovery of reconstruction quality may be possible using the knowledge about the correct boundary shape. Barber and Brown (1988) showed that image artifacts due to electrode errors were effectively removed using the reference measurements made on the homogeneous model of the correct boundary shape.

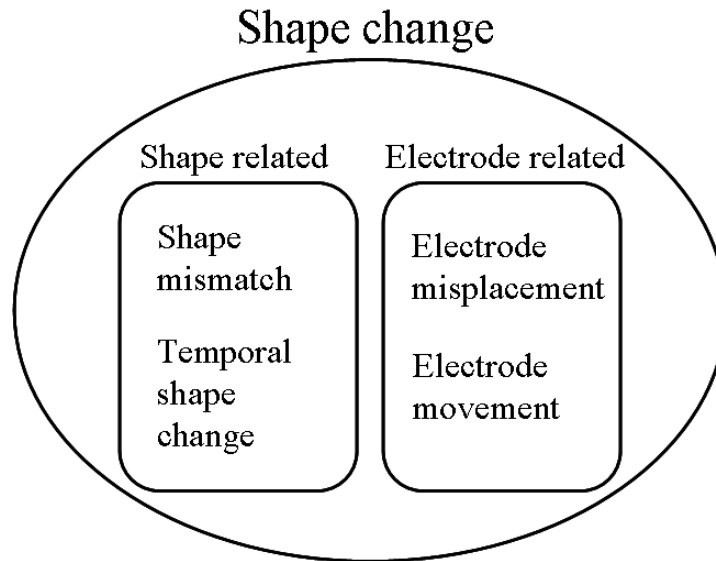


Figure 4-1. Extent of shape change.

Shape estimation using CT, MRI or Ultrasound (Molebny *et al.* 1996) is not always available. On the other hand, we can readily approximate object shapes all the time from EIT measurements, since they depend principally on shape (Barber and Brown 1988). Breckon and Pidcock (1988) estimated domain boundary by describing its shape approximately in terms of Fourier series. Kolehmainen *et al.* (2005) introduced a numerical method that “finds a deformed image of the original isotropic conductivity based on the theory of Teichmüller spaces”. Information about electrode locations can roughly describe boundary shapes, and can be used to enhance reconstruction images. Kiber *et al.* (1990) parameterized measurements in terms of separation of electrodes, and estimated electrode positions iteratively to approximate boundary shapes. Soleimani *et al.* (2006) proposed the use of an augmented Jacobian matrix. Using the matrix, both the spatial information of electrode movement and the conductivity change was simultaneously reconstructed. Measurement sensitivity to unit perturbation of each electrode position composed the augmented columns of the matrix. Heikkinen *et al.* (2002) conducted a

similar approach, which simultaneously reconstructed the conductivity distribution and the contact impedance of the electrodes.

In this chapter, we investigate image artifacts caused by our shape change models. We model shape changes in 2D simply as elliptical shape distortions of a unit disk boundary. In 2D EIT image reconstruction, an object is often assumed to have circular boundary. Our motivation is that parts of human body generally have elliptical profiles rather than circular. We describe elliptical shape change by the Joukowski transformation, which can define the relation between circular and elliptical geometries. Based on the relation, correct reference measurements can be obtained from the solution of the circular domain (Lionheart 1998). We demonstrate a method to estimate shapes as ellipses defined by a single geometrical parameter of the Joukowski transformation (the *Joukowski parameter*). In our method, images of artifacts due to elliptical shape changes, which we use as a template, are obtained from measurements made on homogeneous elliptical domains of various eccentricities. Images reconstructed from actual measurements may then be compared with the template to find the ellipses that produce the best match.

In order to validate our method, analysis was done with simulated measurements with and without added noise; and phantom measurements (elliptical phantoms filled with saline solution as a background material). Data were gathered using the adjacent electrode configuration with 16-electrode full array, and images were generated using TSVD regularized reconstruction method.

Method

In 2D EIT reconstruction, the domain is often assume to be circular when the accurate shape of the model is unavailable. However, cross-sections of body parts such as abdomen or

chest are noticeably more elliptical in profile than circular. Here, we investigate shape changes simply as elliptical boundary distortions on a disk model (Oh *et al.* 2007).

The Joukowski Transformation and Elliptical Boundary Shape Change

Conformal mapping is an angle-preserving transformation, meaning that the angle between any arbitrary two vectors is preserved after the transformation. It is useful when the difficulty of a problem can be expressed in terms of geometry. According to the Riemann's theorem, any object with closed boundary can be mapped conformally into a unit circle. The Joukowski transformation can describe a conformal relation between elliptical and circular geometries as in Equation 4-1. We use the Joukowski transformation to model elliptical shape changes.

$$W = g(Z) = Z + c \frac{1}{Z}, \quad (4-1)$$

where c is termed the *Joukowski parameter*. In Equation 4-1, the relation $g(Z)$ is conformal, and Z and W are complex numbers that represents spatial coordinates of the electrodes. Z denotes the boundary points of a unit circle and W those of an ellipse. The main axes of the ellipse are $1 + c$ in length horizontally and $1 - c$ vertically (Appendix A). Therefore, c is a geometrical parameter of an ellipse determining degrees of elliptical shape changes.

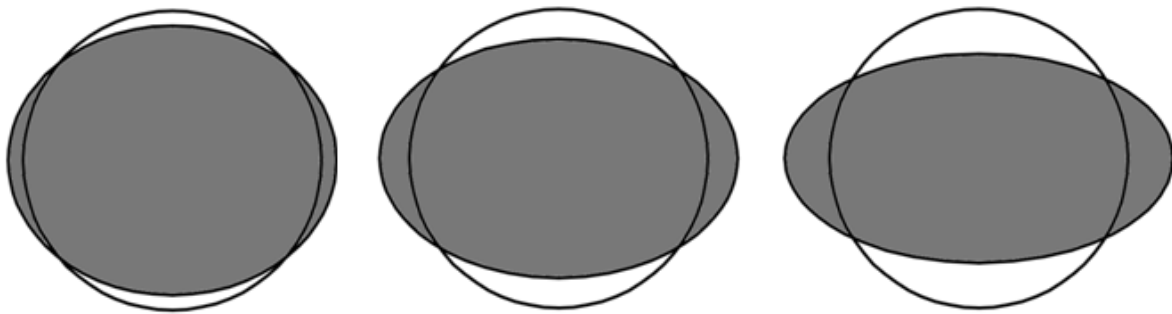


Figure 4-2. A 2D disk model after three different degrees of elliptical shape change ($c = 0.1, 0.2$ and 0.3) under the Joukowski transformation.

In Figure 4-2, we illustrated three different degrees of changes ($c = 0.1, 0.2$ and 0.3), and laid the initial disk model of no shape change over the ellipses.

Reference boundary voltage measurements are initially obtained from a disk object using equidistant boundary electrodes. After the shape change, it is apparent that the object is no longer a disk, thus the initial reference measurements are incorrect. The correct reference measurement can be obtained conveniently from the forward solution of the disk domain. In Figure 4-3, due to the Joukowski transformation, locations of the boundary electrodes have changed, with electrodes near the x -axis having experienced larger shifts along the circular arc than the ones near the y -axis. Assuming that the electrodes had been placed equidistantly on the elliptical boundary, the correct reference measurements were obtained from the circular model using electrodes with shifted locations by the inverse transformation ($g^{-1}(W)$) of the Equation 4-1.

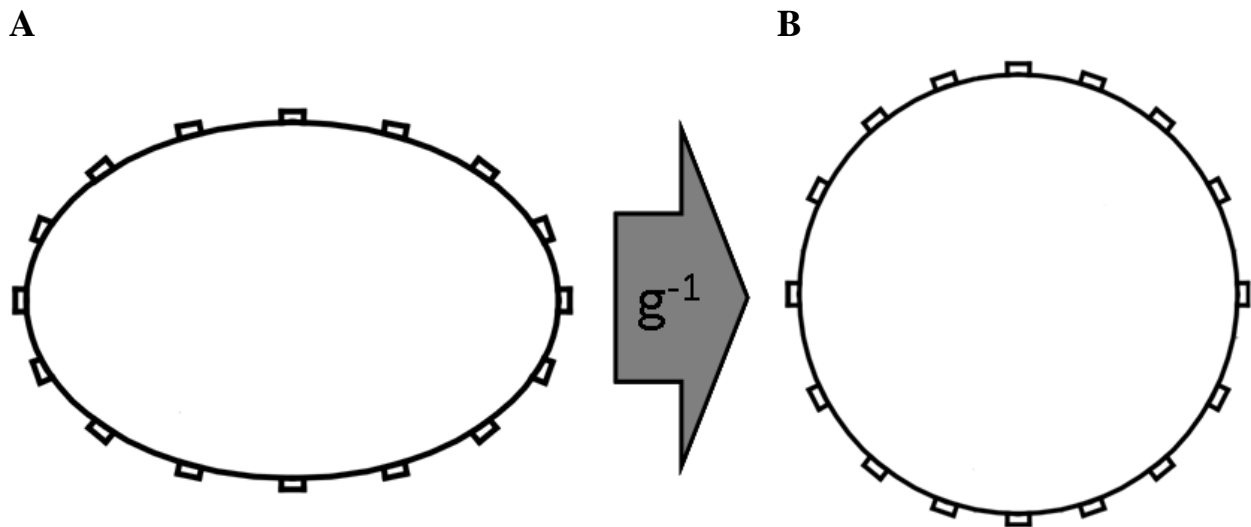


Figure 4-3. Inverse Joukowski transformation of an elliptical domain with 16 equidistant boundary electrodes. A) Elliptical domain ($c = 0.2$) with equidistant boundary electrodes. B) Disk domain with non-equidistant boundary electrodes whose locations are shifted by the inverse Joukowski transformation.

Boundary voltage change (ΔV) after the elliptical shape change is obtained as follows.

First, the reference boundary voltage (V_0) was measured on a 2D disk object (radius: $r_d = 1$) of

homogeneous conductivity using the 16-electrode full array attached on its boundary. Then, various amounts of elliptical shape changes were applied on the disk object containing a single disk anomaly (radius: $r_a = 0.1$) at its center. The boundary voltages (V_e) were measured using electrodes with shifted locations (by $g^{-1}(W)$) on circular boundary (4-1). Finally, the measurement set (ΔV_e) due to elliptical shape change was obtained by subtracting the reference V_0 from V_e as in Equation 4-2.

$$\Delta V_e = V_e - V_0 \quad (4-2)$$

In Figure 4-4, measurements are displayed for three degrees of elliptical shape change ($c = 0, 0.01$ and 0.1). The main attribute of measurement errors due to shape change is sharp spurious peaks near the domain boundary. In Figure 4-4, peak amplitudes are observed to grow as c values increase. It is also apparent that the measurements are completely dominated by this shape change over $c = 0.1$.

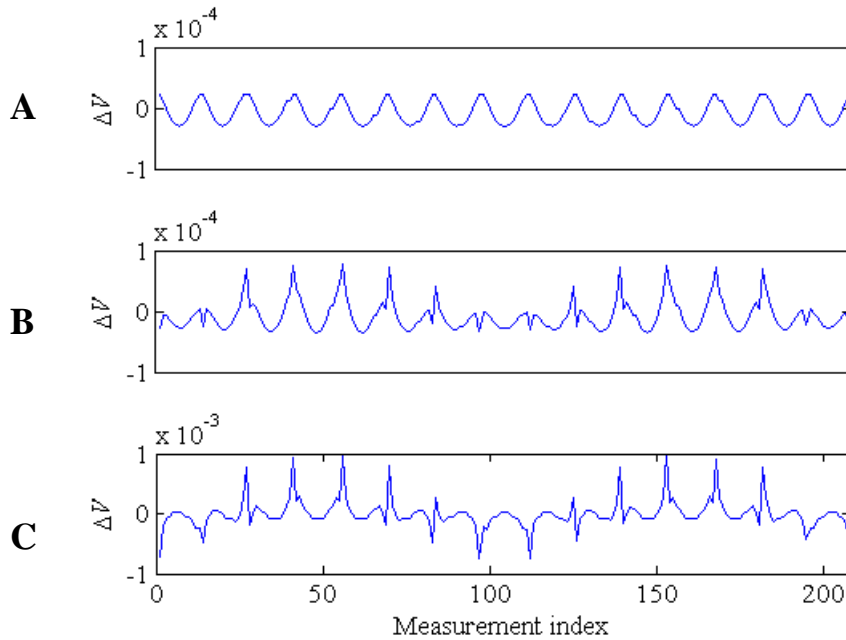


Figure 4-4. Measurements made on the disk model. A) of no shape change ($c = 0$), B) of elliptical shape change $c = 0.01$ and C) $c = 0.1$.

Conductivity images were produced from ΔV_e using TSVD regularized reconstruction as in Equation 4-3.

$$\Delta\sigma_e = \mathbf{S}^+ \Delta V_e, \quad (4-3)$$

where $\Delta\sigma_e$ is the conductivity change reconstructed from ΔV_e . Artifacts in the images occur, because effects of the shape change on reconstruction images are through compensatory conductivity changes within the domain (Tossavainen *et al.* 2004). Figure 4-5 shows images greatly corrupted by the shape change artifacts, whose peak amplitudes increased with c .

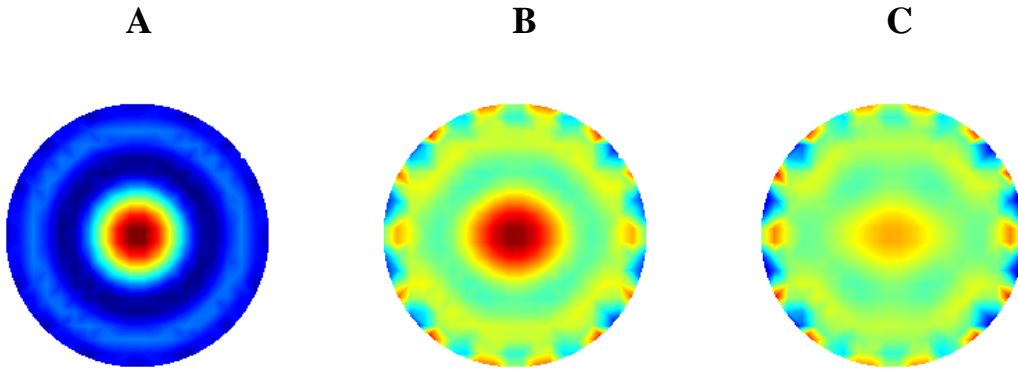


Figure 4-5. Reconstruction image from the measurement on a disk object containing an anomaly at the center. A) No shape change ($c = 0$), B) elliptical shape change ($c = 0.1$), and C) elliptical shape change ($c = 0.2$). Images were reconstructed using TSVD with truncation at 63.

In Figure 4-6, the absolute maximum and minimum of $\Delta\sigma_e$ values, which represent positive and negative artifact peaks respectively, are plotted for various c values. Results of linear fits to these curves allowed several findings: The increase of positive peaks was more linear, while that of negative peaks was more rapid for increasing amount of the shape change. In order to investigate shape change in quantitative EIT, average of $\Delta\sigma_e$ (an analog of QI) was calculated and plotted in terms of c (Figure 4-7). The average of $\Delta\sigma_e$ decreased as c increased, and it went below zero at about $c = 0.15$. Additionally, QI errors were less than 5% for shape

changes whose degrees (c) were less than 0.5 (Oh *et al.* 2007). Therefore, shape change is seen to be a more important issue in imaging than in quantitation.

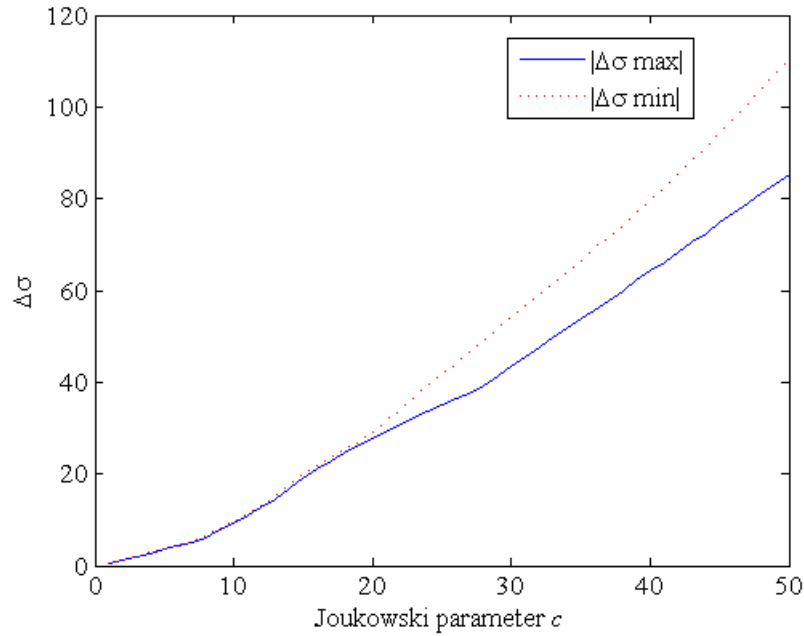


Figure 4-6. Absolute values of maximum and minimum of reconstruction amplitude ($\Delta\sigma$) for various degrees of shape change c (%).

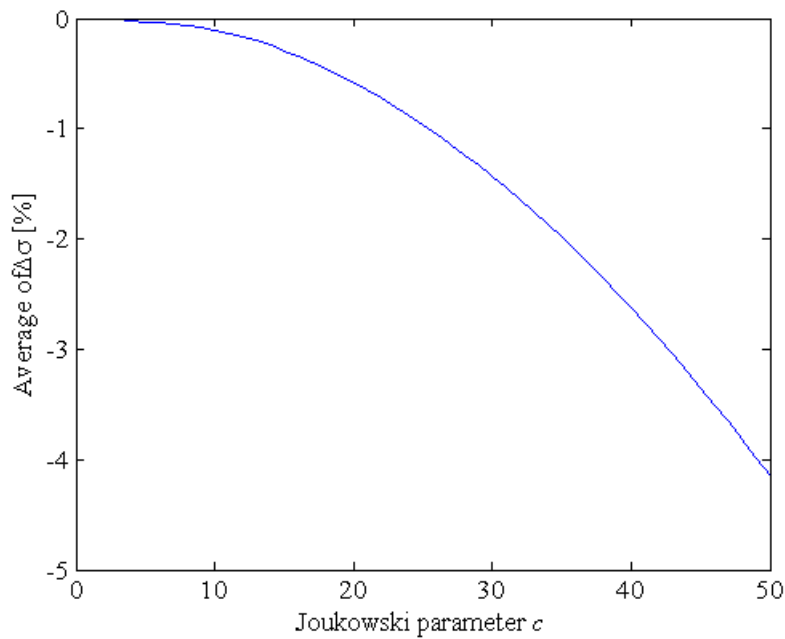


Figure 4-7. QI vs. the degrees of shape change (*Joukowski parameter: c (%)*).

Boundary Shape Estimation

Artifacts due to shape changes are undesirable in reconstructed images, but they may contain concentrated information about shape changes. The main attributes of the artifacts were found to be high amplitude peaks with alternating signs near the object boundary (Figure 4-5). The TSVD reconstruction seems to have a tendency to push the artifacts close to the boundary. We also found that the peak magnitude of the boundary artifacts increased consistently with c (Figure 4-6), while their patterns were relatively preserved (Figure 4-5). Based on these findings, we suggest a method to estimate elliptical boundary shape from EIT reconstruction (Figure 4-8). Our method estimates the changed shape as an ellipse, defined by a single geometrical parameter c (the *Joukowski parameter*) as in Equation 4-1.

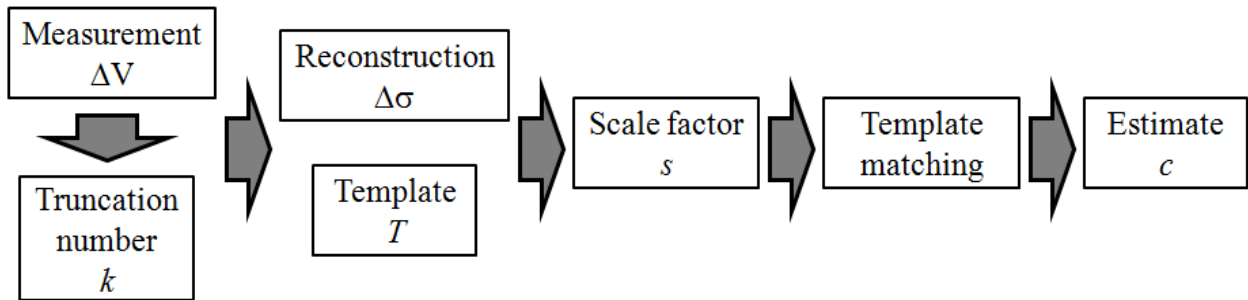


Figure 4-8. Summary of our method to estimate boundary shape.

In Equation 4-3, images of reconstructed conductivity $\Delta\sigma_e$ were obtained by TSVD. Because the artifacts due to shape changes collect mainly in the region near the boundary, we selected a group of elements (pixels) near the boundary (Figure 4-9), and denoted them collectively as J . Finally, a template T was defined as the reconstruction pixel values ($\Delta\sigma_e$) in J that depends on c as in Equation 4-4 (Figure 4-10).

$$T(c) = \Delta\sigma_e(J, c) \quad (4-4)$$

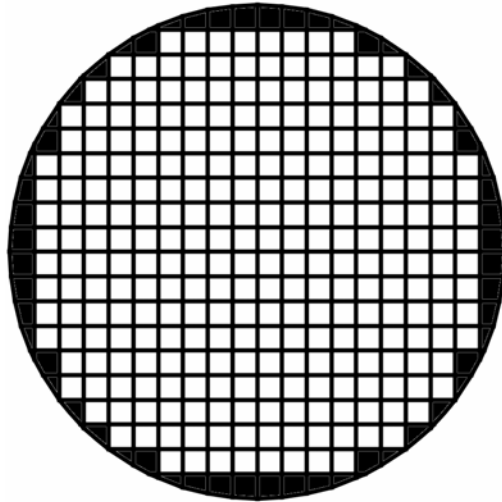


Figure 4-9. The boundary elements that were used for the template (filled with color).

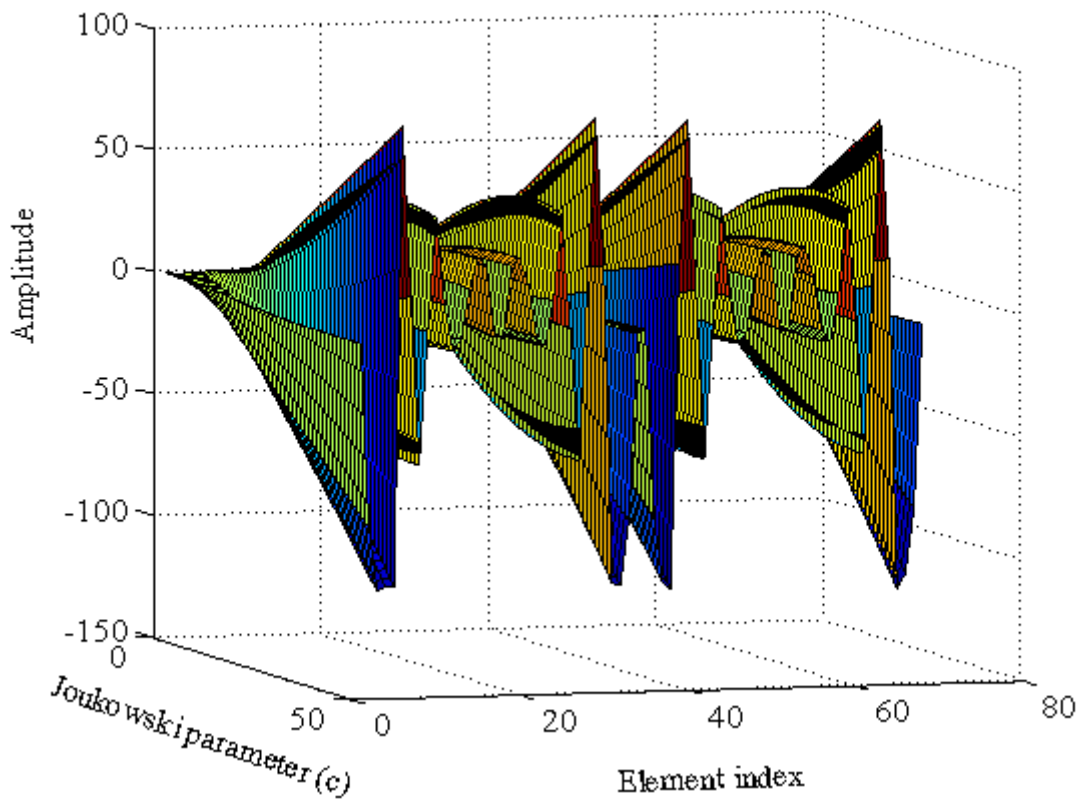


Figure 4-10. Template vs *Joukowski parameter* ($c = 0 \sim 50\%$).

Typically in EIT, accurate knowledge of boundary shape is unavailable, but conductivity change $\Delta\sigma_a$ reconstructed by these actual measurements can readily be compared with $T(c)$. Now, the shape change can be estimated by finding the c value that produces the least sum of squared errors as in Equation 4-5.

$$\arg \min_c \left\{ \sum_J (\Delta\sigma_a(J) - T(c))^2 \right\} \quad (4-5)$$

Method in Equation 4-5 often fails when the mean difference is large between T and $\Delta\sigma_a$. In order to resolve this problem, we considered a scale factor (s) that was defined as the ratio of the maximum pixel values of $\Delta\sigma_a$ and T as in Equation 4-6.

$$\arg \min_c \left\{ \sum_J (s^{-1} \cdot \Delta\sigma_a(J) - T(c))^2 \right\} \quad (4-6)$$

Computer Simulation

We designed a 2D disk model ($r_d = 1$) with 16-electrode full array using Comsol Multiphysics and Matlab. All electrodes had the conductivity of copper ($5.99 \times 10^7 [\text{Sm}^{-1}]$). The length of each electrode was 0.1, and subtended an angle of 5.7° on its circular boundary. The models were discretized to 1916 second-order triangular finite elements, and then solved using the direct linear system solver UMFPACK (Unsymmetric MultiFrontal PACKage). The model contained a small disk anomaly ($r_a = 0.1 \times r_d$) placed at one of five different locations (relative radial distances of: 0, 0.2, 0.4, 0.6 and 0.8 from the origin) on the positive x axis. The model background conductivity was set to one, and anomalies represented a unit conductivity increase from the background.

Actual measurements ΔV_e as in Equation 4-2 were obtained using adjacent electrode configuration for the model undergoing five different degrees ($c = 0.1, 0.2, 0.3, 0.4$ and 0.5) of the elliptical shape change described by the Joukowski transformation.

Phantom Experiment

We constructed an acrylic cylindrical tank ($r_P = 14.0$ cm) as shown in Figure 4-12. Sixteen stainless steel bar electrodes (13.0 mm \times 10 cm) were attached equidistantly around the tank inner surface. Image sensitivity decreases significantly when anomaly volume is outside the electrode plane (Metherall P *et al.* 1996), so we used vertically extended electrodes previously used in the study by Sadleir and Fox (1998). A hole was drilled on each electrode center, and the same sized holes were drilled on the tank wall at a certain height (6.5 mm) from the bottom. Bolts were inserted so that the threaded parts stick outward. They were fastened while being checked for any water leak. Finally, the bolts were connected to 16 channels of the external measurement system.

The tanks were filled with 5 L of saline solution ($\sigma = 0.2$ Sm⁻¹) as a background material. The surface level of the saline solution inside the tank was within the height of the bar electrodes. Two insulating plastic rods of radii (r_A) 1.3 cm and 1.8 cm were used as anomalies I and II. Anomalies I and II were placed at 9 and 5 different locations respectively, on the positive x axis. The displacement from the phantom center was from 0 to 11.2 cm with 1.4 cm gaps for anomaly I, and with 2.8 cm gaps for anomaly II.

The elliptical phantoms were designed (Figure 4-11) to approximate $c = 0.1$ and 0.2 shape change applied to the cylindrical phantom shown in Figure 4-12. The lengths of semi-major and semi-minor axes of the elliptical plane were 15 cm and 12.5 cm (elliptical phantom I), and 16 cm and 11.5 cm (elliptical phantom II). The c values of these ellipses were calculated to be 0.09 and 0.16 respectively.



Figure 4-11. Elliptical phantoms simulating two different degrees of shape change ($c = 0.1$ and 0.2). The 16 stainless steel bar electrodes are attached on the elliptical boundary equidistantly.

Another phantom ($r_p = 10.0$ cm) was constructed from a flexible plastic bucket (Figure 4-13). This phantom was filled with 4 L of saline solution. In this phantom, shape changes could be applied by inserting flat objects beneath the base of the phantom to distort the boundary shape, thus resulting in the upper cross-sections of the bucket to become more distorted than the lower. Four increasing degrees of elliptical shape change were applied in this manner. This type of shape change was deemed to approximate real body shape changes more closely than the elliptical phantoms (i.e. abdominal breathing).

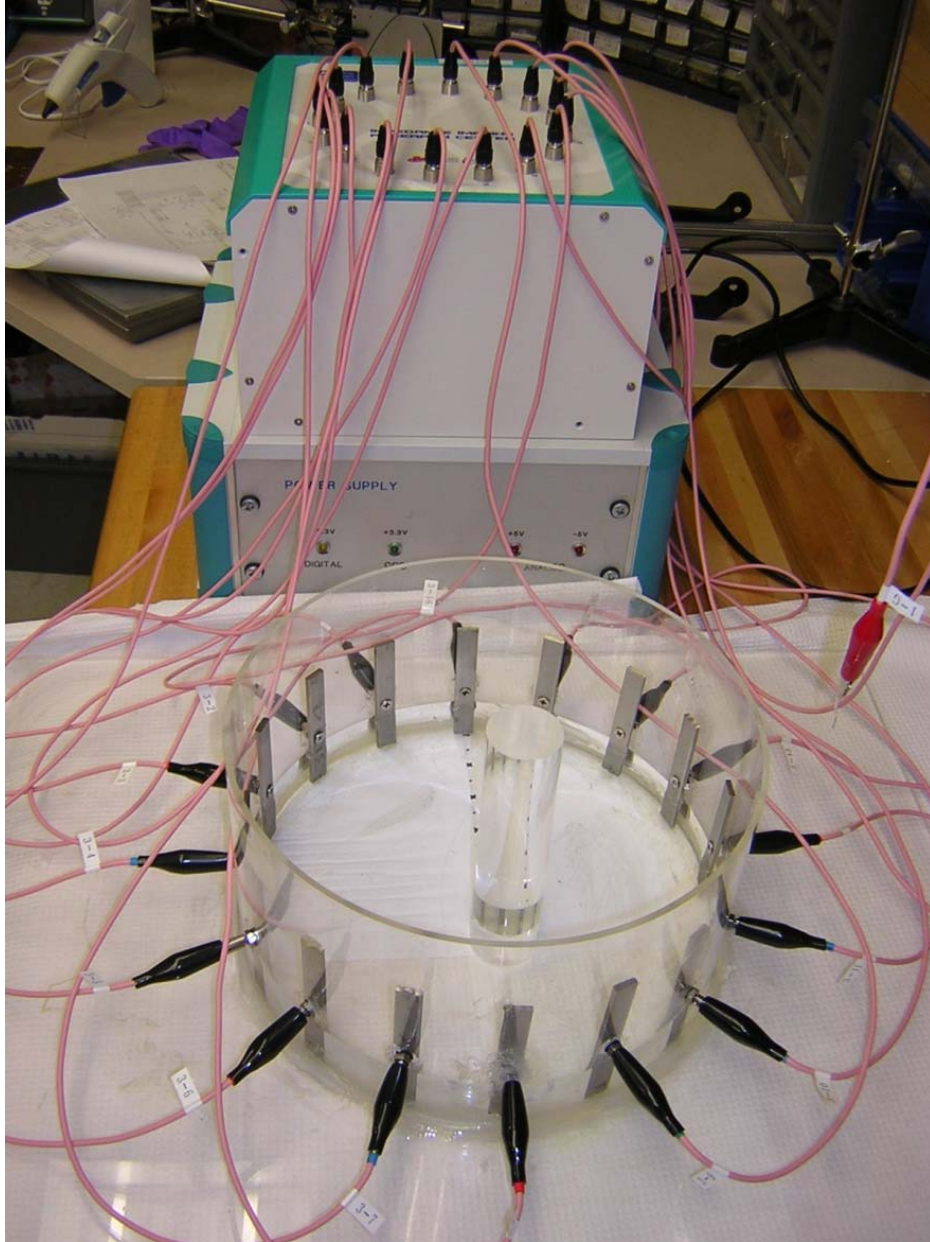


Figure 4-12. Prototype KHU Mark1 with 16 channels applied to a cylindrical phantom.

Data were obtained using a prototype of KHU Mark1 system (Figure 4-13). KHU Mark1 is an EIT system developed in the Impedance Imaging Research Center (IIRC), Kyung Hee University (KHU), Suwon, Korea. The system allows flexibility for addressing electrodes, with a wide range of operating frequency (10 kHz ~ 500 kHz) (Oh *et al.* 2007). We collected measurements at 10 kHz for input current applied at 1 mA.



Figure 4-13. A malleable cylindrical phantom with 16 bar electrodes.

Results

Simulated Data

Figure 4-14 shows reconstructed images with an anomaly at each of five different positions for an elliptical shape change ($c = 0.2$). The shape change affected images of a central anomaly more, and the patterns of the artifacts near the domain boundary are similar.

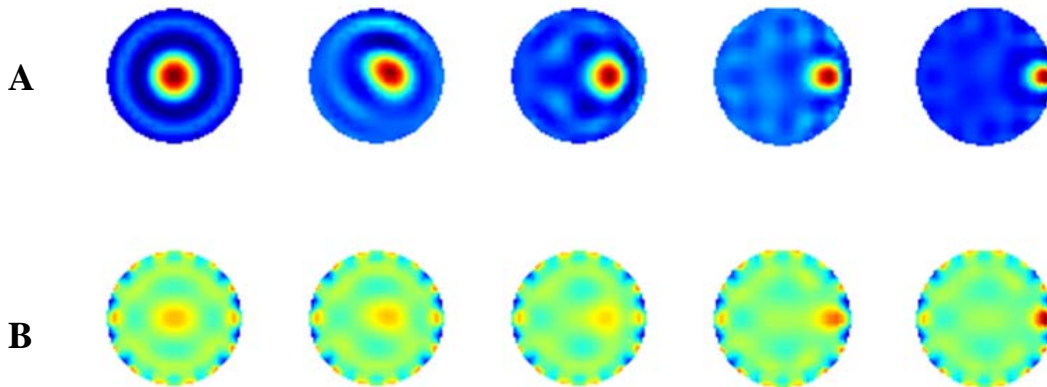


Figure 4-14. Reconstructed images for a single anomaly on five different locations. A) before and B) after shape change ($c = 0.2$)

For noiseless measurements, the results of shape change estimation are shown in Figure 4-15. In Figure 4-15 (A), the minimum of the cost function is seen to correspond exactly to the degree of the shape change applied ($c = 0.2$). We used the estimated shape information to obtain the reference measurement, which was applied to reconstruction and improved image quality greatly (Figure 4-15 (B)).

The White Gaussian Noise (WGN) of 20dB Signal-to-Noise Ratio (SNR) was added to corrupt these simulated measurements. Results in Figure 4-16 shows that the overall errors were only about 2% for shape changes up to $c = 0.5$ (50%).

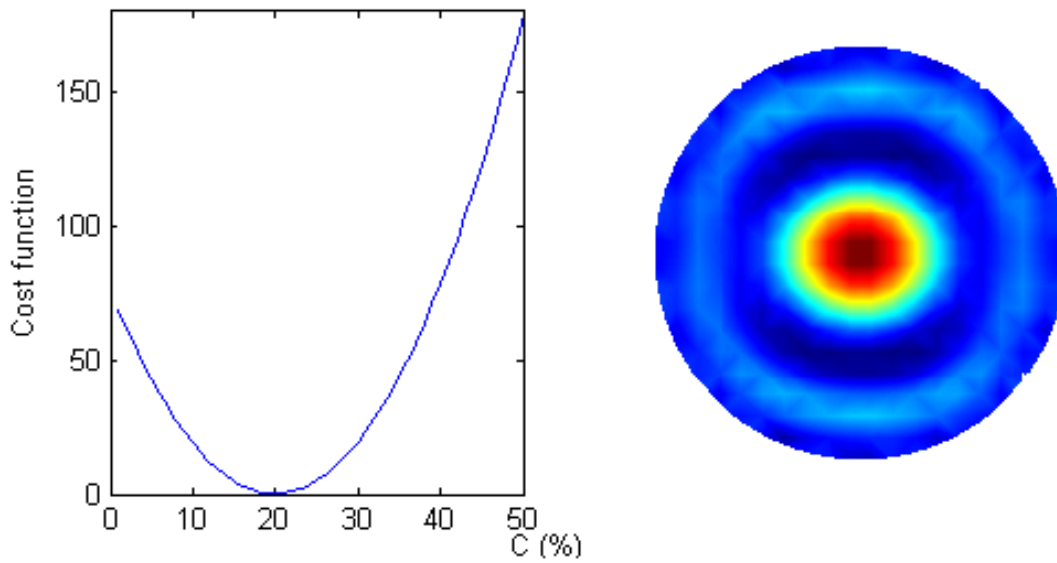


Figure 4-15. Cost function curve for estimating the amount of shape change. Reconstructed image recovered using the estimated shape information is shown on the right.

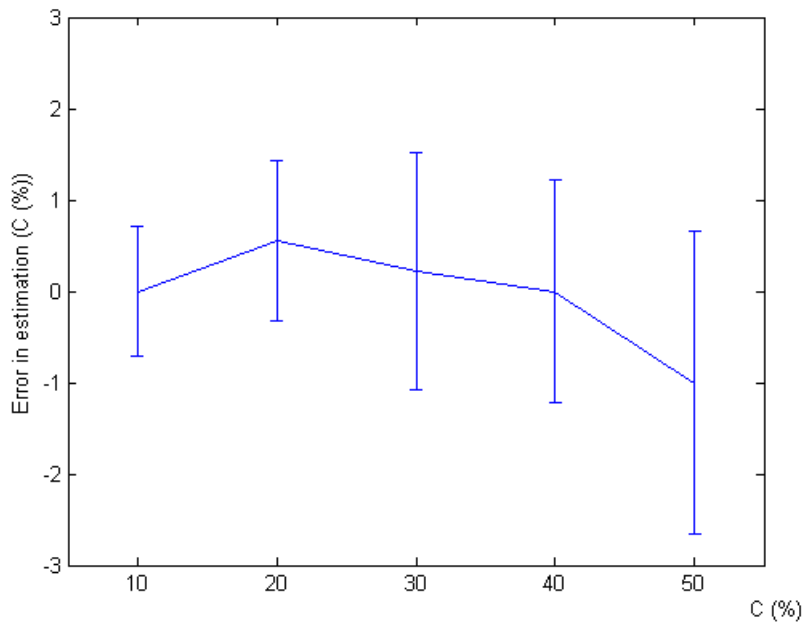


Figure 4-16. Estimation errorbar plot for various amounts of shape change (c). Measurements were noisy with additive WGN of 20dB SNR.

Phantom Data

We estimated c values from the measurements made on the cylindrical and elliptical phantoms. In Table 4-1, the estimated values of c were averaged across anomaly locations and expressed in percentile. The results show that we succeeded in estimating c with discrepancies less than 0.04. The scale factor ($s = 1.5017 \times 10^5$) was calculated from the reconstruction of the cylindrical phantom.

In the malleable phantom case, shape-change corrupted measurements (Figure 4-17) did not match the characteristics of the simulated as previously shown in Figure 4-4.

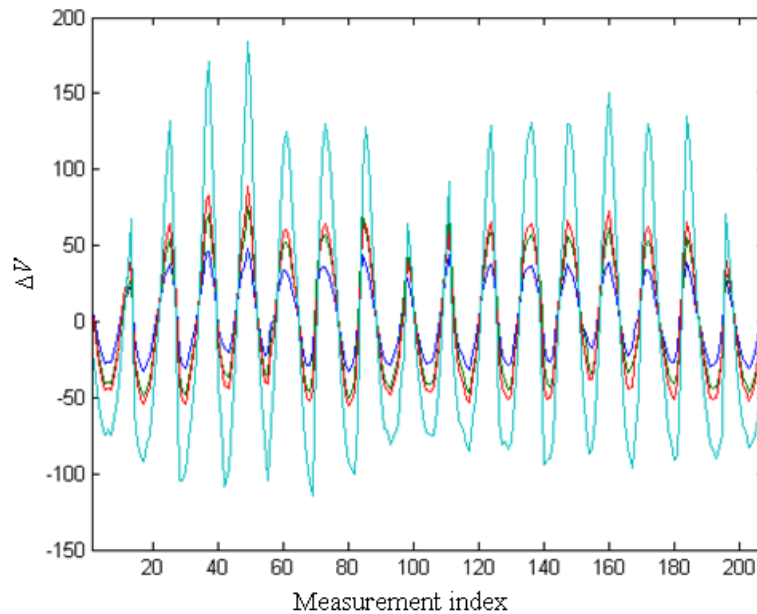


Figure 4-17. Reference measurements from homogeneous medium for four different amounts of shape change

However, we confirmed the spatial characteristics of boundary image artifacts for both were similar. Using our method, c values were estimated as in Figure 4-18. We do not know what the c value was for each shape change, but Figure 4-18 at least shows monotonous increase for increasing amounts of shape change.

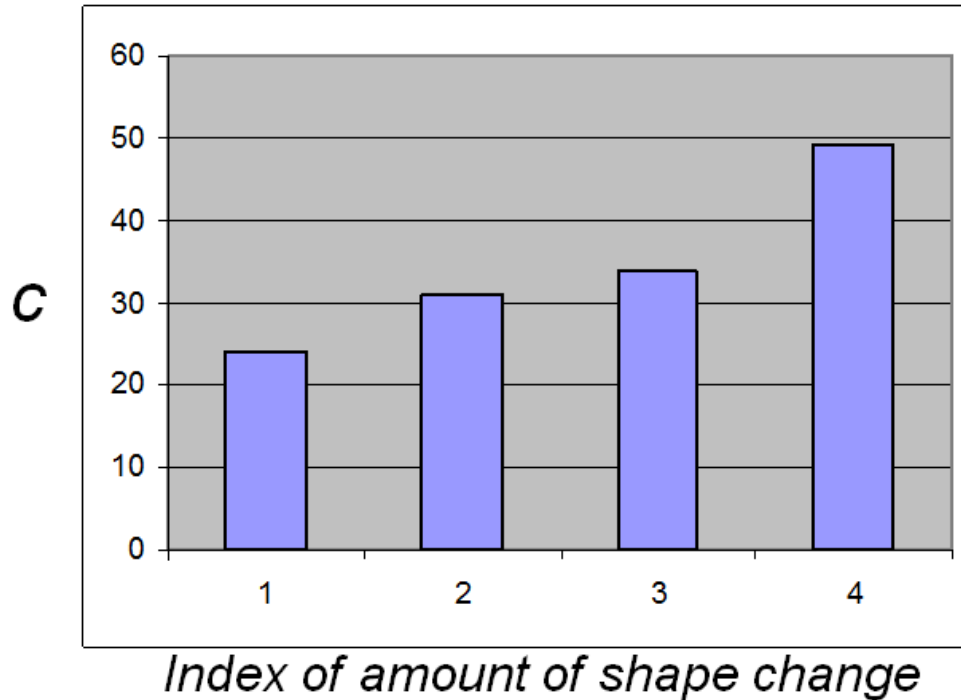


Figure 4-18. Elliptical boundary shape estimation by the *Joukowski parameter c* (%). Four different degrees of shape change were applied on a malleable plastic phantom in an increasing order.

Discussion and Conclusion

We developed our method motivated by our observation that the reconstruction process naturally divides influences of conductivity distribution and boundary shape change. Artifacts due to boundary shape changes were observed to cause spurious boundary peaks, which were used as features to estimate elliptical shape changes. Utilizing the reference measurement obtained from a homogeneous model of the estimated shape, we recovered the original image quality.

We were roughly able to estimate shape changes from the simulated measurements with and without AWGN, and phantom measurements. Phantoms were made either to be elliptical or to be malleable so that approximately elliptical shape distortions can be applied. For simulated model of $c = 0.5$ shape change, estimation errors were under 5% in the presence of 20 dB SNR

AWGN. In phantom experiments, we could always estimate approximate values of c (Table 4-1 and Figure 4-18).

Table 4-1. Estimated c (percentile) from the measurements made on cylindrical and elliptical phantoms I and II. Anomaly I ($r_A = 1.3$) was positioned in nine different locations, and Anomaly II ($r_A = 1.8$ cm) in five locations. The c values were averaged across anomaly position.

| | Cylindrical | Elliptical I | Elliptical II |
|-----------------------------------|-------------|--------------|---------------|
| Expected c values | 0 | 9 | 16 |
| Estimated c values (Anomaly I) | 1 | 12 | 19.9 |
| Estimated c values (Anomaly II) | 1 | 11.8 | 19.6 |

The method by Soleimani *et al.* (2006) successfully reconstructed images of reduced artifacts for both conformal and non-conformal shape changes. However, a recent investigation by Boyle *et al.* (2008) found that it could not estimate conformal shape changes. Our proposed method is a template-matching algorithm and does not modify the reconstruction matrix. As long as changes of domain shapes produce similar boundary artifacts, our method is expected to always find an approximate estimation of the changed shape.

In Figure 4-19, areas of the ellipses transformed from a unit circle via the Joukowski transformation are plotted in terms of c . The area of ellipse can be calculated as $\pi(1 + c)(1 - c)$. For $c = 0.1$, the difference between the cross-sectional areas of the original and changed models is about 1% of the original area. Therefore, we regarded the Joukowski transformation to be an appropriate model for most body shape changes that are typically $c = 0.1$ and below. However, it would still be interesting to investigate realistic cross-sectional area changes of the subject domain. The results from this investigation could be utilized for further improvements in image quality.

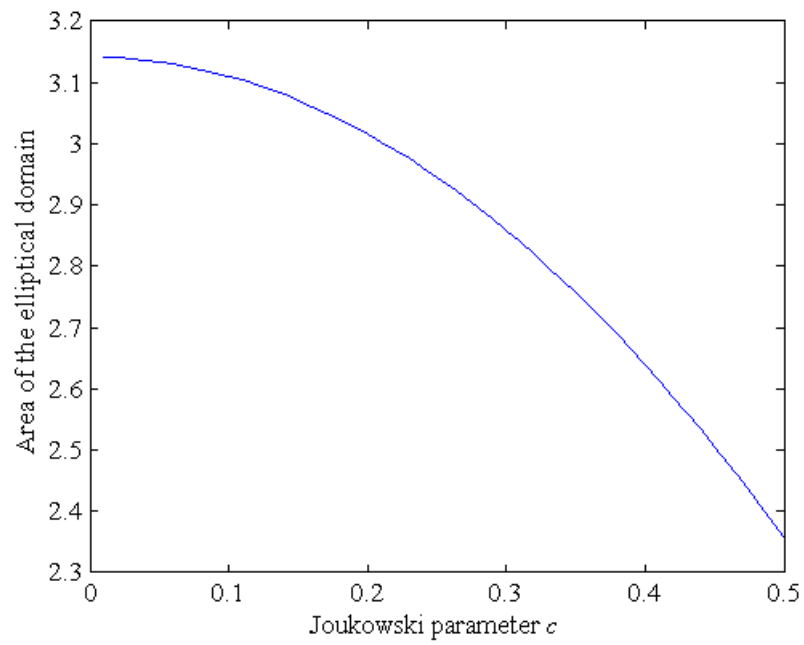


Figure 4-19. Area of the domains for the elliptical shape change of various degrees (c).

CHAPTER 5
NORMALIZATION OF SPATIALLY-VARIANT IMAGE RECONSTRUCTION PROBLEM
IN EIT USING SYSTEM BLURRING PROPERTIES

Background

Previous works suggested quantitative EIT as a potential method to monitor volume changes inside the body. Exemplary areas include air and liquid in the lungs and bleeding in the peritoneum. Relevant in-vivo experiments were done in monitoring dynamic hyperinflation in dogs (Adler *et al.* 1998) and fluid volume changes in Continuous Ambulatory Peritoneal Dialysis (CAPD) (Sadleir and Fox 2001).¹

A main challenge in quantitative EIT is the errors related with the spatial variability of EIT imaging systems. The image amplitude of a conductive anomaly varies with its position (Sadleir and Fox 1998). In monitoring changes of lung air and liquid volumes, Adler *et al.* (1997) reported errors that depended on radial positions of a same anomaly, despite exclusion of a noisy region near the object boundary. Spatial variability in quantification may not be a significant problem when the region of interest (ROI) is relatively small. In Blott *et al.*'s study (2000) of simulated two-dimensional intra-ventricular hemorrhage, quantitation errors due to spatial variance were likely negligible for that reason. However, determining an ROI is not straightforward for some applications. In intra-peritoneal hemorrhage application, bleeding may occur over a large fraction of the imaged domain (Sadleir and Fox 1998). Therefore, reducing effects of the spatial variability on estimating quantities is desired to improve accuracy of quantitative EIT reconstruction.

¹ This chapter was published in *Physiological Measurement*, volume 30, pages 275-289 in 2009. The work was supported in part by NIH grant R01EB-002389, and by the US Army Medical Research and Materiel Command under Award No. w81xwh-07-1-0591, both to RJS.

In order to reduce variations in quantity estimates, Thomas *et al.* (1994) used a method that scaled log-resistivity images pixel-wise. A study by Sadleir and Fox (1998) demonstrated a post-reconstructive filtering method that combined pixel-wise scaling and conformal transformations in the context of a linearized back-projection method.

The problem of a spatially variant imaging system was investigated in detail by Wheeler *et al.* (2002) in the context of resolution measures. In order to identify the resolution of EIT images, spatially invariant measures were sought. In their comparative study, an area integral measure turned out to be the most robust against spatial variance.

We used reconstruction blur analysis in order to reduce errors caused by spatial variance. We demonstrate that normalizing the Point Spread Function (PSF) by its integral can result in improvements. Cohen-Bacrie *et al.* (1997) used variance of this PSF as penalty term in Tikhonov regularization. In our case, we used integrals of PSF functions as normalizing terms. Three mathematical frameworks of normalization were compared: Pixel-Wise Scaling (PWS), Weighted Pseudo-Inversion (WPI) and Weighted Minimum Norm Method (WMNM) for two-dimensional eight electrode *full array* and *hemiarrray* reconstructions. Data were obtained from numerically simulated two-dimensional disk models containing simulated disk anomalies placed at various locations in the image plane and a cylindrical saline phantom containing blood-like anomalies in a less-conducting background.

Method

Point Spread Function and the Blur Matrix

In this chapter, we introduce the point spread function (PSF) in order to investigate blurring in EIT image reconstruction. Consider a unit conductivity change in an element (pixel) j within the image. This unit change can be expressed in a vector form as an entry of 1 in the j -th position and zeros elsewhere ($[0 \dots 0 \ 1 \ 0 \dots 0]^T$) ($I \times N$), whose weighted sum is a vector form of

the ideal image. The change in boundary voltage measurements subject to this unit conductivity change is the j -th column of the sensitivity matrix \mathbf{S} ($M \times N$). Ideally any measurement can be represented as a weighted sum of sensitivity matrix columns. Therefore, the column space of \mathbf{S} can be termed the *ideal measurement* space. By reconstructing from the ideal measurements, a blurred version of the ideal element (pixel) image is obtained, which we term the *PSF* in Equation 5-1.

$$\delta_j = \mathbf{B} [0 \ \dots \ 0 \ 1 \ 0 \ \dots \ 0]^T, \quad (5-1)$$

where \mathbf{B} ($N \times N$) is the *blurring matrix*, and δ_j is the PSF vector for an anomaly in the j -th element. The column space of \mathbf{B} is a blurred version of the ideal images. The blur matrix \mathbf{B} is defined as a product of the sensitivity matrix and the reconstruction matrix. Therefore, it can be easily obtained for any reconstruction matrix that is expressed in algebraic form. In Equation 5-2a and Equation 5-2b, definitions of \mathbf{B} are displayed in the context of TSVD and WMNM regularizations respectively.

$$\mathbf{B} = \mathbf{S}^+ \mathbf{S} \quad (5-2a)$$

$$\mathbf{B} = \mathbf{W}(\mathbf{S}\mathbf{W})^+ \mathbf{S} \quad (5-2b)$$

It should be noted that one can easily obtain \mathbf{B} for other regularization methods such as Tikhonov regularization in Equation 3-22. The definition of \mathbf{B} for Tikhonov regularization is shown in Equation 5-3.

$$\mathbf{B} = \left((\mathbf{S}^T \mathbf{S} + \lambda \cdot \mathbf{I})^{-1} \mathbf{S}^T \right) \cdot \mathbf{S} \quad (5-3)$$

Using SVD, we can estimate basis images that determine the system blurring \mathbf{B} .

$$\mathbf{B} = \mathbf{S}^+ \mathbf{S} \quad (5-4a)$$

$$= (\mathbf{U}\mathbf{D}\mathbf{V}^T)^+ (\mathbf{U}\mathbf{D}\mathbf{V}^T) \quad (5-4b)$$

$$= \mathbf{V}\mathbf{D}^+\mathbf{D}\mathbf{V}^T \quad (5-4c)$$

$$= \mathbf{V} \begin{bmatrix} \mathbf{I}_k & \mathbf{0} \\ \mathbf{0} & \mathbf{0} \end{bmatrix} \mathbf{V}^T, \quad (5-4d)$$

where \mathbf{I}_k ($k \times k$) is the identity matrix. It is clear from Equation 5-4d that columns of the right singular matrix \mathbf{V} can be seen as eigen-image vectors. It is also clear that the blurring depends on the truncation number k .

Normalizing Terms

In order to normalize QI, the column sum of \mathbf{B} , defined as q_j in Equation 5-5, was considered.

$$q_j = \left(\sum_{i=1}^N \mathbf{B}_{ij} \right) \quad (5-5)$$

The normalization matrix used throughout this paper is defined as \mathbf{Q} ($N \times N$) as in Equation 5-6, which is a diagonal matrix whose entries are q_j 's.

$$\mathbf{Q} = \begin{bmatrix} q_1 & 0 & \cdots & 0 \\ 0 & q_2 & 0 & \vdots \\ \vdots & 0 & \ddots & 0 \\ 0 & \cdots & 0 & q_N \end{bmatrix} \quad (5-6)$$

Pixel-wise Scaling

Thomas *et al.* (1994) used a method that scaled log-resistivity images pixel-wise in order to reduce variation in quantity estimates. We can also apply pixel-wise scaling (PWS) to our case in which conductivity change is to be reconstructed. In Equation 5-7, PWS is presented in matrix form.

$$\Delta \hat{\sigma} = \mathbf{Q}^{-1} \mathbf{S}^+ \Delta V \quad (5-7)$$

A more advanced method was proposed by Sadleir and Fox (1998), who demonstrated a post-reconstructive filtering method that combined pixel-wise scaling and conformal

transformations. In their work, the maximum spatial error in quantitation from phantom experimental results decreased from 30% to 6%. However, a large region near the object boundary (normalized radius > 0.75) was excluded from quantification.

Weighted Pseudo-inverse

The normalization that we use here is weighted pseudo-inversion (WPI). The normalized reconstruction can be obtained by weighting columns of the sensitivity matrix by terms in \mathbf{Q} prior to reconstruction as in Equation 5-8.

$$\Delta \hat{\sigma} = (\mathbf{SQ})^+ \Delta V \quad (5-8)$$

If \mathbf{SQ} is a full-rank matrix, Equation 5-8 will become identical to Equation 5-7. In this vein, we speculate that WPI should normalize the reconstruction in a similar way to PWS, with an additional advantage of using the truncated pseudo-inverse.

WMNM Normalization

In the work of Oh and Sadleir (2007), a WPI method was shown to decrease spatial variance of the QI. However, the normalized reconstruction in Equation 5-8 did not produce reasonable images. To obtain meaningful images, one can borrow the mathematical framework of WMNM, which can be done by multiplying \mathbf{Q} post-reconstructively. The final form is shown in Equation 5-9.

$$\Delta \hat{\sigma} = \mathbf{Q}(\mathbf{SQ})^+ \Delta V \quad (5-9)$$

It was also noticed that the WMNM framework can be used to introduce normalization effects in some cases. Sadleir *et al.* (2008) used a combined method of WMNM regularization in Equation 3-19 and WMNM normalization in Equation 5-9 in the eight electrode hemiarray case, which produced normalized QIs and images. The matrix equation of this normalized reconstruction method is shown in Equation 5-10.

$$\Delta \hat{\sigma} = \mathbf{QW}(\mathbf{SWQ})^+ \Delta V \quad (5-10)$$

Normalized Sensitivity Matrices

The pseudo-inverted part of the reconstruction matrix can be understood as pseudo-inversion of a matrix product of the normalization matrix (\mathbf{Q}_t or \mathbf{Q}_w) and the sensitivity matrix (\mathbf{S}). Matrices \mathbf{Q}_t and \mathbf{Q}_w were calculated using differing definitions of the \mathbf{B} matrix as shown in Equation 5-2a and Equation 5-2b respectively. Changes of the system matrix condition number owing to this matrix multiplication are presented in Table 5-1.

Table 5-1. Condition numbers of the normalized system matrices

| System matrix | Condition Number (full array) | Condition Number (hemiarrray) |
|------------------------|----------------------------------|----------------------------------|
| S | 2.21×10^{17} | 2.02×10^{18} |
| SW | 2.00×10^{17} | 3.21×10^{18} |
| SQ_t | 6.37×10^{17} | 3.93×10^{17} |
| SWQ_w | 2.31×10^{17} | 2.51×10^{18} |
| SWQ_t | 2.05×10^{17} | 4.10×10^{17} |

Table 5-1 shows that matrix conditions can improve depending on the choice of the normalization matrix. For a full array, \mathbf{W} tended to decrease the condition number, while \mathbf{Q}_t and \mathbf{Q}_w did not. For the hemiarrray, \mathbf{Q}_t tended to decrease condition number, while \mathbf{W} and \mathbf{Q}_w tended to increase them. Therefore, when noisy measurements are to be reconstructed, using a normalization matrix that decreases condition number could be beneficial.

Reconstruction Matrix after Normalization

For convenience, each normalization method was given an index as in Table 5-2. Normalization method C5 defined in the last row of the Table 5-2 is based on WMNM reconstruction and WMNM normalization as for B4. However, normalization matrix \mathbf{Q}_t was used instead of \mathbf{Q}_w .

Computer Simulation

Two-dimensional forward models of a disk (r_d) containing a single internal anomaly (r_a) at various locations were designed and solved using Comsol Multiphysics and Matlab. We tested

Table 5-2. Index assignment for various normalization methods. The methods are represented by reconstruction matrices. The normalization matrices \mathbf{Q}_t and \mathbf{Q}_w were calculated using blur matrix definition in (5-2a) and (5-2b) respectively. Methods A1 ~ A4 are based on TSVD reconstruction (3-16), methods B1 ~ B4 and C5 are based on WMNM reconstruction (3-19).

| Index | Normalization Method | Reconstruction Matrix |
|-------|----------------------|--|
| A1 | None | \mathbf{S}^+ |
| A2 | PWS | $\mathbf{Q}_t^{-1}\mathbf{S}^+$ |
| A3 | WPI | $(\mathbf{S}\mathbf{Q}_t)^+$ |
| A4 | WMNM | $\mathbf{Q}_t(\mathbf{S}\mathbf{Q}_t)^+$ |
| B1 | None | $\mathbf{W}(\mathbf{S}\mathbf{W})^+$ |
| B2 | PWS | $\mathbf{Q}_w^{-1}\mathbf{W}(\mathbf{S}\mathbf{W})^+$ |
| B3 | WPI | $\mathbf{W}(\mathbf{S}\mathbf{W}\mathbf{Q}_w)^+$ |
| B4 | WMNM | $\mathbf{Q}_w\mathbf{W}(\mathbf{S}\mathbf{W}\mathbf{Q}_w)^+$ |
| C5 | WMNM | $\mathbf{Q}_t\mathbf{W}(\mathbf{S}\mathbf{W}\mathbf{Q}_t)^+$ |

two types of models with anomaly locations as shown in Figure 2-1 and Figure 2-2. The full array model had eight boundary electrodes placed equidistantly (Figure 2-1). The hemiarray model had eight electrodes placed on the anterior boundary only (Figure 2-2). All electrodes had the conductivity of copper ($6 \times 10^7 \text{ Sm}^{-1}$). The length of each electrode was 0.1 relative to the disk radius, subtending an angle of 5.7° on the disk perimeter. The models were discretized to 1374 second-order triangular finite elements, and then solved for boundary voltage values subject to adjacent input current patterns using the direct linear system solver UMFPACK. The anomaly had a radius $0.1 \times r_d$, and was centered at locations with relative radii (r_a/r_d) of 0, 0.2, 0.4, 0.6, 0.8 from the origin. For hemiarray cases the anomaly position was varied in angles (θ) from 0° to 180° with 5° increment. In full array cases only $\theta = -90^\circ$ was used. The model background

conductivity was set to one, and anomalies represented a unit conductivity increase from the background.

Phantom Experiment

A cylindrical phantom ($r_p = 14.0$ cm) was filled with saline solution (5 L). Vertical bar electrodes (width 13.0 mm and length 101.5 mm) were attached equidistantly around the phantom boundary to create an approximately two dimensional field pattern. An insulating plastic rod of radius 1.4 cm ($0.1 \times r_p$) was used as an anomaly, and it was moved along the α , β and γ axes (at $\theta = 0^\circ$, -90° , and 180°), with the anomaly center placed successively at relative radial displacements (r_A/r_p) of 0 (center), 0.25, 0.5, and 0.75, ten locations in total. This procedure was repeated for different volumes (50, 100, 150, 200, and 250 mL) of anomaly having conductivity similar to that of blood (0.67 Sm^{-1}) placed in the background of saline with a conductivity of 0.2 Sm^{-1} .

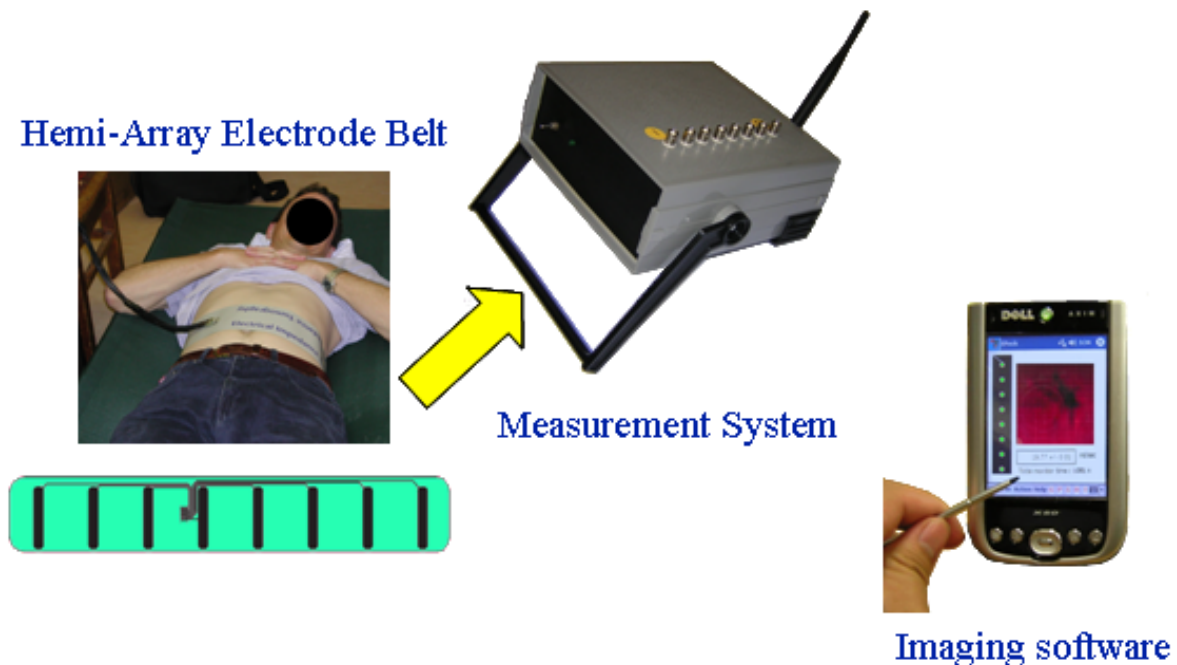


Figure 5-1. Overview of the ePack system (picture taken from Tucker *et al.* (2008))

Measurement System

We used the ePack, 8 channel EIT system to collect measurements (Tucker *et al.* 2008). The ePack is an integrated EIT system targeted at identifying intra-peritoneal hemorrhage as a result of blunt trauma. It's composed of expandable belt of bar electrodes, current source, DSP-based measurement system and imaging software (Figure 5-1). It provides flexibility in measurement by allowing various electrode configurations that can be easily set up from imaging the software. The ePack measurement system takes only 350 ms to collect one complete set of measurements, and its error range is within 0.2 % for a nominal 50 Ω resistance (Tucker *et al.* 2008). The device was operated at a 2 mA constant current and 62.5 kHz.

Results

Ideal Reconstructions

Ideal measurements were obtained by individually perturbing all elements by unit conductivity increase. They are effectively columns of the sensitivity matrix. Their corresponding QI values were calculated for all the measurements. We compared normalization methods in terms of Relative STD (*RSD*: absolute value of variation expressed as standard deviation divided by the average) calculated using all QI values as in Equation 5-11 (Table 5-3).

$$RSD(QI) = STD(QI) / average(QI) \quad (5-11)$$

Method A3 resulted in an *RSD* decrease in all cases, while C5 resulted in an overall decrease of *RSD* except along the hemiarray α axis.

Table 5-3. *RSD* of QI (5-11) calculated from the ideal measurement reconstructions (at full rank, $k = 20$) of eight electrode cases.

| Normalization Method | Full array ($\theta = 0^\circ$) | Hemiarray ($\alpha: \theta = 0^\circ$) | Hemiarray ($\beta: \theta = 90^\circ$) | Hemiarray ($\gamma: \theta = 180^\circ$) |
|----------------------|-----------------------------------|--|--|--|
| A1 | 0.1478 | 0.1749 | 0.1734 | 0.9579 |
| A2 | 0.3294 | 0.4000 | 0.2586 | 0.4829 |
| A3 | 0.0628 | 0.1023 | 0.1019 | 0.9095 |
| A4 | 0.0878 | 0.1053 | 0.1790 | 0.9846 |

| | | | | |
|----|--------|--------|--------|---------|
| B1 | 0.1124 | 0.5440 | 0.8739 | 0.1946 |
| B2 | 1.1087 | 5.8956 | 2.9424 | 16.7774 |
| B3 | 2.4142 | 0.8479 | 0.2373 | 0.5036 |
| B4 | 0.2141 | 0.2729 | 0.0936 | 0.8172 |
| C5 | 0.0672 | 0.3413 | 0.0184 | 0.6702 |

Simulated Data

Simulated measurements were created from the computer models as described in the method section. We investigated relative QI (δQI) (%) with the central anomaly as the reference. Maximum deviation errors (ε) away from the central QI value (QI_0) were calculated as in Equation 5-12 and displayed in Table 5-4.

$$\varepsilon = \text{Max}\{|\delta QI - 1|\} \quad (5-12)$$

Method A3, which was shown to perform most stably in the case of ideal measurements, also reduced ε for simulated measurements. However, it failed to decrease ε for hemiarray β axis. Method B4 showed overall decrease of ε for hemiarray cases, but its ε increased for the full array case. Method C5 produced results similar to the ideal measurement case. Its ε decreased in all cases except for the hemiarray α axis.

Table 5-4. Maximum deviation error (ε) of the relative QI, calculated from the simulated measurement reconstructions ($k = 16$) of eight electrode cases. Truncation number k was chosen based on the l -curve investigation

| Normalization Method | Full array ($\theta = 0^\circ$) | Hemiarray ($\alpha: \theta = 0^\circ$) | Hemiarray ($\beta: \theta = 90^\circ$) | Hemiarray ($\gamma: \theta = 180^\circ$) |
|----------------------|-----------------------------------|--|--|--|
| A1 | 0.7239 | 0.3134 | 0.7409 | 0.9539 |
| A2 | 2.7983 | 2.2928 | 0.5365 | 0.5759 |
| A3 | 0.2437 | 0.0671 | 0.8284 | 0.9075 |
| A4 | 0.4398 | 0.3078 | 0.8478 | 0.9574 |
| B1 | 0.2740 | 3.9886 | 2.8486 | 0.7287 |
| B2 | 1.0667 | 4.9794 | 5.2909 | 2.2658 |
| B3 | 0.3379 | 6.2294 | 2.2075 | 0.9253 |
| B4 | 0.9985 | 0.1382 | 0.5224 | 0.8945 |
| C5 | 0.2239 | 0.5944 | 0.6117 | 0.7948 |

Phantom Data

Phantom measurements were made as previously described in the method section. In Table 5-5, ε values are displayed for various volumes of the blood-like anomaly. The ε values were calculated from δQI values calculated from ten different anomaly positions.

Table 5-5. Maximum deviation error of the relative QI (ε), calculated from phantom reconstructions of eight electrode full array and hemiarray topologies. In the full array, the anomaly was placed on 4 different locations on the negative β axis with relative displacement from the domain centre ($r_A/r_P = 0, 0.25, 0.5, \text{ and } 0.75$). In the hemiarray, the anomaly was placed on 10 different locations on the $\alpha, -\beta, \text{ and } \gamma$ axes ($r_A/r_P = 0, 0.25, 0.5, \text{ and } 0.75$). Truncation number k was chosen by investigation of the l -curve.

| Normalization Method | Full array | | | | |
|----------------------|----------------------|-----------------------|-----------------------|-----------------------|-----------------------|
| | Anomaly Volume | | | | |
| | 50mL ($k = 16$) | 100mL ($k = 17$) | 150mL ($k = 17$) | 200mL ($k = 17$) | 250mL ($k = 17$) |
| A1 | 0.3344 | 0.3799 | 0.3048 | 0.2631 | 0.2377 |
| A2 | 0.8131 | 0.8741 | 0.6714 | 0.6055 | 0.5685 |
| A3 | 0.1570 | 0.1634 | 0.1517 | 0.1173 | 0.1017 |
| A4 | 0.2266 | 0.2588 | 0.2129 | 0.1760 | 0.1562 |
| B1 | 0.1896 | 0.1918 | 0.1831 | 0.1492 | 0.1318 |
| B2 | 1.6966 | 9.6980 | 17.6351 | 5.3715 | 3.5571 |
| B3 | 0.1961 | 0.3818 | 0.1346 | 0.1869 | 0.1777 |
| B4 | 0.4055 | 0.4456 | 0.3568 | 0.3126 | 0.2852 |
| C5 | 0.1513 | 0.1582 | 0.1483 | 0.1138 | 0.0980 |
| Normalization Method | Hemiarray | | | | |
| | Anomaly Volume | | | | |
| | 50mL ($k = 15$) | 100mL ($k = 16$) | 150mL ($k = 16$) | 200mL ($k = 16$) | 250mL ($k = 17$) |
| A1 | 0.5084 | 0.6845 | 0.4759 | 0.4213 | 0.4219 |
| A2 | 0.5319 | 0.2658 | 0.1438 | 0.2028 | 0.2872 |
| A3 | 0.6003 | 0.6216 | 0.5373 | 0.5155 | 0.5536 |
| A4 | 0.5923 | 0.7090 | 0.5181 | 0.4819 | 0.4940 |
| B1 | 0.6883 | 0.4502 | 0.2519 | 0.4558 | 0.3855 |
| B2 | 3.0771 | 4.5643 | 8.2285 | 6.4299 | 1.3628 |
| B3 | 0.7296 | 0.8014 | 0.7127 | 0.8695 | 0.9601 |
| B4 | 0.4587 | 0.4695 | 0.3345 | 0.3314 | 0.4013 |
| C5 | 0.3072 | 0.2578 | 0.2660 | 0.2253 | 0.2609 |

Our results in Table 5-5 show that method A2 worked better for anomalies of larger volumes in hemiarray case. B4 showed a decrease for hemiarray case, and ε values tended to

increase as the anomaly volume increased. This may have been due to our assumption of reconstructions being the weighted sum of system's PSFs. Method C5 decreased ϵ values for anomalies of all volumes in both full array and hemiarray cases.

Cross examination of Tables 5-3, 5-4 and 5-5 allow us make some findings. For the full array, the spatial variability (in terms of relative STD of QI or ϵ) decreased for A3, A4, B1 and C5. A3 and C5 seem to be best candidates since they resulted in the most decrease in most cases.

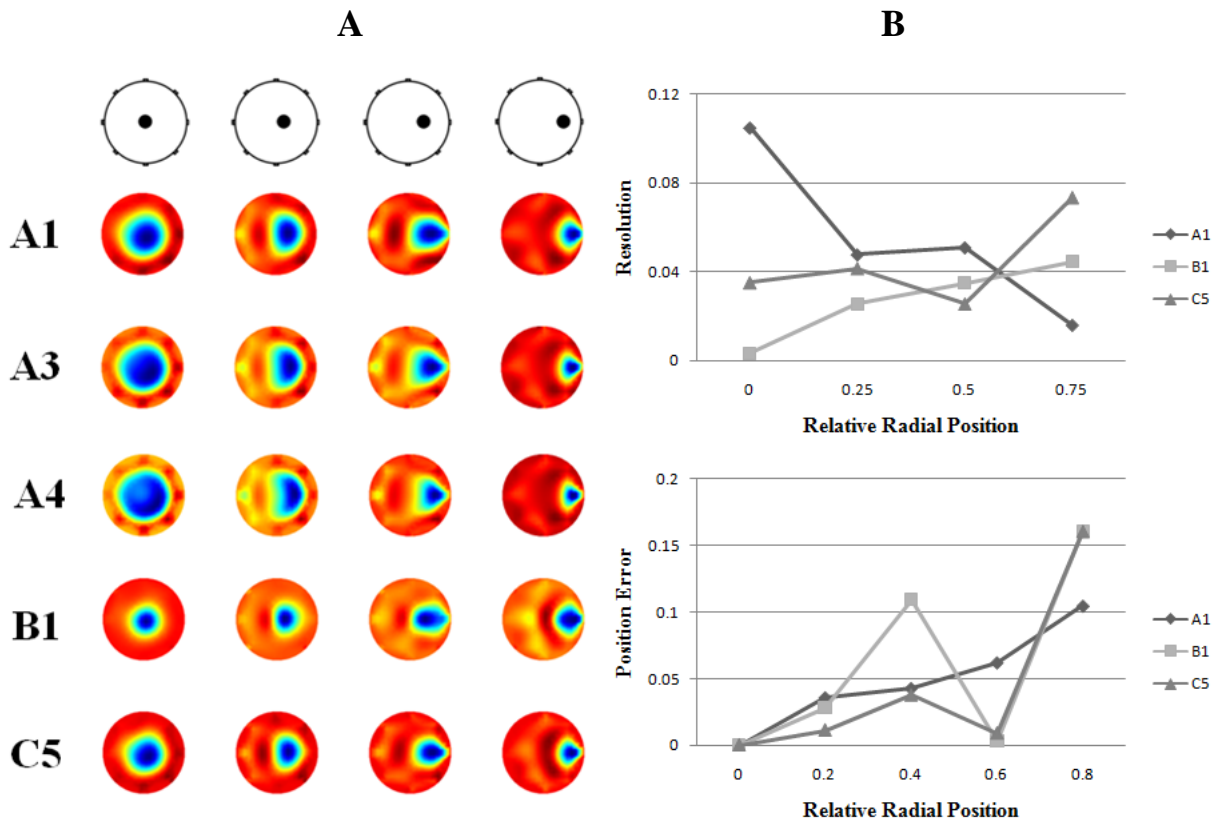


Figure 5-2. Eight electrode full array images ($k = 17$) reconstructed from phantom measurements made for a blood-like anomaly (100mL) in four different locations on the negative β axis ($r_A/r_P = 0, 0.25, 0.5,$ and 0.75). A) Images reconstructed using normalization methods A1, A3, A4, B1 and C5 are compared. B) Images reconstructed using A1, B1 and C5 were investigated in terms of the anomaly's blur radius (resolution) and position error. Resolution was calculated as a square root of the ratio between area of the half amplitude set and the actual anomaly size. Position was estimated as a centre of mass of the half amplitude set.

In Figure 5-2 (A), methods A3 and A4, which successfully reduced spatial variability of QI, resulted in blurred reconstruction of a central anomaly compared to reconstructions using B1 and C5, which produced more compact central anomaly. It should be noted that B1 and C5 are methods that are based on WNMN regularization. Method B1 blurred images of the anomaly near the boundary. C5 did not produce a blurred reconstruction of this location. Thus, C5 appears to be the most reasonable method for full array. In Figure 5-2 (B), selected methods (A1, B1 and C5) were compared in terms of resolution and position error. In order to estimate resolution, we followed definition of the blur radius suggested by Adler and Guardo (1996). Elements that have values greater than half the maximum element value were chosen as the Half Amplitude (HA) set. Then, the resolution was calculated as a square root of the ratio between area of the HA set (A_{HA}) and the domain area (A_o) as in Equation 5-13.

$$resolution = \sqrt{\frac{A_{HA}}{A_o}} \quad (5-13)$$

The position of an anomaly was located as the centre of mass of HA set in reconstruction images as in Equation 5-14.

$$position = \frac{\sum_m \sigma_m \cdot p_m}{\sum_m \sigma_m} \quad (5-14)$$

Here, p_m is the position vector (x_m, y_m) within the domain.

Small and uniform resolution values are regarded to be desirable indicating less blurring. In Figure 5-2, there are overall enhancement of resolution when using B1 and C5. In terms of position error, C5 shows great improvement except when the anomaly was close to the domain boundary.

For the hemiarray case, normalization could be made particularly effective for anomalies on the γ axis. However, this was obtained at the expense of increasing variability along the α axis. Even though B4 and C5 were most effective for β and γ axes anomalies, they were not effective for α axis anomalies (Table 5-4 and 5-5).

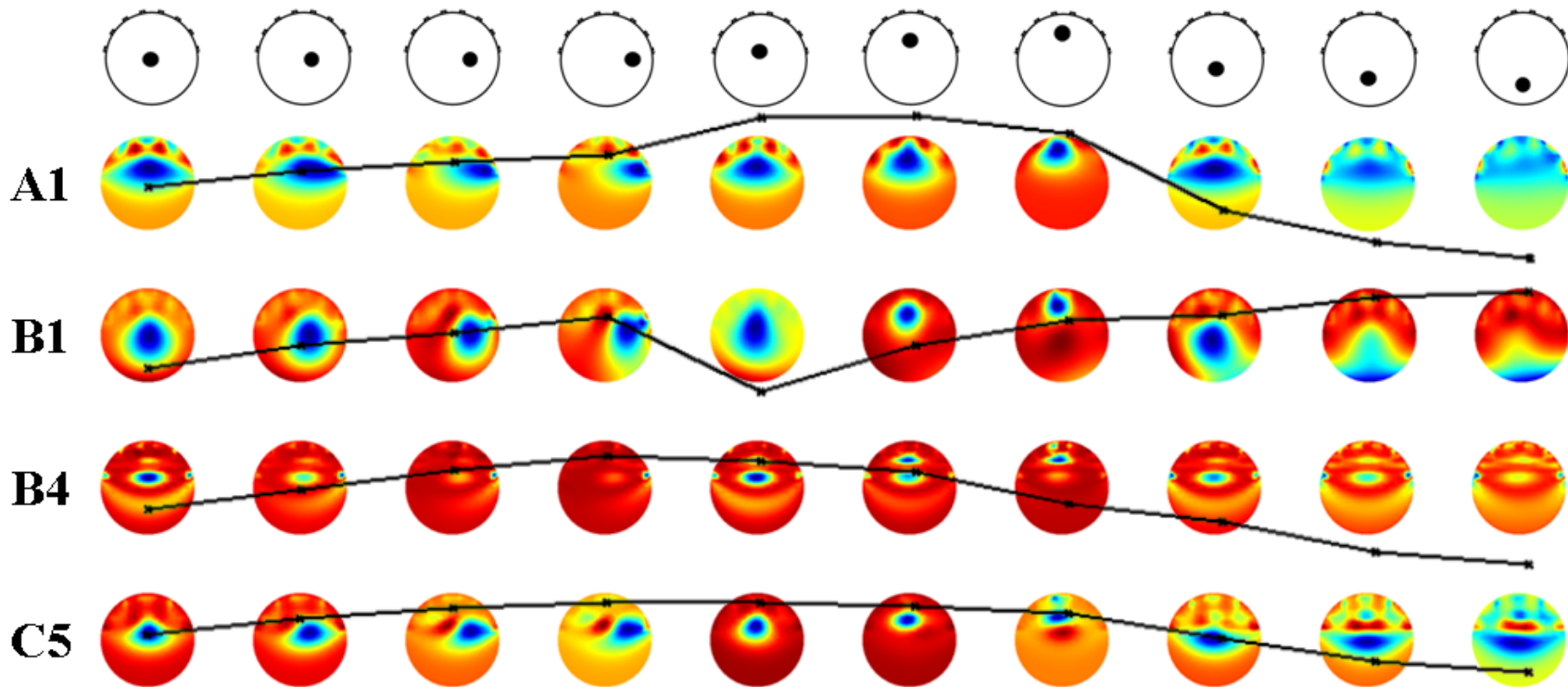


Figure 5-3. Eight electrode hemiarray images ($k = 16$) and relative QI curves reconstructed from a blood-like anomaly (100mL) using methods A1, B1, B4 and C5. Relative QI values were calculated with the central anomaly ($r_A/r_P = 0$) as a reference. All relative QI curves were scaled the same (0.5~2) and overlaid on top of each corresponding reconstruction image. The anomalies were positioned at ten different locations on the $-\beta$, α and γ axes ($r_A/r_P = 0.25, 0.5, \text{ and } 0.75$).

Investigation for various anomaly volumes (50, 100, 150, 200, and 250mL) used in our phantom experiments (Table 5-5) revealed that B4 and C5 consistently reduced spatial variability. In Figure 5-3, methods that reduced variability are compared for 100mL anomaly in ten locations. Anomaly images reconstructed using B1 were comparatively less blurry than A1, B4, and C5. In reconstruction of anomalies on the γ axis, B1 reduced the spatial variability. Method B4 performed well in terms of reducing spatial variability of QI, but did not produce a good image quality, as shown in Figure 5-3 (B4). Method C5 resulted in reduced variability producing images of improved qualities. However, images of anomalies on the γ axis were still unclear.

In Figure 5-4, performance of our proposed method C5 was demonstrated for normalizing QI in full array and hemiarray topology. The relative QI values were plotted versus radial axis. The uniformity of the relative QI curves increased, when C5 was used. The improvement was consistent for all axes considered (the α , β , and γ axes).

Discussion

Image reconstruction in EIT is a non-linear and ill-posed inverse problem. Uncertainties caused by these properties prevent EIT images from having the high-resolution typically found in MRI and CT imaging. However, one may extract a unique property (electric conductivity) of an imaged object in EIT, which is potentially valuable in clinical monitoring. EIT image reconstruction is a spatially-variant estimation problem. In this paper, we attempted to reduce spatial variance of QI. Spatial variance is hard to deal with because its properties also depend on the regularization method chosen. Therefore, we sought a general approach that can reduce spatial variance in this paper. We proposed methods that normalize full array and hemiarray EIT reconstructions using blurring properties calculated directly from the sensitivity matrix as a normalization term. This term is dimensionless, and unit of reconstructed quantities were

preserved after normalization. We found that the spatial variability observed was more dependent on the regularization scheme than the inverse model. Additionally, we found that patterns of the spatial variability were similar for different forward models. We chose the model that had elements of similar areas in order to simplify QI calculation.

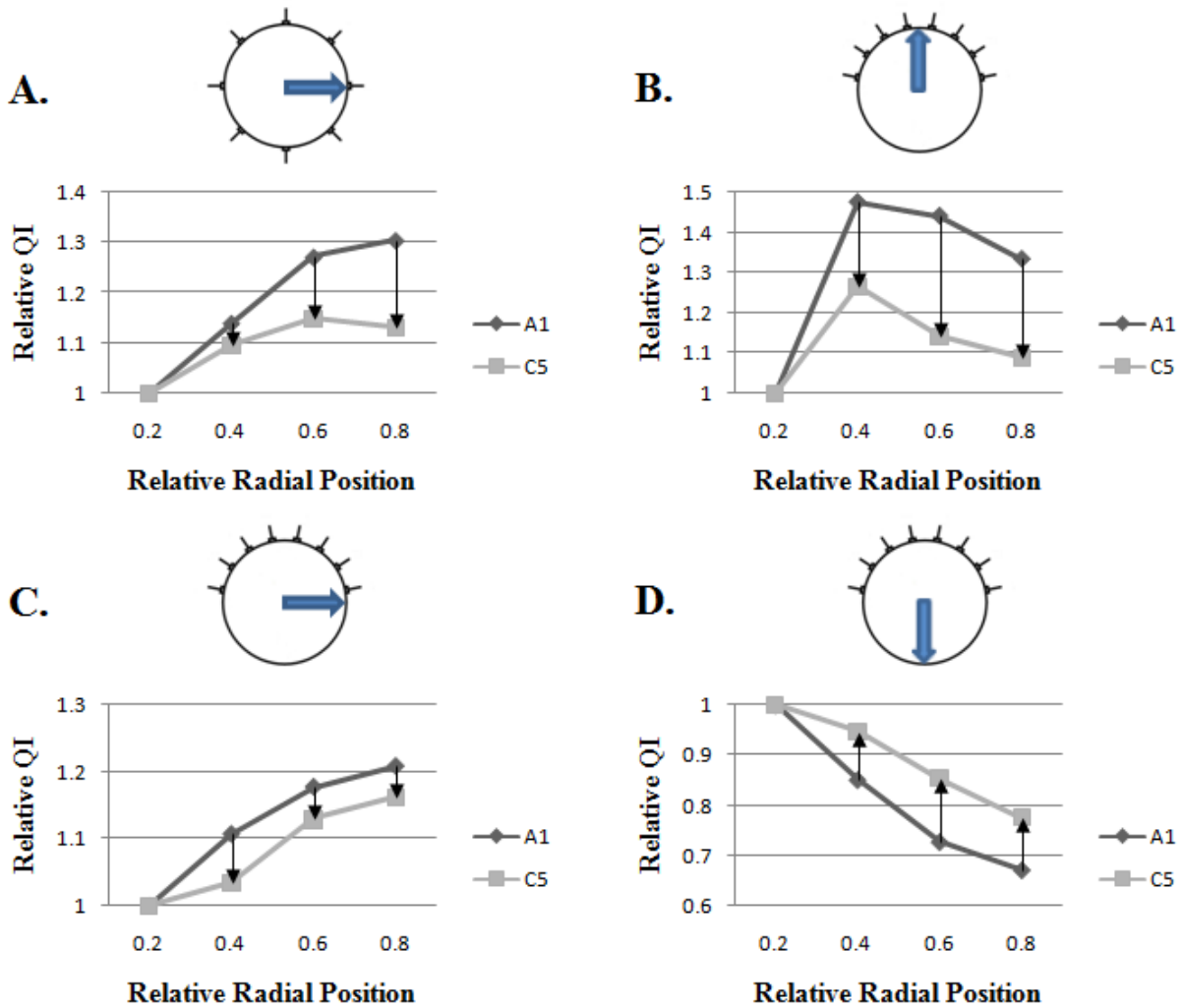


Figure 5-4. Radial curves of relative QI calculated using TSVD (A1) and normalization method (C5). The QI values are obtained from reconstructions for the full array ($k = 17$) and hemiarray ($k = 16$). The anomaly (100mL) was positioned on various locations. The curves were plotted for the A) full array $-\beta$, B) hemiarray α , C) hemiarray $-\beta$, and D) hemiarray γ axes.

We implemented normalization of spatially-variant EIT image reconstruction using three different methods: pixel-wise scaling (PWS), weighted pseudo-inversion (WPI), and weighted minimum norm method (WMNM). We found in our comparison that PWS methods generally worked poorly in reducing spatial variance. Employing WPI methods (A3 and A4) worked well for the full array, but not for the hemiarray. The WMNM-regularized reconstruction (B1) produced images of improved contrast in both full array and hemiarray cases. While B1 succeeded in reducing spatial variability for the full array, it did not reduce variability for hemiarray cases. By using the WMNM framework, but with a differently defined normalization matrix as in C5 (\mathbf{WQ}_t) rather than B1 (\mathbf{W}), Sadleir *et al.* (2008) succeeded in decreasing spatial variability of QI. C5 also produced images that were generally superior to those produced using A1. In our investigation, we confirmed the results of Sadleir *et al.* (2008) in terms of QI. Further, we demonstrated that C5 performed fairly well for the full array as well. The images in Figure 5-3 (C5) were reconstructed from phantom measurements, while the images shown in Sadleir *et al.* (2008) were reconstructed from noiseless simulated measurements. Our images did not match the images in Sadleir (2008) closely for anomalies in the γ axis. Even though the condition number of the system matrix of B1 (\mathbf{SW}) was larger than that of C5 (\mathbf{SWQ}_t) (Table 3), anomaly images reconstructed by B1 appeared less diffuse than those by C5 over all regions including the γ axis.

We tested our methods for single anomalies located at various positions within the domain. We have yet to determine if our method works well for multiple anomaly cases. Our normalization scheme was based on 2D and we obtained the blurring matrix from the sensitivity matrix of a 2D inverse model. We applied the 2D normalization method successfully to cylindrical phantom data acquired using bar electrodes. The blur matrix can easily be obtained

from a 3D sensitivity matrix, and there is restriction on implementing our normalization method in 3D.

Overall, we found that the best normalized QI values were obtained by applying a WMNM normalization method to WMNM regularization (C5) for both full array and hemiarray topologies. Our comparison showed that C5 was generally superior to other methods, even though there were test cases where it did not perform better than other candidates.

Conclusion

In this chapter, we compared various normalization methods in terms of QI. We demonstrated that some of these methods successfully reduced spatial variability of QI for the measurements obtained in numerically simulations and phantom experiments. Our investigation included many different approaches to resolve spatial variability problem in EIT image reconstruction. Although method C5 generally performed well, there was no single method that performed significantly better over both electrode topologies. However, we have showed that discrete use of this type of normalization method should result in increased quantitation stability in EIT reconstruction.

Further testing of these methods is necessary for more realistic geometries in 2D and 3D. Formulated in a straightforward manner, the methods should be simple to implement without great computational burden. Thus, they should be easily applicable to various image reconstruction problems that are spatially-variant. We anticipate that this type of normalization method could also be used for highly asymmetric image reconstruction problems.

CHAPTER 6 IMAGE RECONSTRUCTION BY WEIGHTED PSEUDO-INVERSION METHOD IN HEMIARRAY EIT

Introduction

In hemiarray EIT, the input electrodes are placed only on one half of the object to be imaged. Measurement sensitivity varies depending on the anomaly location, and some reconstructed anomalies were either invisible or erroneous when utilizing conventional regularization methods. For example, in the posterior region (γ region) of the image domain, anomalies were almost invisible when TSVD reconstruction was used (Figure 5-3). Therefore, methods to enhance image quality needs to be investigated further for 8-electrode hemiarray EIT.

We investigated Weighted Pseudo-Inverse (WPI) method to improve image quality and anomaly localization. The weighting coefficients were composed of system blurring property, which were directly calculated from the sensitivity matrix. The method was tested for a 2D simulated model with circular boundary, containing a smaller disk anomaly located in various positions. The measurements obtained from the model were contaminated with AWGN of various amounts. The effect of the WPI method was studied, and compared with plain TSVD and WMNM reconstruction methods. We found that image quality was enhanced by using the WPI method, which resulted in improvement in anomaly localization.

Method

Weighted Pseudo-Inversion

The motivation in our method is that improved images may be obtained by weighting reconstruction prior to pseudo-inversion. We define entries of a diagonal weighting matrix \mathbf{P} as in Equation 6-1.

$$p_j = \left(\sum_{i=1}^N \mathbf{B}_{ij}^2 \right)^{-1}, j = 1, 2, \dots, N, \quad (6-1)$$

where p_j values are reciprocals of square sum of \mathbf{B} 's columns. The advantages of considering properties of the blur matrix \mathbf{B} as weighting coefficients are that they are dimensionless and can be pre-calculated from the sensitivity matrix \mathbf{S} . Then, we use WPI framework to modify the problem to reconstruct the image as in Equation 6-2.

$$\Delta \hat{\sigma} = (\mathbf{SP})^+ \Delta V \quad (6-2)$$

Singular Value Decomposition

Using SVD, we can estimate basis (singular) images that determine system blurring. In Figure 6-1, we compared the singular images of \mathbf{S} (TSVD reconstruction) and \mathbf{SP} (WPI reconstruction). Singular images of \mathbf{S} fail to describe γ region, which may explain why anomalies in the γ region are invisible for TSVD reconstruction. On the contrary, singular images of \mathbf{SP} can roughly describe the entire region.

In order to investigate the effect of the WPI method, it may be worthwhile to examine the singular value spectra of the sensitivity matrices with and without weighting. In Figure 6-2, singular value spread of \mathbf{S} (TSVD reconstruction), \mathbf{SW} (WMNM reconstruction) and \mathbf{SP} (WPI reconstruction) are compared. We found that \mathbf{SP} 's singular values decrease the most rapidly as the mode number increases.

Computer Simulation

For our investigation, we used the hemiarray forward models described in Chapter 5. Anomaly position was varied with respect to relative radius ($r = 0, 0.2, 0.4, 0.6$ and 0.8); and angle displacement ($\theta : 0^\circ$ to 180° with 5° increment) (Figure 2-2).

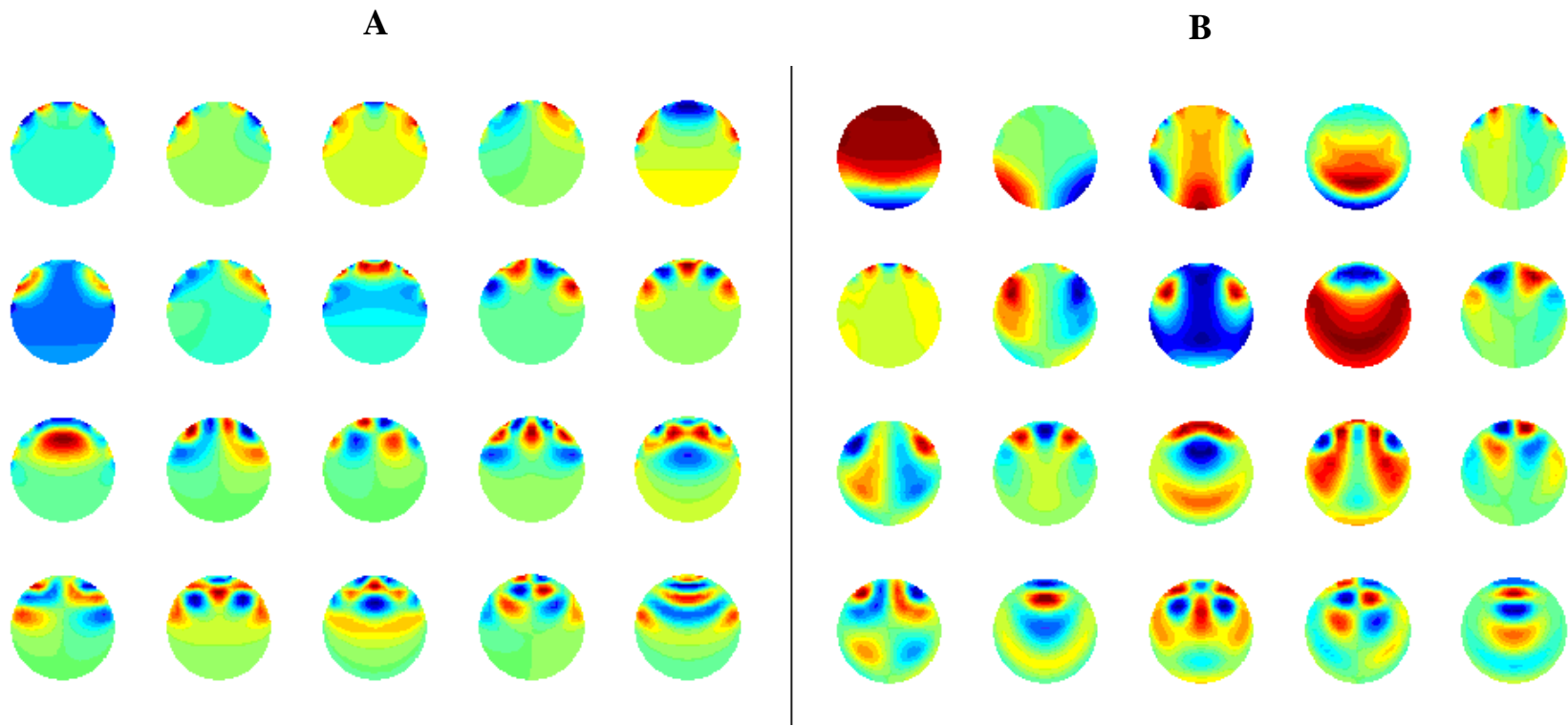


Figure 6-1. Singular images of sensitivities matrices (S and SP). A) S and B) SP in eight-electrode hemiarray case. Singular modes from 1 to 20 are displayed from left to right and top to bottom. Rank of both matrices was 20.

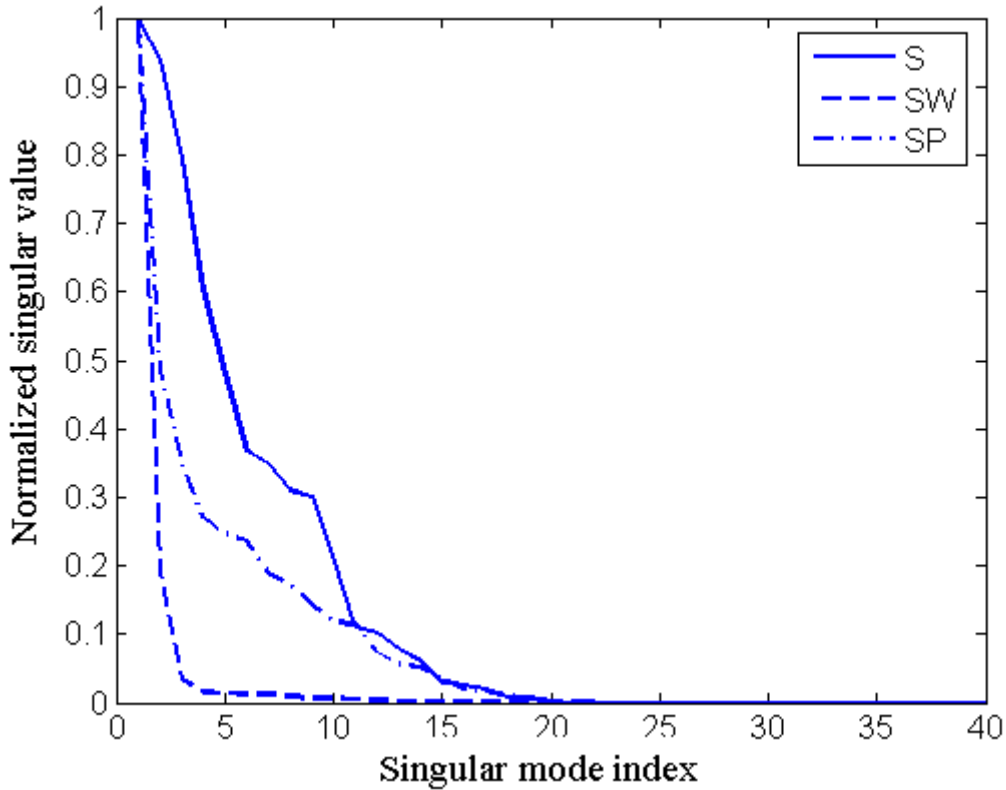


Figure 6-2. Comparison of singular value spectra **S**, **SP** and **SW** in eight-electrode hemiarray case.

Results

Noiseless Simulated Measurement

In Figure 6-3, images reconstructed from noiseless simulated measurements are displayed. Using the conventional TSVD reconstruction, we could estimate anomaly locations reasonably well for α and β regions (Figure 6-3 (A)). However, anomalies in the γ region diffused away as they moved further away from the electrodes. Using WMNM these anomalies could be roughly recovered (Figure 6-3 (B)). However, a relatively large artifact peak appeared in the α ($r = 0.8$) region, and errors in localization are seen for anomalies in the β ($r = 0.6$ and 0.8), and γ ($r = 0.6$ and 0.8) regions. The WPI method shown in Equation 6-2 produced images of improved qualities (Figure 6-3 (C)) compared to the TSVD and WMNM reconstruction methods.

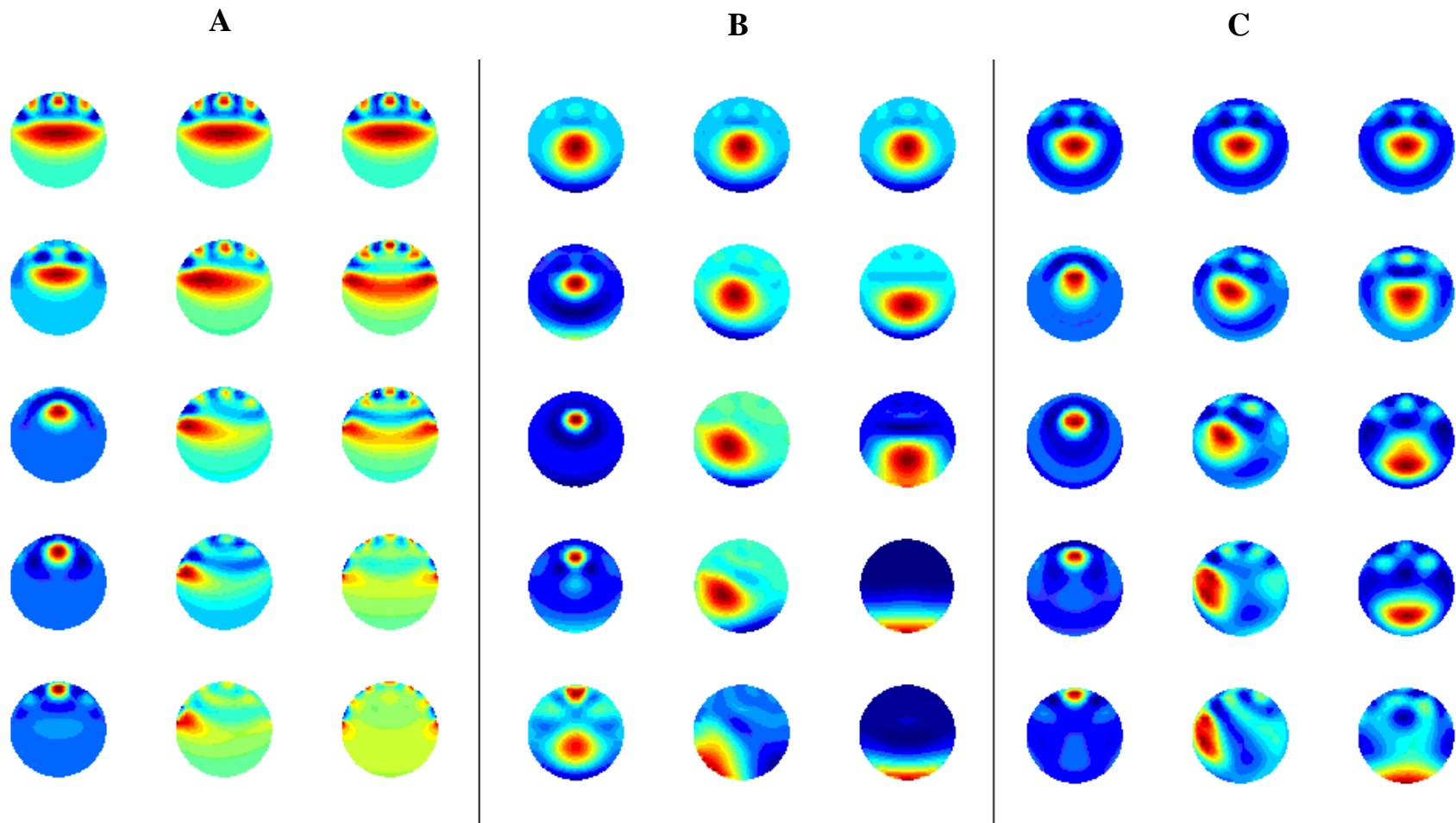


Figure 6-3 Images of a single anomaly at 15 different locations reconstructed from noiseless measurements using A) TSVD, B) WMNM and C) the WPI in eight-electrode hemiarray case ($k=20$). The first, second and third columns of each figure display anomalies on the α , β , and γ axes respectively.

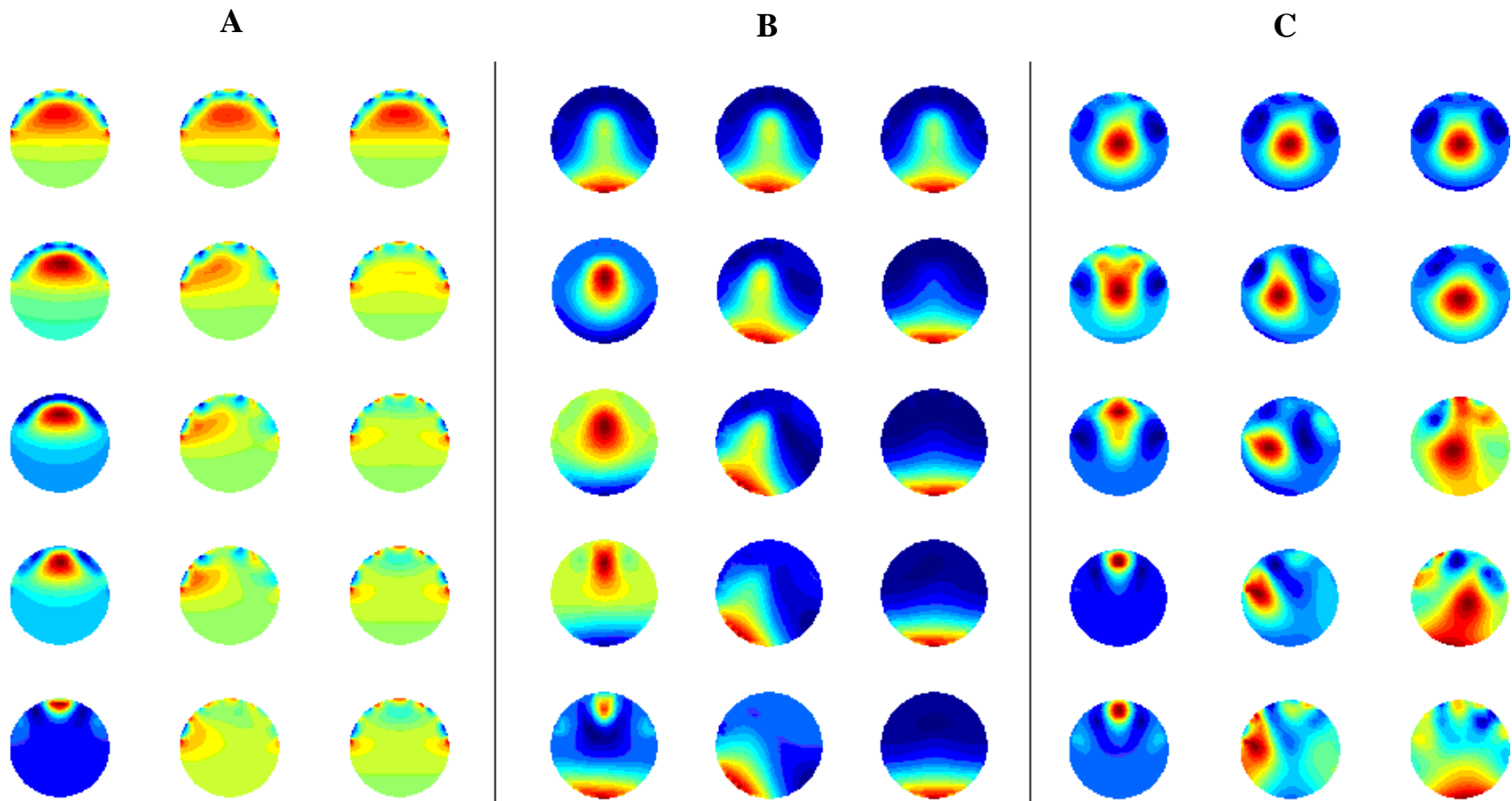


Figure 6-4 Images of a single anomaly at 15 different locations reconstructed from noisy measurements (AWGN of 30dB) using A) TSVD, B) WMNM and C) the WPI in eight-electrode hemiarray case ($k=20$). The first, second and third columns of each figure display anomalies on the α , β , and γ axes respectively.

Noisy Simulated Measurement

For noisy 3D phantom measurements, $k = 12$ was chosen after the inspection of l -curves. Here, we used $k = 12$ for the simulated measurements corrupted with AWGN of 30dB. Figure 6-4 shows that TSVD and WMNM reconstructions produced inaccurate images, while the WPI method as in Equation 6-2 produced images of acceptable qualities, which shows a potential for reasonable localization.

Localization of Anomaly

The images were created from the measurements corrupted with AWGN of various SNR. Based on the images, anomalies were localized as follows. First, image pixel values that were greater than a half of the maximum pixel value were chosen as the half amplitude set. Then, center of mass of the half amplitude set was taken as the anomaly's location. In Figure 6-5 and 6-6, we present the localization results of a single anomaly from the measurements corrupted with AWGN of 40dB and 30dB SNR respectively. The discrepancy between the original and reconstructed locations is illustrated by arrows. The mean and variance of localization errors were about 0.07 and 1.43×10^{-6} , and 0.11 and 6.17×10^{-4} respectively.

Discussion and Conclusion

The EIT image reconstruction is a spatially-variant problem. In 8-electrode hemiarray EIT, some reconstructed anomalies were either invisible or erroneous when plain TSVD and WMNM reconstruction methods were used.

In this chapter, we considered the WPI method for image reconstruction. In the WPI method, sensitivity matrix \mathbf{S} was multiplied with a weighting matrix \mathbf{P} before pseudo-inversion of the inverse problem as in Equation 6-2. By using the WPI framework, we expect to benefit from regularizing effect of the truncation, which reduces uncertainties of high spatial frequency

components. By using the WPI method, our results showed that the errors in the images were reduced. Consequently, anomaly localization became reasonable with relatively small errors.

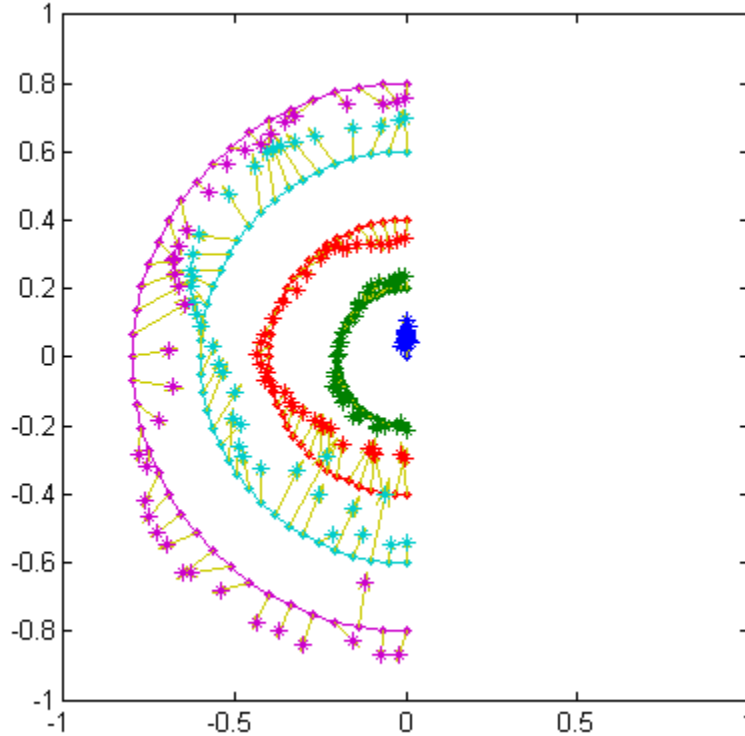


Figure 6-5. Localization of a single anomaly at various positions from simulated noisy measurements (AWGN of 40dB SNR). Images were reconstructed by the WPI ($k = 13$). Anomaly positions varied as a function of radius ($r = 0, 0.2, 0.4, 0.6$ and 0.8) and angle (θ : from 0° to 180° with 5° increment). Arrows were used to illustrate localization errors.

In Table 6-1, condition numbers of sensitivity matrices with and without weighting are presented. In 8-electrode hemiarray case, matrix **SP** had larger condition number than **S** and **SW**. Therefore, reconstruction by **SP** may be more susceptible to measurement noise.

Table 6-1. Condition numbers of sensitivity matrices with and without weighting.

| Reconstruction matrix | Condition number |
|---------------------------|-----------------------|
| S ⁺ | 9.11×10^{17} |
| W(SW) ⁺ | 4.88×10^{17} |
| (SP) ⁺ | 1.15×10^{20} |

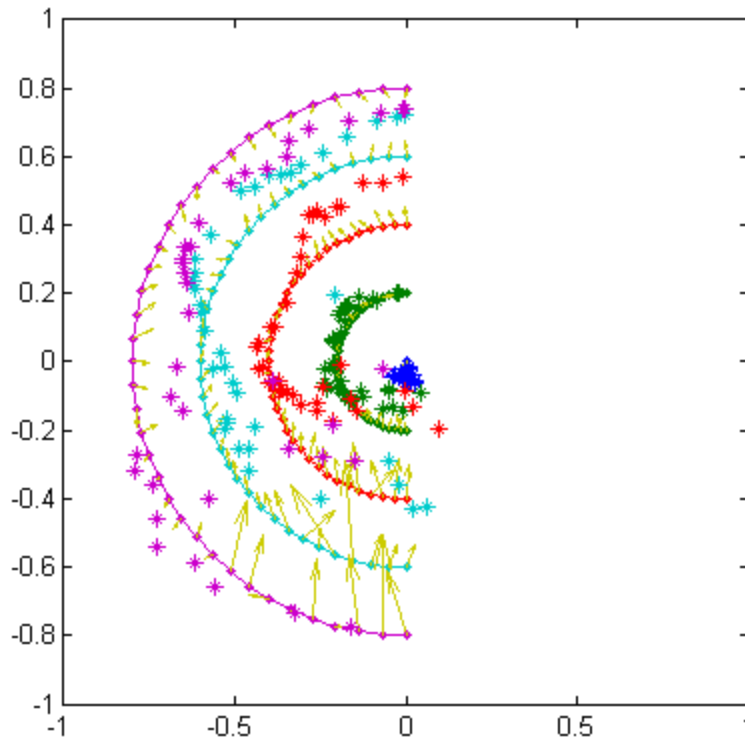


Figure 6-6. Localization of a single anomaly at various positions from simulated noisy measurements (AWGN of 30dB SNR). Images were reconstructed by the WPI ($k = 12$). Anomaly positions varied as a function of radius ($r = 0, 0.2, 0.4, 0.6$ and 0.8) and angle (θ : from 0° to 180° with 5° increment). Arrows were used to illustrate localization errors.

This investigation is limited in that only a single anomaly case was considered. Besides, we tested the method for AWGN. However, noise in the realistic measurements may be differently characterized. The method should be tested further, and its performance may be further improved by combining it with other regularization techniques.

The method is straightforward to implement and should be widely applicable to other image reconstruction problems. We anticipate that the method may be useful for any highly asymmetric image reconstruction problems.

CHAPTER 7 FUTURE WORK

Estimation of Shape Change in 3D

Object shapes are often assumed to be either cylindrical or spherical in 3D EIT. If we can define a conformal relation between the real and the assumed shapes in 3D, a similar approach to the one we introduced in Chapter 4 can be implemented to estimate the shape change. The stereographic projection is a known conformal mapping that projects a sphere onto a plane. We anticipate that this conformal mapping would play an important role in estimating shape changes in 3D EIT.

Normalization Method in EIT Image Reconstruction

Test for Anomalies of Different Conductivities

Various normalization methods in EIT image reconstruction were introduced in Chapter 5, and applied to reducing QI errors caused by spatial variability of the image reconstruction problem. The methods were tested for various volumes of an anomaly that has the same conductivity, which was regarded to simulate bleeding, perfusion or respiration. Testing for various conductivity values is suggested for future work, simulating temporal changes (aged or malignant tissues) or situational changes (i.e. effect of delivered drugs) of tissues' electrical properties.

Test for Multiple Anomalies

The normalization methods introduced in Chapter 5 is suggested to be tested for multiple anomaly cases. In lung imaging, it is beneficial to simultaneously monitor the liquid and air volumes, which can be seen to be anomalies of two different conductive properties. In the case of internal bleeding, this model can simulate bleeding from multiple sources.

Normalization in 3D

The normalization methods proposed in Chapter 5 are generic and simple to implement. We tested the methods to 2D full array and hemiarray electrode configurations. However, it can be readily tested for the 2D and 3D measurements obtained from highly asymmetrical objects. Potential areas include: subsurface imaging (Kotre 1996), imaging using a rectangular array (Mueller *et al.* 1999), and 3D cerebral imaging (Tidswell *et al.* 2001, Sadleir and Tang 2009).

APPENDIX A
MATHEMATICAL FORMULATION

Least Squares Solution

We will demonstrate how to obtain least squares solution of the inverse problem of the Equation 3-5. The least squares problem is an optimization problem, where one estimates the solution $\Delta\sigma$ by an approximate that minimizes the residual norm as in Equation A-1.

$$\min_{\Delta\sigma} \|\Delta V - \mathbf{S} \cdot \Delta\sigma\|_2^2 \quad (\text{A-1})$$

First, we take the derivative of the quantity with respect to $\Delta\sigma$ as in Equation A-2.

$$\left\{ \|\Delta V - \mathbf{S} \cdot \Delta\sigma\|_2^2 \right\} \quad (\text{A-2})$$

Then, we get Equation A-3 and Equation A-4.

$$= \mathbf{S}^T (\mathbf{S} \cdot \Delta\sigma - \Delta V) \quad (\text{A-3})$$

$$= \mathbf{S}^T \mathbf{S} \cdot \Delta\sigma - \mathbf{S}^T \cdot \Delta V \quad (\text{A-4})$$

By putting this quantity equal to zero, we get Equation A-5.

$$\mathbf{S}^T \mathbf{S} \cdot \Delta\sigma = \mathbf{S}^T \cdot \Delta V \quad (\text{A-5})$$

Finally, by inverting the square matrix $\mathbf{S}^T \mathbf{S}$, we can obtain the least squares solution expressed in algebraic form in Equation A-6.

$$\Delta\sigma = (\mathbf{S}^T \mathbf{S})^{-1} \cdot \mathbf{S}^T \cdot \Delta V \quad (\text{A-6})$$

TSVD Solution (Full Rank)

Full rank TSVD solution is equivalent to the least squares solution. For full rank truncation, \mathbf{D}^+ equals \mathbf{D}^{-1} . Thus, the TSVD solution becomes as in Equation A-7.

$$\Delta\hat{\sigma} = \mathbf{V} \mathbf{D}^{-1} \mathbf{U}^T \Delta V \quad (\text{A-7})$$

The least squares solution from Equation A-6 is calculated using pseudo-inverse of \mathbf{S} as in Equation A-8.

$$(\mathbf{S}^T \mathbf{S})^{-1} \cdot \mathbf{S}^T \quad (\text{A-8})$$

If we apply SVD to \mathbf{S} , we get Equation A-9.

$$= \left\{ (\mathbf{U} \mathbf{D} \mathbf{V}^T)^T (\mathbf{U} \mathbf{D} \mathbf{V}^T) \right\}^{-1} \cdot (\mathbf{U} \mathbf{D} \mathbf{V}^T)^T \quad (\text{A-10})$$

$$= \left\{ (\mathbf{V} \mathbf{D} \mathbf{U}^T) (\mathbf{U} \mathbf{D} \mathbf{V}^T) \right\}^{-1} (\mathbf{U} \mathbf{D} \mathbf{V}^T)^T \quad (\text{A-11})$$

$$= (\mathbf{V} \mathbf{D}^2 \mathbf{V}^T)^{-1} (\mathbf{U} \mathbf{D} \mathbf{V}^T)^T \quad (\text{A-12})$$

$$= (\mathbf{V} \mathbf{D}^{-2} \mathbf{V}^T) (\mathbf{V} \mathbf{D} \mathbf{U}^T) \quad (\text{A-13})$$

$$= \mathbf{V} \mathbf{D}^{-1} \mathbf{U}^T \quad (\text{A-14})$$

Finally, this is identical to the full rank TSVD regularization inverse of \mathbf{S} .

Weighted Minimum Norm Method

The method is motivated by that \mathbf{S} can also be written as $\mathbf{S}(\mathbf{W}\mathbf{W}^{-1})$.

$$\mathbf{S} \Delta \sigma = \Delta V \quad (\text{A-15})$$

$$\mathbf{S}(\mathbf{W}\mathbf{W}^{-1}) \Delta \sigma = \Delta V \quad (\text{A-16})$$

$$(\mathbf{S}\mathbf{W})\mathbf{W}^{-1} \Delta \sigma = \Delta V \quad (\text{A-17})$$

Then, the weighted sensitivity matrix $\mathbf{S}\mathbf{W}$ is inverted instead of \mathbf{S} as in Equation A-18.

$$\mathbf{W}^{-1} \Delta \sigma = (\mathbf{S}\mathbf{W})^+ \Delta V \quad (\text{A-18})$$

Finally, we get the final form of the WMNM solution as in Equation A-19.

$$\Delta \sigma = \mathbf{W}(\mathbf{S}\mathbf{W})^+ \Delta V \quad (\text{A-19})$$

Therefore, the overall change is modification of the reconstruction matrix \mathbf{S}^+ to $\mathbf{W}(\mathbf{S}\mathbf{W})^+$.

Tikhonov Regularization

We will demonstrate how to obtain an algebraic form of the solution by Tikhonov regularization. In the standard zero-order Tikhonov regularization, one estimates the solution $\Delta \sigma$ by minimizing the weighted sum of residual norm and solution norm as in Equation A-20.

$$\arg \min \left\{ \|\Delta V - \mathbf{S} \cdot \Delta \sigma\|_2^2 + \lambda \cdot \|\Delta \sigma\|_2^2 \right\} \quad (\text{A-20})$$

Taking the derivative of the quantity with respect to $\Delta \sigma$ gives us Equation A-21.

$$\left\{ \|\Delta V - \mathbf{S} \cdot \Delta \sigma\|_2^2 + \lambda \cdot \|\Delta \sigma\|_2^2 \right\} \quad (\text{A-21})$$

$$= \mathbf{S}^T (\mathbf{S} \cdot \Delta \sigma - \Delta V) + \lambda \cdot \Delta \sigma \quad (\text{A-22})$$

$$= \mathbf{S}^T \mathbf{S} \cdot \Delta \sigma - \mathbf{S}^T \cdot \Delta V + \lambda \Delta \sigma \quad (\text{A-23})$$

By putting the derivative equal to zero, we get Equation A-24.

$$\mathbf{S}^T \mathbf{S} \cdot \Delta \sigma + \lambda \Delta \sigma = \mathbf{S}^T \cdot \Delta V \quad (\text{A-24})$$

$$(\mathbf{S}^T \mathbf{S} + \lambda \cdot \mathbf{I}) \Delta \sigma = \mathbf{S}^T \cdot \Delta V \quad (\text{A-25})$$

Finally, inverting the square matrix $(\mathbf{S}^T \mathbf{S} + \lambda \mathbf{I})$, whose condition can be improved by choice of λ , we get the solution as in Equation A-26.

$$\Delta \sigma = (\mathbf{S}^T \mathbf{S} + \lambda \cdot \mathbf{I})^{-1} \mathbf{S}^T \cdot \Delta V \quad (\text{A-26})$$

Joukowski Transformation of a Unit Circle

Joukowski transformation from Equation 4-1 is rewritten here.

$$W = Z + c \frac{1}{Z} \quad (\text{A-27})$$

Complex number Z in Cartesian coordinates can be expressed as in Equation A-28.

$$Z = x + jy, \quad (\text{A-28})$$

where x and y are real numbers. In polar form,

$$Z = r(\cos(\theta) + j \sin(\theta)), \quad (\text{A-29})$$

where r is radial distance from Z to the origin, and θ is the radian. Similarly, complex number W can be written as in Equation A-30.

$$W = U + jV \quad (\text{A-30})$$

For unit circle $r = 1$, $Z = \cos(\theta) + j \sin(\theta)$. After the Joukowski transformation, points on the unit circle will be W as in Equation A-31.

$$W = \cos(\theta) + j \sin(\theta) + \frac{c}{(\cos(\theta) + j \sin(\theta))} \quad (\text{A-31})$$

$$= \cos(\theta) + j \sin(\theta) + c(\cos(-\theta) + j \sin(-\theta)) \quad (\text{A-32})$$

$$= \cos(\theta) + j \sin(\theta) + c(\cos(\theta) - j \sin(\theta)) \quad (\text{A-33})$$

$$= (1 + c)\cos(\theta) + j(1 - c)\sin(\theta) \quad (\text{A-34})$$

$$= (1 + c)\cos(\theta) + j(1 - c)\sin(\theta) \quad (\text{A-35})$$

From Equation A-35, we get U and V as a function of θ (Equations A-36 and A-37).

$$U(\theta) = (1 + c)\cos(\theta) \quad (\text{A-36})$$

$$V(\theta) = (1 - c)\sin(\theta) \quad (\text{A-37})$$

U and V satisfy Equation A-38.

$$\left(\frac{U(\theta)}{1 + c}\right)^2 + \left(\frac{V(\theta)}{1 - c}\right)^2 = 1 \quad (\text{A-38})$$

Therefore, W represents an ellipse whose semi-major and semi-minor axes are $1+c$ and $1-c$ respectively.

APPENDIX B
MATLAB/COMSOL SCRIPTS

Solve.m

```
function [fem,map] = solve(input,inputNeg,angle,anoIndex)
% script designs and solves a forward model for given input and specified anomaly location
% input & inputNeg : pair of electrodes used for current injection
% angle : angle of the axis where anomaly lies on. zero corresponds to the positive y axis.
% anoIndex : 1,2,3,4,5 (r = 0, 0.2, 0.4, 0.6, 0.8)
% fem : solution (voltage field) structure

flclear fem

clear vrsn
vrsn.name = 'COMSOL 3.4';
vrsn.ext = '';
vrsn.major = 0;
vrsn.build = 248;
vrsn.rcs = '$Name: $';
vrsn.date = '$Date: 2007/10/10 16:07:51 $';
fem.version = vrsn;

% Geometry
g1=circ2('1','base','center','pos',{0,0},'rot',0);
g2=square2('1','base','corner','pos',{'-.05','-.05'},'rot',0);
g2=move(g2,[1,0]);
g3=geomcomp({g1,g2},'ns',{'C1','SQ1'],'sf','SQ1-C1','edge','none');
g4=circ2('1','base','center','pos',{0,0},'rot',0);
[g5]=geomcopy({g3});
[g6]=geomcopy({g5});
g6=move(g6,[0,0]);
g6=rotate(g6,0.7853981633974483,[0,0]);
[g7,g8]=geomcopy({g3,g6});
[g9,g10]=geomcopy({g7,g8});
g9=move(g9,[0,0]);
```

```

g10=move(g10,[0,0]);
g9=rotate(g9,1.5707963267948966,[0,0]);
g10=rotate(g10,1.5707963267948966,[0,0]);
[g11,g12]=geomcopy({g9,g10});
[g13,g14]=geomcopy({g11,g12});
g13=move(g13,[0,0]);
g14=move(g14,[0,0]);
g13=rotate(g13,1.5707963267948966,[0,0]);
g14=rotate(g14,1.5707963267948966,[0,0]);
[g15,g16]=geomcopy({g13,g14});
[g17,g18]=geomcopy({g15,g16});
g17=move(g17,[0,0]);
g18=move(g18,[0,0]);
g17=rotate(g17,1.5707963267948966,[0,0]);
g18=rotate(g18,1.5707963267948966,[0,0]);

g19=circ2('0.1','base','center','pos',{'0','0'},'rot','0');
[g20]=geomcopy({g19});
[g21]=geomcopy({g20});
g21=move(g21,[0,0.2]);
[g22]=geomcopy({g21});
[g23]=geomcopy({g22});
g23=move(g23,[0,0.2]);
[g24]=geomcopy({g23});
[g25]=geomcopy({g24});
g25=move(g25,[0,0.2]);
[g26]=geomcopy({g25});
[g27]=geomcopy({g26});
g27=move(g27,[0,0.2]);

g19=rotate(g19,angle*1.5707963267948966/90,[0,0]);
g21=rotate(g21,angle*1.5707963267948966/90,[0,0]);
g23=rotate(g23,angle*1.5707963267948966/90,[0,0]);
g25=rotate(g25,angle*1.5707963267948966/90,[0,0]);

```

```

g27=rotate(g27,angle*1.5707963267948966/90,[0,0]);

% Geometry objects
clear s
s.objs={g3,g4,g6,g9,g10,g15,g16,g17,g18,g19,g21,g23,g25,g27};
s.name={'CO1','C1','CO2','CO3','CO4','CO5','CO6','CO7','CO8','C2', ...
        'C3','C4','C5','C6'};
s.tags={'g3','g4','g6','g9','g10','g15','g16','g17','g18','g19', ...
        'g21','g23','g25','g27'};

fem.draw=struct('s',s);
fem.geom=geomcsg(fem);

% Initialize mesh
fem.mesh=meshinit(fem, ...
                  'Report','off', ...
                  'hauto',5);

% Application mode 1
clear appl
appl.mode.class = 'ConductiveMediaDC';
appl.assignsuffix = '_dc';
clear bnd
bnd.Jn = {0,0,1,-1};
bnd.type = {'nJ0','cont','nJ','nJ'};

nbnd = flgeomnbs(fem.geom);
bnd.ind = [1*ones(1,nbnd)];
bdd = find(bnd.ind == 1);
arrowArrival = []; arrowDisplacement = [];
for i = 1:length(bdd)
    [xy,dxy] = flgeomed(fem.geom,bdd(i),1);
    arrowArrival = [arrowArrival xy];
    arrowDisplacement = [arrowDisplacement dxy];

```

```

end
arrowDeparture = arrowArrival - (arrowDisplacement);
leng = abs(complex(arrowDisplacement(1,:),arrowDisplacement(2,:)));

bnd.ind(bdd(find(abs(complex(arrowDeparture(1,:),arrowDeparture(2,:))) < 0.95))) = 2;
temp1 = bdd(find(abs(complex(arrowArrival(1,:),arrowArrival(2,:))) > 0.95));
temp2 = bdd(find(abs(complex(arrowArrival(1,:),arrowArrival(2,:))) <= 1.05));
temp3 = bdd(find(abs(complex(arrowDeparture(1,:),arrowDeparture(2,:))) <= 1.05));
temp4 = bdd(find(leng < 0.1));
temp = intersect(intersect(intersect(temp1,temp2),temp3),temp4);
bnd.ind(temp) = 2;

ebnd = [24 19 13 7 1 5 11 18];
bnd.ind(ebnd(input)) = 3;
bnd.ind(ebnd(inputNeg)) = 4;
appl.bnd = bnd;

clear equ
equ.sigma = {5.99e7,1,2};
equ.ind = [1,1,1,1,1,1,1,1,2,2,2,2,2,2];
if angle == 0
    anoInd = [10,11,12,13,14];
else
    anoInd = [14,13,12,11,10];
end
equ.ind(anoInd(anoIndex)) = 3;
appl.equ = equ;
fem.appl{1} = appl;
fem.frame = {'ref'};
fem.border = 1;
clear units;
units.basesystem = 'SI';
fem.units = units;

```

```

% ODE Settings
clear ode
clear units;
units.basesystem = 'SI';
ode.units = units;
fem.ode=ode;

% Multiphysics
fem=multiphysics(fem);

% Extend mesh
fem.xmesh=meshextend(fem, ...
    'Report','off');

% Solve problem
fem.sol=femlin(fem, ...
    'solcomp',{'V'}, ...
    'outcomp',{'V'}, ...
    'Report','off');

```

Solve_batch.m

```

function [fem] = solve_batch()
% script solves forward problems for all inputs prescribed
% fem : solution (voltage field) structure

nE = 8;

for angle = [0:5:180]
    for kk = 1:5
        for ii = 1:nE
            jj = mod(ii,8)+1;
            fem{ii,jj} = solve(ii,jj,angle,kk);
            cd forward
            eval(['save sol' num2str(angle) '_' num2str(kk) '.mat fem']);

```

```

        cd ..
    end
end
end
end

```

Measure.m

```

function [v] = measure(fem,P)
% script returns voltage values of specified locations for a given solution structure
% fem : solution structure
% P : points of measurements

fem.xmesh = meshextend(fem);
v = postinterp(fem, 'V', P);

```

Measure_all_8.m

```

function [Dv] = measure_all_8(fem)
% script measures voltages from loaded fem structure in 8-electrode case.
% fem : solution structure
% Dv : boundary voltage measurements

nE = 8; clear i;
Pcomplex = exp(i*2*pi/8.*[0:nE-1]);
x=real(Pcomplex);y=imag(Pcomplex);P = [x;y];
% P: electrode locations

clear temp;
index = [];
for ii = 1:nE
    temp = sort(mod([1:nE-3]+ii,nE)+1);
    index = [index; temp];
end

Dv = zeros(1,nE*(nE-3))';
for k = 1:nE

```

```

inPos = k; inNeg = mod(k,nE)+1;
femIn = fem{inPos,inNeg};
[V] = measure(femIn,P);
V = [V V(1)];
dVV = diff(V);
outV = index(k,:);
dV = dVV(outV);
Dv([(nE-3)*(k-1)+1:(nE-3)*k]) = dV';
end

```

Check_sol.m

```

function [M] = check_sol(fem,speed)
% script plays movie file showing all solutions.
% fem : solution structure
% speed : play speed of the slideshow

nE = 8;
j = [1:nE];
i = [2:nE]; i = [i 1];
kk = 0;
for k = 1:nE
    postplot(fem{j(k),i(k)},'tridata','V', ...
        'flowdata',{'Jx_dc','Jy_dc'}, ...
        'flowcolor',[1.0,0.0,0.0], ...
        'flowlines',15, ...
        'title','Streamline: Total current density [A/m^2]', ...
        'axis',[-2.08,2.08,-1.2,1.2,-1,1])
    kk = kk+1;
    M(kk) = getframe;
end
movie(M,1,speed)

```

Sensitivity.m

```

% script is used to calculated sensitivity matrix

```

```

load sMesh.mat
nsubd = 344;

% area
equ.init = {0};
equ.ind = ones(1,nsubd);
appl.equ = equ;
fem.appl{1} = appl;
fem.frame = {'ref'};
fem.border = 1;
fem.units = 'SI';
fem=multiphysics(fem);
fem.xmesh=mesnextend(fem);
init = asseminit(fem);
fem.sol = init;
A = zeros(1,nsubd);
for j = 1:nsubd
    A(j)=postint(fem,'1', 'dl',[j]);
end
save sMeshArea.mat A

fem0 = fem;
nsubd = flgeomnmr(fem0.geom);
nbnd = flgeomnbs(fem0.geom);
cd forward
load solhomo.mat, cd ..
nE = 8;

for i = 1:nsubd
    pd(i) = posteval(fem0,'1','dl',i);
    vert{i} = pd(i).p;
    fac{i} = pd(i).t; % just in case
end
clear pd

```

```

numb = [1:nE];
for n = 1:nsubd
    disp('element'); disp(n);
    for k = 1:nE
        Pos = k;
        numbe = setdiff(numb,[Pos]);
        Neg = mod(Pos,nE)+1;
        f = fem{Pos,Neg};
        f.xmesh = meshextend(f);
        Ex = postinterp(f,'Ex_dc',vert{n});
        Exx{k,n} = Ex;
        Ey = postinterp(f,'Ey_dc',vert{n});
        Eyy{k,n} = Ey;
        clear Ex, clear Ey
    end
end
save Exx.mat Exx; save Eyy.mat Eyy

S = zeros(nE*(nE-3),nsubd);
clear temp; temp = ones(1,nE-3);
inputV = [temp 2*temp 3*temp 4*temp 5*temp 6*temp 7*temp 8*temp];
clear temp
outputV = [];
for i = 1:nE
    temp = sort(mod([1:nE-3]+i,nE)+1);
    outputV = [outputV temp];
end

for n = 1:nsubd
    for i = 1:nE*(nE-3)
        input = inputV(i);
        output = outputV(i);
        S(i,n) = meshintegrate(vert{n},fac{n}, ...

```

```

        dot([Exx{input,n}; Eyy{input,n}], ...
        [Exx{output,n}; Eyy{output,n}]);
    end
end
Sfull = S;
save Sfull.mat Sfull

```

Reconstruct.m

```

% script is used to obtain TSVD image reconstruction.
clear
load Sfull8.mat; S = Sfull;
load b_0.mat

k = 16;

[U,s,V] = svd(S);
sinv = zeros(size(s));
ss = svds(S,k);
for ii = 1:k
    sinv(ii,ii) = 1/ss(ii);
end
Sinv = V*sinv*U';
x_TSVD = Sinv*b;

```

LIST OF REFERENCES

- Adler A, Berthiaume Y, Guardo R and Amyot R 1995 Imaging of pulmonary edema with electrical impedance tomography *Proc. 17th Annu. Int. Conf. IEEE EMBS, Montreal* **17** 557-558
- Adler A and Guardo R 1996 Electrical impedance tomography: Regularized imaging and contrast detection *IEEE Trans. Med. Imag.* **15** 170-179
- Adler A, Guardo R and Berthiaume Y 1996 Impedance imaging of lung ventilation: Do we need to account for chest expansion? *IEEE Trans. Biomed. Eng.* **43**(4) 414-420
- Adler A, Amyot R, Guardo R, Bates J H T and Berthiaume Y 1997 Monitoring changes in lung air and liquid volumes with electrical impedance tomography *J. Appl. Physiol.* **83** 1762-1767
- Adler A, Shinozuka N, Berthiaume Y, Guardo R and Bates J H T 1998 Electrical impedance tomography can monitor dynamic hyperinflation in dogs *J. Appl. Physiol.* **84** 726-732
- Alessandrini G and Rondi L 1998 Stable determination of a crack in a planar inhomogeneous conductor *SIAM J. Math. Anal.* **30** 326-340
- Avis N J and Barber D C 1992 Single step algorithms for image reconstruction. II. Generalization of the Sheffield filtered back projection algorithm. [Electric impedance tomography] *EIT/APT, IEE Colloquium on* **5** 1-3
- Avis N J and Barber D C 1994 Image reconstruction using non-adjacent drive configurations *Physiol. Meas.* **15** A153-A160
- Barber D C and Brown B H 1984 Applied potential tomography *J. Phys. E: Sci. Instrum.* **17** 723-733
- Barber D C and Seagar A D 1987 Fast reconstruction of resistance image *Clin. Phys. Physiol. Meas.* **8** A47-A54
- Barber D C and Brown B H 1988 Errors in reconstruction of resistivity images using a linear reconstruction technique *Clin. Phys. Physiol. Meas.* **9** A101-A104
- Barber D C 1990 Quantification of impedance imaging *Clin. Phys. Physiol. Meas.* **11** A45-A56
- Bayford R H, Boone K G, Hanquan Y and Holder D S 1996 Improvement of the positional accuracy of EIT images of the head using a Lagrange multiplier reconstruction algorithm with diametric excitation *Physiol. Meas.* **17** A49-A57
- Blott B H, Daniell G J and Meeson S 1998 Electrical impedance tomography with compensation for electrode positioning variations *Phys. Med. Biol.* **43** 1731-1739

- Blott B H, Cox S J, Daniell G J, Caton M J and Nicole D A 2000 High fidelity imaging and high performance computing in nonlinear EIT *Physiol. Meas.* **21** 7-13
- Boone K G and Holder D S 1995 Design considerations and performance of a prototype system for imaging neuronal depolarization in the brain using “direct current” electrical resistance tomography *Physiol. Meas.* **16**(3A) A87-A98
- Borsic A, Comina C, Foti S, Lancellotta R and Musso G 1995 Imaging heterogeneities with electrical impedance tomography: laboratory results *Geotechnique* **55**(7) 539-547
- Boyle A, Lionheart W R B, Gómez-Laberge C and Adler A 2008 Evaluating deformation corrections in electrical impedance tomography *IXth Conf. on EIT, Dartmouth college, New Hampshire*
- Breckon W R and Pidcock M K 1988 Data errors and reconstruction algorithms in electrical impedance tomography *Clin. Phys. Physiol. Meas.* **9** A105-A109
- Brown B H, Leathard A, Sinton A, McArdle F J, Smith R W M and Barber D C 1991 Blood flow imaging using electrical impedance tomography *Ann. Intl. Conf. IEEE EMBS* **13**(1) 307-308
- Campbell J H, Harris N D, Zhang F, Brown B H and Morice A H 1994 Clinical applications of electrical impedance tomography in the monitoring of changes in intrathoracic fluid volumes *Physiol. Meas.* **15** A217-A222
- Cheney M, Isaacson D, Newell J C, Simske S and Goble J 1990 NOSER: An algorithm for solving the inverse conductivity problem *Intl.J. Imag. Sys. Technol.* **2** 66-75
- Cherepenin V, Karpov A, Korjenskyy A, Kornienko V, Mazaletskaya A, Mazourov D and Meister D 2001 A 3D electrical impedance tomography (EIT) system for breast cancer detection *Physiol. Meas.* **22** 9-18
- Clay M T and Ferree T C 2002 Weighted regularization in electrical impedance tomography with applications to acute cerebral stroke *IEEE Trans. Med. Imag.* **21** 629-637
- Cohen-Bacrie C, Goussard Y and Guardo R 1997 Regularized reconstruction in electrical impedance tomography using a variance uniformization constraint *IEEE Trans. Med. Imag.* **16** 562-571
- Conway J 1987 Electrical impedance tomography for thermal monitoring of hyperthermia treatment: an assessment using in vitro and in vivo measurements *Clin. Phys. Physiol. Meas.* **8**(A) 141-146
- Davalos R V, Otten D M, Mir L M and Rubinsky B 2004 Electrical impedance tomography for imaging tissue electroporation *IEEE Trans. Biomed. Eng.* **51**(5) 761-767
- Dehghani H, Soni N, Halter R, Hartov A and Paulsen K D 2005 Excitation patterns in three-dimensional electrical impedance tomography *Physiol. Meas.* **26** S185-S197

- Dickin F and Wang M 1996 Electrical resistance tomography for process tomography *Meas. Sci. Tech.* **7** 247-260
- Dijkstra A M, Brown B H, Leathard A D, Harris N D, Barber D C, Edbrooke D L 1993 Review clinical applications of electrical impedance tomography *J. Med. Eng. Tech.* **17**(3) 89-98
- Dong G, Liu H, Bayford R H, Yerworth R, Gao S, Holder D and Yan W 2004 The spatial resolution improvement of EIT images by GVSMP-FOCUSS algorithm *Physiol. Meas.* **25** 209-225
- Dong G, Liu H, Bayford R H, Yerworth R, Schimpf P H and Yan W 2005 Spatial resolution improvement of 3D EIT images by the shrinking sLORETA-FOCUSS algorithm *Physiol. Meas.* **26** S199-S208
- Edic P M, Saulnier G J, Newell J C and Isaacson D 1995 A real-time electrical impedance tomography *IEEE Trans. Biomed. Eng.* **42** 849-859
- Eyüboğlue B M, Öner F A, Baysal U, Bibert Ç, Ihsan Keyf A, Yilmaz Ü and Erdogan Y 1995 Application of electrical impedance tomography in diagnosis of emphysema – a clinical study *Physiol. Meas.* **16**(3A) A191-A211
- Frerichs I, Hahn G and Hellige G 1999 Thoracic electrical impedance tomographic measurements during volume controlled ventilation-effects of tidal volume and positive end-expiratory pressure *IEEE Trans. Med. Imag.* **18**(9) 764-773
- Frerichs I 2000 Electrical impedance tomography (EIT) in applications related to lung and ventilation: a review of experimental and clinical activities *Physiol. Meas.* **21** R1-R21
- Geselowitz D B 1971 An application of electrocardiographic lead theory to impedance plethysmography *IEEE Trans. Biomed. Eng.* **18** 38-41.
- Ghahary A and Webster J G 1989 Electrical safety for an electrical impedance tomography *IEEE EMBS 11th annual intl. conf.* 461-462
- Golub G H and Reinsch C 1970 Handbook series linear algebra: singular value decomposition and least squares solutions *Numer. Math.* **14** 403-420
- Gómez-Laberge and Adler A 2006 Imaging of electrode movement and conductivity change in electrical impedance tomography *Proc. 19th Can. Conf. Electrical and Computer Eng. (Ottawa, Canada)* **19** 975-978
- Gorodnitsky I F and Rao B D 1997 Sparse signal reconstruction from limited data using FOCUSS: A re-weighted minimum norm algorithm *IEEE Sig. Proc.* **45**(3) 600-616
- Halter R J, Hartov A, Heaney J A, Paulsen K D and Schned A R 2007 Electrical impedance spectroscopy of the human prostate *IEEE Trans. Biomed. Eng.* **54**(7) 1321-1327
- Hansen P C 1987 The truncated SVD as a method for regularization *BIT* **27** 543-553

- Hansen P C 1992 Analysis of discrete ill-posed problems by means of the L-curve *SIAM Review* **34**(4) 561-580
- Hansen P C and O'Leary D P 1993 The use of the L-curve in the regularization of discrete ill-posed problems *SIAM J. Sci. Comput.* **14**(6) 1487-1503
- Hansen P C 1994 Regularization tools: A Matlab package for analysis and solution of discrete ill-posed problems *Numerical Algorithms* **6** 1-35
- Heikkinen L M, Vilhunen T, West R M and Vauhkonen M 2002 Simultaneous reconstruction of electrode contact impedances and internal electrical properties, Part II: applications *Meas. Sci. Technol.* **13** 1855-1861
- Heikkinen L M, Kourunen J, Savolainen T, Vauhkonen P J, Kaipio J P and Vauhkonen M 2006 Real time three-dimensional electrical impedance tomography applied in multiphase flow imaging *Meas. Sci. Technol.* **17** 2083-2087
- Holder D S 2005 Electrical impedance tomography: Methods, history and applications *Institute of Physics publishing*
- Jianhua Li 1994 A method of reducing the error caused by boundary shape and electrode positions in electrical impedance tomography *Physiol. Meas.* **15** A169-A174
- Kao T-J, Isaacson D, Newell J C and Saulnier G J 2006 A 3D reconstruction algorithm for EIT using a handheld probe for breast cancer detection *Physiol. Meas.* **27** S1-S11
- Keshtkar A and Keshtkar A 2007 Measured and modelled electrical bio-impedance inside the human normal and malignant bladder epithelium *International J. Biomed. Eng. Tech.* **1**(2) 127-133
- Kiber M A, Barber D C and Brown B H 1990 Estimation of object boundary shape from the voltage gradient measurements *Proc. Mtg. EIT Copenhagen* 52-59
- Kolehmainen V, Lassas M and Ola P 2005 The inverse conductivity problem with an imperfectly known boundary *SIAM J. Appl. Math.* **66**(2) 365-383
- Kotre C J 1996 Subsurface electrical impedance imaging using orthogonal linear electrode arrays *IEE Proc. Sci. Meas. Technol.* **143** 41-46
- Lionheart W R B, Lidgey F J, McLeod C N, Paulson K S, Pidcock M K and Shi Y 1997 Electrical impedance tomography for high speed chest imaging *Physica. Medica.* **13** Suppl. 1
- Lionheart W R B 1998 Boundary shape and electrical impedance tomography *Inverse Problems* **14** 139-147
- Lionheart W R B 2004 EIT reconstruction algorithms: Pitfalls, challenges and recent developments *Physiol. Meas.* **25** 125-142

- Ljaz U Z, Khambampati A K, Lee J S, Kim S and Kim K Y 2008 Nonstationary phase boundary estimation in electrical impedance tomography using unscented Kalman filter *J. of Comput. Phys.* **227**(15) 7089-7112
- Malmivuo J and Plonsey R 1995 Bioelectromagnetism: principles and applications of bioelectric and biomagnetic fields *New York, Oxford university press.*
- Mangnall Y F, Kerrigan D D, Johnson A G and Read N W 1991 Applied potential tomography: Noninvasive method for measuring gastric emptying of a solid test meal *Dig. Dis. Sci.* **36**(12) 1680-1684
- McEwan A L and Holder D S 2007 Battery powered and wireless electrical impedance tomography spectroscopy imaging using Bluetooth *IFMBE Proc. 11th Mediterranean Conf. on Medical and Biomedical Engineering and Computing 2007* **16** 798-801
- Meeson S, Killingback L T and Blott B H 1995 The dependence of EIT images on the assumed initial conductivity distribution: a study of pelvic imaging *Phys. Med. Biol.* **40** 643-657
- Metherall P, Barber D C, Smallwood R H and Brown B H 1996 Three-dimensional electrical impedance tomography *Nature* **380**(11) 509-512
- Molebny V V, Lionheart W R B, Vovk P P, Mykytenko Y H and Gouz V I 1996 Sensor position measurement for electroimpedance tomography *Med. Biol. Eng. Comput.* **34**(1) Part 1
- Morucci J-P and Rigaud B 1996 Bioelectrical impedance techniques in medicine. Part III: impedance imaging. Third section: medical application *Crit. Rev. in Biomed. Eng.* **24**(4-6)655-677
- Moskowitz M J, Ryan T P, Paulsen K D and Mitchell S E 1995 Clinical implementation of electrical impedance tomography with hyperthermia *Intl. J. Hyperthermia* **11**(2) 141-149
- Mueller J L, Isaacson D and Newell J C 1999 A reconstruction algorithm for electrical impedance tomography data collected on rectangular electrode arrays *IEEE Trans. Biomed. Eng.* **46**(11) 1379-1386
- Murai T and Kagawa Y 1985 Electrical impedance computed tomography based on a finite element model *IEEE Trans. Biomed. Eng.* **32** (3) 177-184
- Murphy D, Burton P, Coombs R, Tarassenko L and Rolfe P 1987 Impedance imaging in the newborn *Clin. Phys. Physiol. Meas.* **8A** 131-140
- Murphy S C and York T A 2006 Electrical impedance tomography with non-stationary electrodes *Meas. Sci. Technol.* **17** 3042-3052
- Nobes D C 1996 Troubled waters: Environmental applications of electrical and electromagnetic methods *Surveys in Geophysics* **17** (4) 393-454

- Nour S, Mangnall Y F, Dickson J A, Johnson A G and Pearse R G 1995 Applied potential tomography in the measurement of gastric emptying in infants *J. Pediatr. Gastroenterol. Nutr.* **20**(1) 65-72
- Oh S, Tang T and Sadleir R J 2007 Quantitative analysis of shape change in Electrical Impedance Tomography (EIT) *XIIIth conf. on Electrical bioimpedance and VIIIth conf. on Electrical Impedance tomography (ICEBI 07), IFMBE Proc.* **17** 424-427
- Oh S and Sadleir R J 2007 Compensating spatial variability of Quantity Index in 2D electrical impedance tomography: *Comsol Multiphysics study COMSOL Conf. Boston, Massachusetts*
- Oh S, Tang T, Tucker A S and Sadleir R J 2009 Normalization of a spatially-variant image reconstruction problem in electrical impedance tomography using system blurring properties *Physiol. Meas.* **30** 1-15
- Oh T I, Woo E J and Holder D 2007 Multi-frequency EIT system with radially symmetric architecture: KHU Mark1 *Physiol. Meas.* **28** S183-S196
- Pomerantz M, Delgado F and Eiseman B 1970 Clinical evaluation of transthoracic electrical impedance as a guide to intrathoracic fluid volumes *Ann. Surg.* **171**(5) 686-694
- Powell H M, Barber D C and Freeston I L 1987 Impedance imaging using linear electrode arrays *Clin. Phys. Physiol. Meas.* **8**(A) 109-118
- Pretty I A 2006 Caries detection and diagnosis: novel technologies *J. of Dentistry* **34**(10) 727-739
- Romsauerova A, McEwan A, Horesh L, Yerworth R, Bayford R H and Holder D S 2006 Multi-frequency electrical impedance tomography (EIT) of the adult human head: initial findings in brain tumors, arteriovenous malformations and chronic stroke, development of an analysis method and calibration *Physiol. Meas.* **27** S147-S161
- Sadleir R J and Fox R A 1998 Quantification of blood volume by electrical impedance tomography using a tissue-equivalent phantom *Physiol. Meas.* **19** 501-516
- Sadleir R J and Fox R A 2001 Detection and quantification of intraperitoneal fluid using electrical impedance tomography *IEEE. Biomed. Eng.* **48**(4) 484-491
- Sadleir R J, Zhang S U, Tucker A S and Oh Sungho 2008 Imaging and quantification of anomaly volume using an eight electrode 'hemiaray' EIT reconstruction method *Physiol. Meas.* **29** 913-927
- Sadleir and Tang 2009 Electrode configurations for detection of intraventricular haemorrhage in the premature neonate *Physiol. Meas.* **30** 63-79
- Sha L, Ward E R and Stroy B 2002 A review of dielectric properties of normal and malignant breast tissue *Proc. IEEE SoutheastCon.* 457-462

- Shini M and Rubinsky B 2007 Multiple biopsy probe sampling enabled minimally invasive electrical impedance tomography *Physiol. Meas.* **29** 109-126
- Soleimani M, Gómez-Laberge C and Adler A 2006 Imaging of conductivity changes and electrode movement in EIT *Physiol. Meas.* **27** S103-S113
- Soni N K, Hartov A, Kogel C, Poplack S P and Paulsen K D 2004 Multi-frequency electrical impedance tomography of the breast: new clinical results *Physiol. Meas.* **25** 301-314
- Taktak A, Record P M Gadd R and Rolfe P 1995 Neonatal lung imaging using *EIT Proc. IX Int. Conf. on Electrical BioImpedance, Heidelberg, Germany* Heidelberg: University of Heidelberg 458-459
- Tang M, Wang W, Wheeler J, McCormick M and Dong X 2002 The number of electrodes and basis functions in EIT image reconstruction *Physiol. Meas.* **23** 129-140
- Tang T, Zhang S U and Sadleir R J 2006 A portable 8-electrode EIT measurement system *Proc. VIIth Conference on Biomedical Applications of EIT*, 190-193
- Thomas D C, Siddall-Allum J N, Sutherland I A and Beard R W 1994 Correction of the nonuniform spatial sensitivity of electrical impedance tomography images *Physiol. Meas.* **15** A147-A152
- Tidswell T, Gibson A, Bayford R and Holder D 2001 Three-dimensional electrical impedance tomography of human brain activity *Neuroimage.* **13** 283-294
- Tossavainen O-P, Vauhkonen M, Heikkinen L M and Savolainen T 2004 Estimating shapes and free surfaces with electrical impedance tomography *Meas. Sci. Technol.* **15** 1402-1411
- Tucker A S, Sadleir R J, Oh Sungho and Tang Te 2008 Portable eight-electrode EIT system for detection and quantification of abdominal hemorrhage *Electrical Impedance Tomography Conference, Hanover, New Hampshire*
- Vauhkonen M, Vadász D, Karjalainen P A, Somersalo E and Kaipio J P 1998 Tikhonov regularization and prior information in electrical impedance tomography *IEEE Trans. Med. Imag.* **17**(2) 285-293
- Vilhunen T, Heikkinen L M, Savolainen T, Vauhkonen P J, Lappalainen R, Kaipio J P and Vauhkonen M 2002 Detection of faults in resistive coatings with an impedance-tomography-related approach *Meas. Sci. Technol.* **13** 865-872
- Vonk Noordegraaf A, Kunst P W, Janse A, Smulders R A, Heethaar R M, Postmus P E, Faes T J and deVries P M 1997 Validity and reproducibility of electrical impedance tomography for measurement of calf blood flow in healthy subjects *Med. Biol. Eng. Comput.* **35**(2) 107-112

- Walker D C, Brown B H, Hose D R and Smallwood R H 2000 Modelling the electrical impedivity of normal and premalignant cervical tissue *IEEE Electronics letters* **36**(19) 1603-1604
- Wheeler J L, Wang W and Tang M 2002 A comparison of methods for measurement of spatial resolution in two-dimensional circular EIT images *Physiol. Meas.* **23** 169-176
- Xu C, Dong X, Fu F, Shuai W, Liu X and Zhang C 2007 A novel image monitoring software system of electrical impedance tomography for internal hemorrhage *IFMBE Proc. World Congress on Medical Physics and Biomedical Engineering 2006* **14** 3882-3885
- Zadehkoochak M, Blott B H, Hames T K and George R F 1991 Spectral expansion analysis in electrical impedance tomography *J. Phys. D: Appl. Phys.* **24** 1911-1916
- Zlochiver S, Arad M, Radai M M, Barak-Shinar D, Krief H, Engelman T, Ben-Yehuda R, Adunsky A and Abboud S 2007 A portable bio-impedance system for monitoring lung resistivity *Med. Eng. Phys.* **29** 93-100

BIOGRAPHICAL SKETCH

Sungho Oh was born in 1975 in Wonju, South Korea. He graduated from Daewon Foreign Language High school with English and Spanish major. He entered Hanyang University with radio science and engineering major. From 1996 to 1998, he served the Republic of Korea (ROK) Army as a Korean Augmentee To the US Army (KATUSA) in Youngsan, Korea. He graduated with a bachelor's degree in electrical engineering in 2000. After graduation, he worked in marketing department, Mobile Internet Business Unit, LOCUS Corporation. The next year, he moved to the USA and began his graduate study in electrical engineering at the University of Florida. He earned his master's degree in 2004 with a thesis: *A new quality measure in electrocardiogram*. In 2005, he began his PhD study in biomedical engineering at the University of Florida. He earned his PhD in biomedical engineering in 2009 with a dissertation: *Compensation of shape change artifacts and spatially-variant image reconstruction problem in Electrical Impedance Tomography*.